University of South Bohemia
in České Budějovice
Faculty of Science

Microscopy – Point Spread Function, Focus, Resolution

Ph.D. Thesis
in the field of Biophysics

Mgr. Tomáš Náhlík

Supervisor: Prof. RNDr. Dalibor Štys, CSc.
Special Trainer: Ing. Jan Urban, Ph.D.

České Budějovice
2015

NÁHLÍK, Tomáš. Microscopy – Point Spread Function, Focus, Resolution. České Budějovice, 2015, Ph.D. Thesis. University of South Bohemia, Faculty of Science

Annotation

The aim of this thesis was to design new algorithms for processing image data from microscopes and demonstration of the possibilities of their use on standard samples (latex particles of different diameter). Results were used for the analysis of real objects inside the living mammalian cell.

For the design of these algorithms was necessary to first understand how the image in the microscope is build, including a variety of lens aberrations. It was necessary to start with simulations of ideal case displaying one point (simulation PSF). Images of Airy discs in the plane of focus, or simulations using the ENZ theory. Available ENZ simulations provide only a few sections of different focal planes. It was necessary to adjust them to a usable form for generating a full 3D view. Using these algorithms, it was examined the behavior of the basic lens aberrations, and the behavior of two particles (objects) at different distances from each other. At the conclusion of these observations, it was necessary to redefine the terms Focus and resolution. Furthermore, the definitions have been introduced for discriminability and distinguishability of objects in an image.

Thanks to the new definitions and new viewing (information entropy) to challenge the discriminability/distinguishability problem of objects in the image was possible to design and develop algorithms for image processing that enable to detect objects below the Abbe resolution condition using standard optical bright field microscopy. It has been found experimentally that the limiting factor for resolution using this method is the size and resolution of the camera chip. When using a chip with a higher density of points, we can achieve better results (detection of smaller objects) using the same

algorithms.

Anotace

Cílem této disertační práce bylo navrhnutí nových algoritmů pro zpracování obrazových dat z mikroskopů a demonstrace možnosti jejich využití na standardních vzorcích (latexové částice o různém průměru). Výsledky byly využity pro analýzu reálných objektů uvnitř živé savčí buňky. Pro navržení těchto algoritmů bylo nutné nejprve pochopit, jak vzniká obraz v mikroskopu, včetně různých aberací čoček. Bylo nutné nejprve začít se simulacemi ideálního případu zobrazení jednoho bodu (simulace PSF). Zobrazení Airyho disků v rovině zaostření, případně simulace pomocí ENZ teorie. Dostupné ENZ simulace poskytovaly pouze řezy několika rovinami zaostření a bylo nutné je upravit do použitelné podoby pro kompletní 3D zobrazení. Pomocí těchto algoritmů bylo zkoumáno chování jednotlivých základních aberací čoček a také chování dvou částic (objektů) v různých vzdálenostech od sebe. Na závěr těchto pozorování bylo nutné znovu definovat termíny zaostření (fokus) a rozlišení. Dále byly zavedeny definice pro rozlišitelnost a odlišitelnost objektů v obraze. Díky novým definicím a novému nahlížení (informační entropie) na problém rozlišitelnosti/odlišitelnosti objektů bylo možné navrhnout a vytvořit algoritmy pro zpracování obrazu a jejich logických sérií, jež nám umožňují detekovat objekty pod hranicí danou Abbého rozlišením za použití standardní optické mikroskopie ve světlém poli. Bylo experimentálně zjištěno, že limitujícím faktorem pro rozlišení pomocí této metody je velikost bodu kamerového čipu a velikost objektu, který na je na ně projektován. Při použití čipu s vyšší hustotou bodů, jsme schopni dosáhnout lepších výsledkøu (detekce menších objektů) za použití stejných algoritmů.

Declaration

Prohlašuji, že svoji disertační práci jsem vypracoval samostatně pouze s použitím pramenů a literatury uvedených v seznamu citované literatury.

Prohlašuji, že v souladu s §47b zákona č. 111/1998 Sb. v platném znění souhlasím se zveřejněním své disertační práce, a to v nezkrácené podobě elektronickou cestou ve veřejně přístupné části databáze STAG provozované Jihočeskou univerzitou v Českých Budějovicích na jejích internetových stránkách, a to se zachováním mého autorského práva k odevzdanému textu této kvalifikační práce. Souhlasím dále s tím, aby toutéž elektronickou cestou byly v souladu s uvedeným ustanovením zákona č. 11/1998 Sb. zveřejněny posudky školitele a oponentů práce i záznam o průběhu a výsledku obhajoby kvalifikační práce. Rovněž souhlasím s porovnáním textu mé kvalifikační práce s databází kvalifikačních prací Theses.cz provozovanou Národním registrem vysokoškolských kvalifikačních prací a systémem na odhalování plagiátů.

In Nové Hrady
November 15th 2015
Tomáš Náhlík

This these originated from a partnership of Faculty of Science, University of South Bohemia and Institute of Complex Systems, Faculty of Fisheries and Protection of Waters, University of South Bohemia.

Přírodovědecká fakulta
Faculty of Science

Jihočeská univerzita v Českých Budějovicích
University of South Bohemia in České Budějovice

Fakulta rybářství a ochrany vod
Faculty of Fisheries and Protection of Waters

Jihočeská univerzita v Českých Budějovicích
University of South Bohemia in České Budějovice

Acknowledgments

This work was partly supported and co-financed by the South Bohemian Research Center of Aquaculture and Biodiversity of Hydrocenoses (CZ.1.05/2.1.00/01.0024, No. LO1205 under the NPU I program), by the Ministry of Education, Youth and Sports of the Czech Republic under the grant MSM 6007665808, by the ERDF and made possible by the INTERREG IVC programme, project Innovation 4 Welfare, subproject PICKFIBER, by the GA JU152//2010/Z and project Aktion.

I would like also to thank to

- my supervisor prof. RNDr. Dalibor Štys, CSc. and my special trainer Ing. Jan Urban, Ph.D.
- all my colleagues and coworkers
- my Summer School students
- my family and my wife for support during my study

Motto

'Some hypotheses are dangerous, first and foremost those which are tacit and unconscious. And since we make them without knowing them, we cannot get rid of them.'

H. Poincaré, Science and Hypothesis, 1905.

List of papers and authors contribution

The thesis is based on the following papers (listed chronologically):

I Štys, D., Vaněk, J., **Náhlík, T.**, Urban, J., & Císař, P. (2011). The cell monolayer trajectory from the system state point of view. Molecular biosystems, 7(10), 2824-2833. (IF 2011 = 3.534)

Tomáš Náhlík participated in measurement, image analysis and entropy calculation of images of the cell. He also made the graphs and cluster analysis of entropy data.

II **Náhlík, T.**, Urban, J., Štys, D., Císař, P., Pautsina, A., & Vaněk, J. (2011). The State Trajectory of Cell Using Rényi Entropy Coefficients. Procedia Computer Science, 7, 212-213. (no IF)

Tomáš Náhlík participated in Belousov-Zhabotinsky experiment, analysis of images of the reaction and entropy calculation. He also made the the graphs and cluster analysis of entropy data.

III **Náhlík, T.**, Urban, J., Císař, P., Vaněk, J., & Štys, D. (2012). Entropy Based Approximation to Cell Monolayer Development. In 5th European Conference of the International Federation for Medical and Biological Engineering (pp. 563-566). Springer Berlin Heidelberg. (no IF)

Tomáš Náhlík participated in measurement, image analysis and entropy calculation of images of the cell. He also made the the graphs and cluster analysis of entropy data and was responsible for revision of the manuscript.

IV **Náhlík, T.**, & Štys, D. (2014). Microscope point spread function, focus and calculation of optimal microscope set-up. International Journal of Computer Mathematics, 91(2), 221-232. (IF 2014 = 0.824)

Tomáš Náhlík made all experiments, measurements, image analysis and entropy calculation of images. He also made the the graphs and cluster analysis of entropy dat and was responsible for revision of the manuscript.

List of abbreviations

In alphabetical order

AFM	Atomic Force Microscope (Microscopy)
ASM	Active Shape Model
BF	Bright Field
CCD	Charge-Coupled Device
CLSM	Confocal Laser Scanning Microscope (Microscopy)
CoC	Circle of Confusion
DoF	Depth of Field
ENZ	Extended Nijboer-Zernike (theory, model)
EXIF	Exchangeable Image File Format
GUI	Graphical User Interface
IR	Infra Red
LIL	Least Information Loss
NA	Numerical Aperture
NSOM/SNOM	Near-field Scanning Optical Microscope (Microscopy)
OSF	Object Spread Function
PALM/FPALM	Photo-Activated Localization Microscope (Microscopy)
PIE	Point Information Gain Entropy
PIG	Point Information Gain
PDG	Point Divergence Gain
PSF	Point Spread Function
RGB Image	Red, Green, Blue Image (Color Image)
SIM	Structured-Illumination Microscope (Microscopy)
STED	Stimulated Emission Depletion Microscope (Microscopy)
STORM	Stochastic Optical Reconstruction Microscope (Microscopy)
VEM/VEC	Video Enhanced Microscope (Microscopy) / Contrast

List of Figures

List of Tables

List of Listings

Contents

1 Introduction

Important questions of the current science and technology are related to micro- and nanoworld. In biology, the micro(nano)scale observations are utilized in biocompatibility assays for finding new drugs, cures, and materials (e.g., implants). These observations can be done using different techniques such as computer tomography, magnetic resonance, X-rays, and microscopy, each of them with different problems and limits.

In this thesis are presented limits of the optical microscopy. In relation to terms like resolution, focus, and focal plane, I introduce how to understand, measure, and simulate the phenomenon of Point Spread Function (PSF).

If we want to interpret a microscopic measurement in the form of an image or image series, we have to consider the microscope's transfer function which describes changes of the light properties during passing the light through the microscope. Every image obtained by microscope is not the image of the reality. We can see the image of the interaction of the light with a real object, further transferred through the system of optical elements. Each element contributes to the changes the image little bit. That means if anything in the light path is changed the resulting image can be different. If the real object is point, sum of all these changes is called a Point Spread Function (PSF), a system impulse response or transfer function of the optical system. This thesis describes experimental evidence of factors which influence the PSF in the most standard version of the optical microscope. All interactions of the light with the microscope's optical system and the sample are projected on the camera chip (Fig.1.1).

The microscope's transfer function consists of the interaction of the

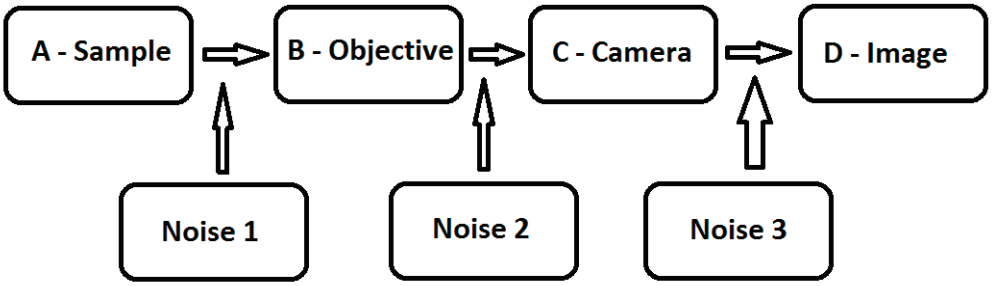

Figure 1.1: Information transfer scheme – A – Sample (cells or other objects), B – Objective (first lens), C – Camera, D – Digital image, Noise 1 – Interaction of the light with the sample, slide and cover glass, Noise 2 – Interaction of the light with the objective lenses, Noise 3 – Introducing of digital noise (sampling of signal, projection on the camera pixels); Information transfer from the sample (A) to our observation (D)

light with the sample and the imaging process which is described by the PSF. Knowledge of the PSF can help us to understand what we see and what can be seen in the microscope. This knowledge can be used also in the image processing and analysis. Simulated or measured PSF can be used as a deconvolution kernel in the deconvolution function to obtain images with better resolution and sharpness. Since an input for the deconvolution function is an original image and the PSF [1, 2, 3], knowledge of PSF gives us also another possibility to define terms like resolution and focus.

While the PSF has been studied extensively since 1940's [4, 5, 6], the interaction of the light with the sample is still, to a large extent, a subject of the individual experimental evidence. In this thesis is discussed the problem of the observation in scattered light. Although the concept of Mie scattering has been known for more than 100 years [7], most of the available theoretical analyses still rely on the Rayleigh scattering [8, 9, 10, 11]. The problem comes from the complicated outcome of the Mie[7] approach, even for a spherical object, which makes it practically impossible for its combination with the PSF. Thus, it is rather difficult to predict the outcome of the microscopy in the scattered light theoretically, despite the fact that surprisingly detailed

structures may sometimes be detected [12, 13].

The aim of this thesis is to contribute to the recognition of the difference between the theoretically described and understood PSF and the real microscope transfer function. The microscope's transfer function is understood as a process by which the microscope delivers information about the sample. Understanding the microscope as the information source opened the route towards examining this information. The subsequent aim of this thesis is thus to introduce algorithms and processing techniques of microscopic image series. All proposed techniques will be verified on nanoparticles of different size and applied to reconstruction of organelles inside an unlabelled living cells.

Here, primarily experimental results are presented and confronted with existing simulations. A point source of light of the finite size is used in theoretical simulation, whereas, in a real experiment, is substituted by small latex and gold particles. The obvious difference between these two cases lies in samples's, e.g., non-zero thickness, non-ideal shape, and non-homogeneous optical properties. Besides these commonly understood factors, effects of the changing light intensity are to a limited extent also observed [12, 14].

2 State of the art

Microscopy is a technique for observation of the objects under the resolution of human eyes. There are three main branches of the microscopy techniques used in the life sciences: The optical microscopy, which is discussed in this thesis, the electron microscopy, and the scanning probe microscopy. Optical microscope deals with the interaction of light with the sample. There are various ways how to obtain images using light microscopes. In biology, fluorescent and diffracting techniques are the most frequently used. In many cases, the sample is modified for better recognition of objects which are generally transparent and do not exhibit any fluorescent emission. Modification techniques in biological microscopy include a chemical or even molecule-biological modification of the sample. The question has to be always asked to which extent the sample after the modification represents the original object of interest. This thesis deals with techniques which do not include any sample modification.

2.1 Basic physical principles

2.1.1 Emitting vs. light diffracting imaging techniques

The most recent works performed in the field of microscopy were about fluorescent microscopes which utilize an object emanating light, fluorescent probes, nanodots etc [15]. In case of fluorescence techniques, it is necessary to excite an excitable molecule – a fluorophore – contained naturally in the sample or artificially inserted into the sample. After the excitation (light absorption), the fluorophore emits light (photons) of a lower energy (a

longer wavelength). This means that the sample itself is a source of light and the fluorophore, i.e., the actual chemical bonds whose de-excitation gives rise to the photon emission, can be consider as a point source of the light. The emitted light consequently interact with the surroundings of the sample (e.g., medium, cover glass, etc.) and with the microscope's optics. However, due to the better coherence of the emitted light, the light interaction analysis is much simpler than that for the light diffraction.

Microscopy in diffracted light is the basic, elementary, and simplest technique with no special requirements for samples. It is a non-invasive technique which can be used for observation of "true" unchanged living samples. The interactions of the diffracted light are more complicated in comparison to the fluorescence. When light hits the sample, a part of it can be absorbed, a part of it can go through the sample, and the rest is scattered. Light which goes around the sample remains untouched. Each point of the sample is a source of the second wavefronts according to the Huygens-Fresnel principle (Fig. 2.1). This new wavefronts interact with the original light either positively (constructive interferences) or negatively (destructive interferences). These interferences can be observed as the Airy discs in the image plane. Due to the interference it can happen that the size of the smallest region in the resulting wavefront which may be discriminated from its surrounding is smaller than the object which gives rise to the diffraction itself.

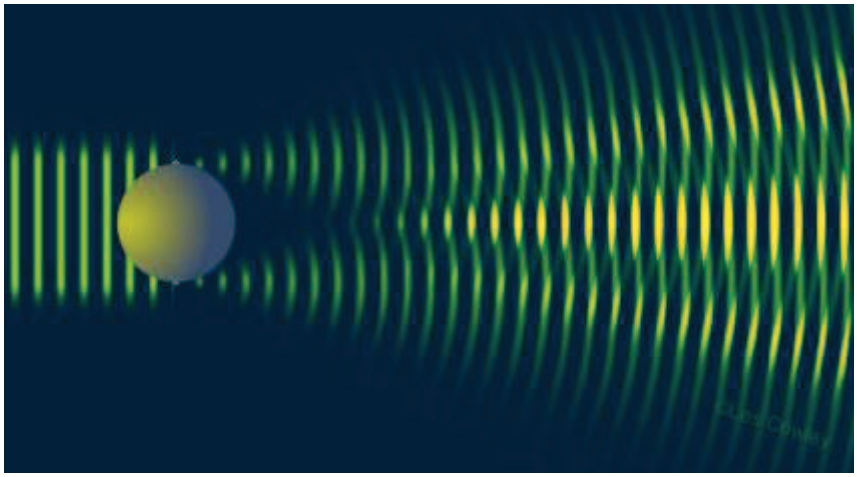

Figure 2.1: Image of the ideal diffraction of the laser light on the particle with positive and negative interferences of light wavefronts. The direction of the light is from the left to the right. [16]

All these generated wavefronts interact with the surroundings and when they hit another object they start to generate new and new wavefronts. All these wavefronts reach the lenses of the microscope and are transferred to the imaging system (camera chip). The characteristics of the scattering depends on the particle's (object's) size. The light which interact with large particles behaves according to the Mie scattering model. If the particle is smaller than the light wavelength, light is scattered according to Rayleigh scattering model (Fig. 2.3).

Mie scattering

In 1908 Gustav Mie [7] described the solution of the problem of the light scattering at the interface of the homogeneous spherical particle of any size. Mie's solution is described in terms of two parameters – n_r, x. Parameter n_r is defined as the ratio of the refractive indices of the particle (n_p) and medium (n_{med}):

$$n_r = \frac{n_p}{n_{med}}. \tag{2.1}$$

The second parameter x is described as the fraction of the meridional circumference of the sphere and the wavelength of the light in medium.

$$x = \frac{2\pi a}{\frac{\lambda}{n_{med}}}, \tag{2.2}$$

where a is a diameter of the particle.

These equations give the efficiency of the scattering which is explained as the ratio of the cross-sectional area of the scattering to the true geometrical cross-sectional area of the particle (Fig. 2.2). The size of the scattering shadow is called the effective cross-section σ_S and, related by the dimensionless constant of proportionality called the scattering efficiency Q_S, can be smaller or larger than the geometrical size A of the scattering particle:

$$\sigma_S = Q_S A. \tag{2.3}$$

A is defined as $A = \pi a^2$, where a is the radius of the spherical particle.

The medium containing many scattering particles can be described by the scattering coefficient μ_S, which depends on the density of the medium ρ_S:

$$\mu_S = \rho_S \sigma_S. \tag{2.4}$$

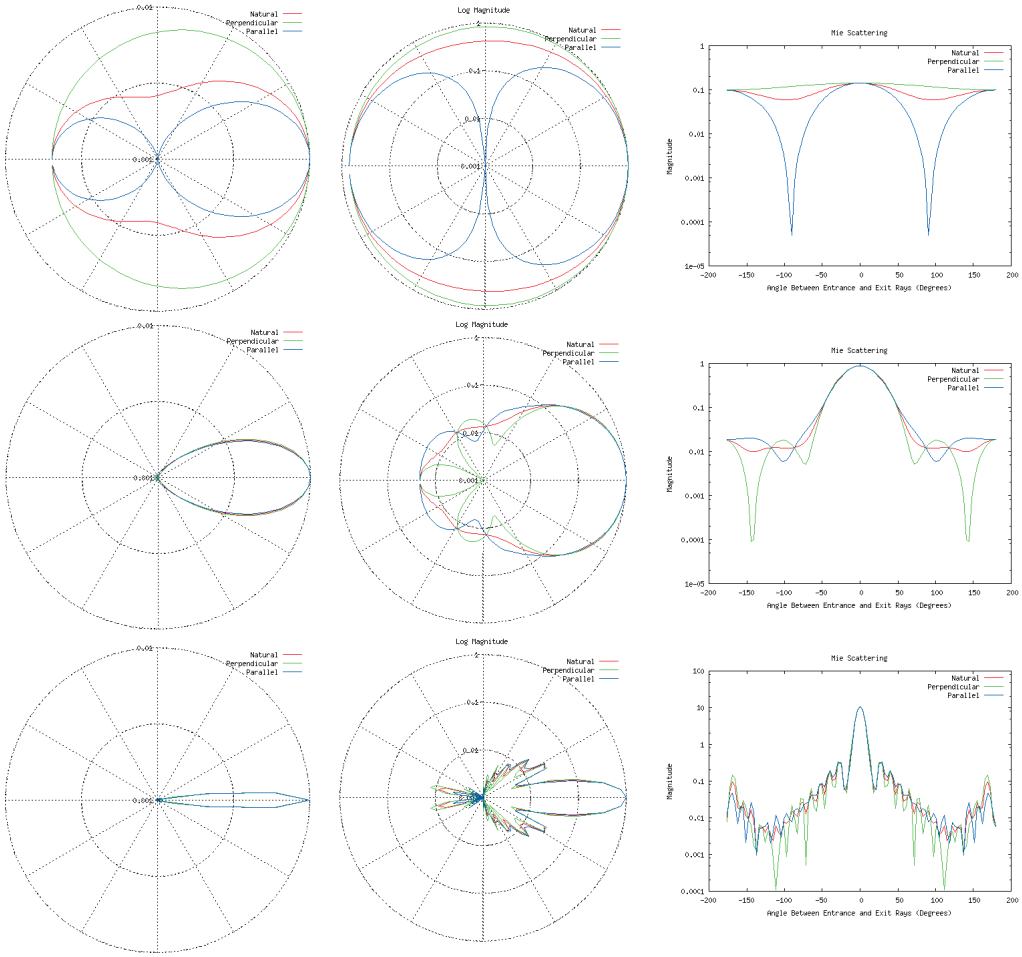

Figure 2.2: Dependency of the Mie scattering patterns on the size of the particle and type of scattered light. Light is incident from the left on a sphere located at the center of the plots. Relative size of the particle to the light wavelength $\lambda = 500$ nm is 0.2 (a 100 nm particle; first row), 1 (a 500 nm particle; second row), and 5 (a 2.5 μm particle; third row). Graphical visualizations of the same processes: a polar graph (first column), a polar graph with a radial distance in a log scale (second column), a log-linear graph of the scattering as a function of angle between entrance and exit rays (third column). Types of light scatter: unpolarized, natural (red plots), parallel (green plots), perpendicular (blue plots). The maximal magnitude was normalized to 10.

Rayleigh scattering

The Rayleigh scattering [9] is an elastic scattering of light on particles which are much more smaller than the wavelength of the light. It is the approximation of the Mie scattering for small particles:

$$I = I_0 \left(\frac{1 + cos^2\Theta}{2R^2} \right) \left(\frac{2\pi}{\lambda} \right)^4 \left(\frac{n^2 - 1}{n^2 + 2} \right)^2 \left(\frac{d}{2} \right)^6, \tag{2.5}$$

where I_0 is the intensity of the light before any interaction with the particle, R is the distance between particle and observer, λ is the light wavelength, n is the refractive index, Θ is the scattering angle and d is the diameter of the particle.

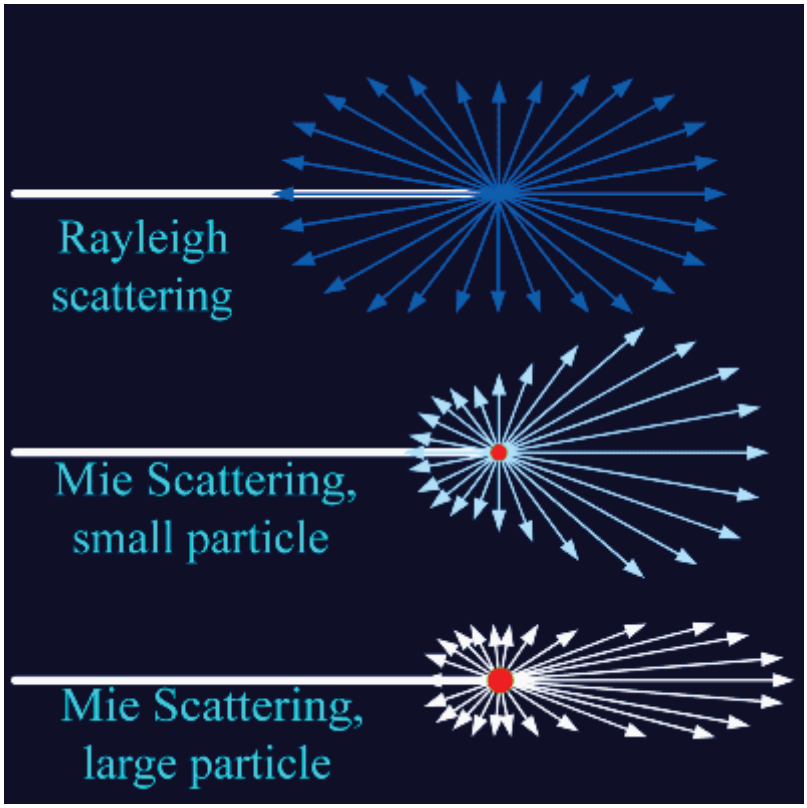

Figure 2.3: Comparison of the Rayleigh and Mie scattering. Rayleigh scattering (upper image) is scattering on the particle of the diameter $d \approx 0.2\lambda$. The size of the particle in Mie scattering, small particle (middle image), is $d \approx 1\lambda$. Size of the particle in the bottom image, Mie scattering, large particle, is $d \approx 10\lambda$ [16].

Other microscopy techniques

Electron microscopy is in some aspects similar to the light microscopy, however, it uses electrons instead of the photons (light). From the point of view of the wave nature, electrons are particles of a very short wavelength and high energy (i.e. electron with energy of 10 keV means wavelength 12.2 pm, 200 keV means 2.5 pm). Due to this fact, the point spread function negligible and observations done using electron microscopy suffer from a relatively small image distortion. However, electron microscopy has also many principal and technical limitations. The principal limitations are the large electron-sample

cross-section (many electrons interact with the sample, sometimes more than once) and low scattering efficiency of carbon atoms. The former limits the intelligibility of the structural details of thicker samples, the latter often leads to the need of labelling. The technical limitations cause that, in most cases, electron microscopy cannot be used for observation of living samples, because sample preparation usually includes a special manipulation (e.g., freezing, metal coating, cutting to very thin slices, etc.).

The microscopy in electron diffracting beam has basically most of the same problems of reproduction of the original object shape.

Scanning probe microscopy uses an interaction of the probe with the sample. The example of the scanning probe microscopy is the AFM (Atomic Force Microscopy)[17] or NSOM/SNOM (Near-Field Scanning Optical Microscopy) [18, 19]. This technique can influence the behaviour of the living sample due to the interaction with the probe. The case that a living cell does not have to be chemically fixed to the sample support is also very seldom. Using the AFM, no information about the sample interior is also obtained.

Many experiments were done and described in the field of confocal and deconvolution microscopy and by using special optics, also many simulations were introduced for confocal microscopy [1, 2, 3, 20, 21]. Also techniques like SIM (Structured Illumination Microscopy) [22, 23, 20, 21, 24, 25], 4Pi [26, 27, 21], STORM (Stochastic Optical Microscopy) [28, 29, 20], PALM (Photoactivated Localization Microscopy) [30, 31, 20, 21] , STED (Stimulated Emission Depletion Microscopy) [32, 33, 20, 21, 34] can help with improving of the quality of the final microscopy image.

The problem is that most of these techniques use special equipment or needs special treatment of the sample. We are introducing methods which are based on image processing and primarily designed for bright-field microscopy [35, 36].

Distortions of image obtained by optical lenses

Unfortunately, images obtained by light microscopy suffer from many image distortions. Image distortion is a form of the optical aberration [37]. In mathematical sense, it may be understood as a deviation from the rectilinear projection. This can be due to the imperfection of the lenses, where different parts of the lenses focus the image to the different point. As discussed below, the approaches to understanding the distortion of the image by the microscope's imaging system are available for light sources of various kinds [38, 39, 40, 41].

A major problem of light microscopy of samples comes from the sample thickness. From the lens through the focus to infinity, elements from various focal planes of the sample contribute to the signal at any level of the light path. During the observation in light diffraction, apparent intensity maxima and minima, which may be mistaken for the recognition of the focus, are observed at several levels along the optical path.

Microscopic image of the real diffracting structure is composed of many individual diffracting elements. Their diffracting properties vary with size and surface properties[7]. In this work are demonstrated diffraction patterns of standard balls and way of their analysis. The microscopic images of these simple objects are complicated and any attempt of their reconstruction into elementary objects is beyond reality. What remains is technical, empirical analysis based only on few simple assumptions about the course of the imaging function along the optical axis. Outlines of the use of these assumptions is presented in the manuscript which accompanies this dissertation.

Type of lens' distortions

Modern lens systems are widely assumed to produce, to a large extent, aberration-free images. This assumption is close to the truth for very thin samples in which majority of observed objects is very close to the focal plane or the microscope's optical axis. For an object placed in a less favourable position, the complicated composition of optical elements may paradoxically

lead to higher, or at least less intelligible, distortion than that observed in a more traditional optical path [42, 43, 44]. The general positions prevail mainly in biological sample.

In order to understand how each object is imaged by the lens, the main distortion properties of lenses must be firstly explained. Effects of different distortions are shown on the example of the simple square net (Fig. 2.4 A).

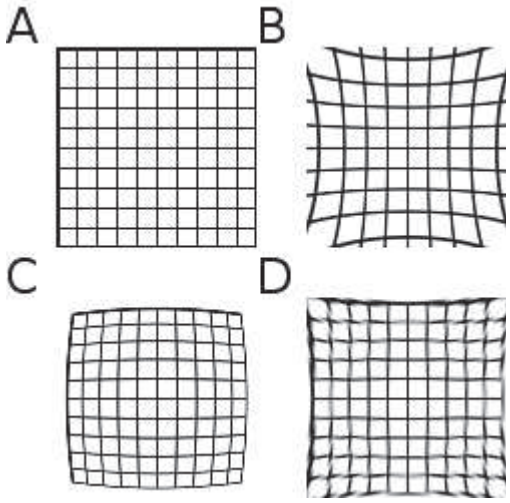

Figure 2.4: Example of lens' distortions. A - Image without any distortion. B - Pincushion Distortion. C - Barrel Distortion. D - Moustache Distortion.

The pincushion distortion cause the increase of the image magnification with the distance from the optical axis. The lines that do not go through the centre of the image are bowed inwards, towards the centre of the image (Fig.2.4 B). It is the opposite effect to the barrel distortion.

The barrel distortion leads to the decrease of the image magnification with distance from the optical axis. Only lines which goes through the optical axis are straight. Other lines are curved in the way that the central part of the lines goes out of the image, whereas the ends of the lines point into the image (Fig. 2.4 C). The barrel distortion, known also as a "fish-eye", is the way how to map an infinitely wide object's plane into a finite image area. For a zoom lens, barrel distortion appears in the middle of the lens'

focal length range and is worst at the wide-angle end of the range.

The moustache distortion is a mixture of both previously mentioned types. It can be called a complex distortion and is less common but not rare. It starts out as a barrel distortion close to the image center and turns gradually into a pincushion distortion towards the image periphery. (Fig.2.4 D)

2.1.2 Focus, Focal Plane, Depth of focus

The shape of the PSF is related to the terms focus, depth of focus, depth of field, and circle of confusion.

The focus is a special distance between sample and objective. It is a focus (image) point, where, in ideal case, all light rays meet (in the geometry optics approximation) or the electromagnetic field intensity of light emanating from a flat light source is the highest (in Maxwell's theory) after transition through the lens. The focal length is a distance between the focus point and the center of the lens (Fig. 2.5).

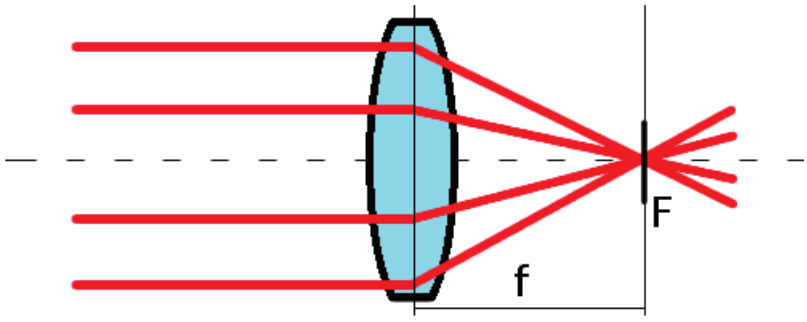

Figure 2.5: Scheme of light passing through the lens. The point F where the light rays meets is called a focal point, the distance f is a focal length.

The depth of focus has different meanings. The definitions are often subjective or depend on a model or convention. The first meaning is the distance over which the image plane can be displaced while a single object plane remains in acceptably sharp focus. The second meaning is the image-side conjugate of depth of field. If the depth of focus is related to a

single plane in object space, it can be calculated as

$$t = 2Nc\frac{v}{f}, \tag{2.6}$$

where t is the depth of focus, N is the lens f-number, c is the circle of confusion, v is the image distance, and f is the lens focal length. Eq. 2.6 can be expressed in terms of magnification m (Eq. 2.7) as

$$t = 2Nc\,(1 + m) \tag{2.7}$$

The definition of the depth of focus in digital microscopy is simple and connected to the PSF. We demonstrate the case when the image of the nanoparticle in the focus is only one pixel (i.e., element of the CCD area detector) in the camera chip. When optical slices (Z-stack) are made, the image of this particles is enlarged. The section along the optical axis within which the image of this particle does not overflow to the neighbouring pixel is called the depth of focus (2.6).

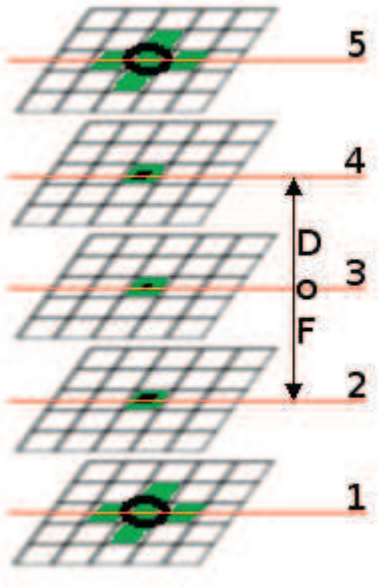

Figure 2.6: Digital definition of the Depth of Focus. Black points are projections of the object on the camera chip, which is shown as a net. Green color represents pixels which correspond to the signal (black points). The red lines are the Z-Steps. The black arrow is the Depth of Focus.

The depth of field (DoF) is the distance between the sharp nearest and farthest object in the scene. The lens can, of course, focus only at one distance at the same time but the non-sharpness in the image can be invisible under standard viewing condition.

The circle of confusion (CoC) is known also as a disk of confusion, circle of indistinctness, blur circle, or blur spot (Fig. 2.7). CoC is an image of the point of the light which comes through the lens not in the perfect focus. CoC is used for the definition of the depth of focus in a traditional microscopy.

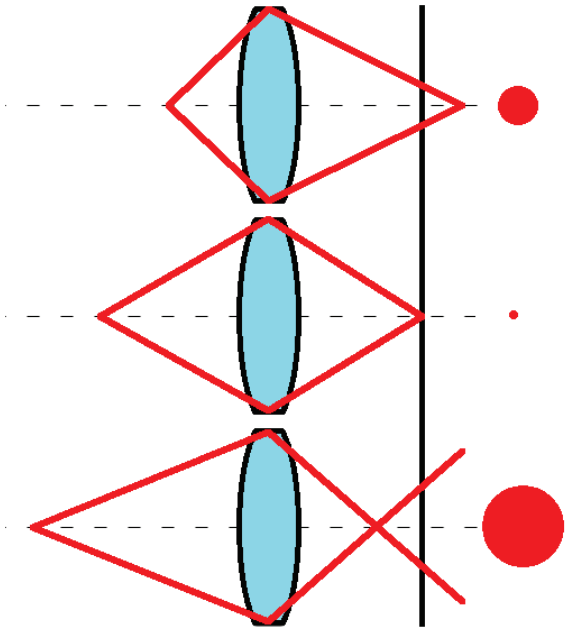

Figure 2.7: Scheme of Circle of Confusion.

2.1.3 Resolution, Distinguishability, Discriminability

One of the basic singular numbers which characterizes any optical system is the resolution. The angular resolution (or spatial resolution) is a property of the optical system which describes its ability to distinguish small details of an object. It can be considered as a size of the smallest observable object or a distance between two objects to be seen separately. Provided two peaks (signals) separated by the valley of the lowest point of at least 5% of the higher peak (Dawes' limit), the resolution is defined as a distance between peaks' maxima (Fig. 2.8).
Commonly used definition of the resolution was defined by Abbe [45] as the separation between two sharp lines on a grid:

$$D = \frac{\lambda}{2nsin\theta}. \tag{2.8}$$

where D is resolution (distance between to lines), θ is used wavelength (resolution is wavelength dependent) and $nsin\alpha$ is numerical aperture (NA) of

the system.

The angular resolution Θ can be calculated using wavelength λ and diameter D of the lens' aperture as

$$\Theta = 1.220\frac{\lambda}{D}. \tag{2.9}$$

This equation can be transform to spatial resolution (eq. 2.10)

$$\Delta l = 1.220\frac{f\lambda}{D}, \tag{2.10}$$

where Δl is the spatial resolution and f is the focal length of an objective. The constant 1.220 in Eqs. 2.9 and 2.10 comes from the calculation of the position of the first minimum of Airy Disc.

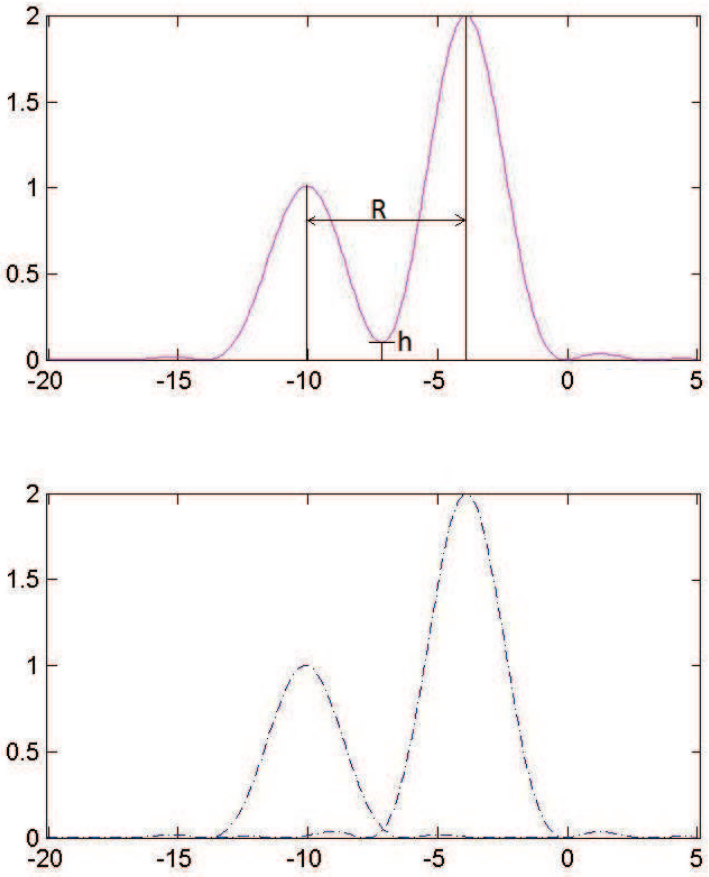

Figure 2.8: The example of the resolved signals. The upper graph shows a cumulative (superimposed) signal of two individual signals in the bottom graph. R is the resolution and h is the height of the valley between two peaks, which varies from 5% to 10% of the value of the maximum of the higher peak [46].

The resolution in microscopy is usually defined as a function of wavelength of the light (illuminating or emanating) λ and numerical apertures NA

$$R = \frac{1.220\lambda}{NA_{condensor} + NA_{objective}}, \tag{2.11}$$

where the numerical aperture for each lens (the condensor or objective) is expressed as

$$NA = \eta sin\Theta, \tag{2.12}$$

where η is refractive index of the medium between the lens and the specimen and Θ is a half of the included lens' angle α. This depends on the focal length and the diameter of the lens.

Heisenberg [47, 48] claimed that if resolution of position was

$$\Delta x = \frac{\lambda}{sin\frac{\epsilon}{2}}, \tag{2.13}$$

then the electron's momentum in the x direction was determined up to

$$\Delta p_x \approx 2\frac{h}{\lambda} sin\frac{\epsilon}{2}. \tag{2.14}$$

Eqs. 2.13 and 2.14 gives [48]

$$\Delta x \Delta p_x \approx \left(\frac{\lambda}{sin\frac{\epsilon}{2}}\right)\left(2\frac{h}{\lambda} sin\frac{\epsilon}{2}\right) = 2h \tag{2.15}$$

Further, we defined another two terms – discriminability and distiguishability [46] – which are related to the resolution by the term

$$discriminability \leqq resolution \leqq distinguishability. \tag{2.16}$$

The term **distinguishability** of an object means that there exists **at least one element** of the object which is uniquely assigned only to this object. It the microscopic image can be defined as a distance between two signals (peaks, intensity maxima or minima) such that there exists a valley between them. In the case of the image this means that two points of equal intensity are distinguishable if between them exists at least one point with lower intensity (Fig. 2.9 A). In contrast, two points in the image are **discriminable** if there exists any condition which **each point** of the object uniquely assigns only to this object and not to the neighbouring one. This means that two point objects in the microscope image are discriminated at the condition of different color, intensity or position (Fig. 2.9 B).

Two distinguishable values are already discriminable. However, only

some discriminable values are distinguishable (those with the valley)[46].

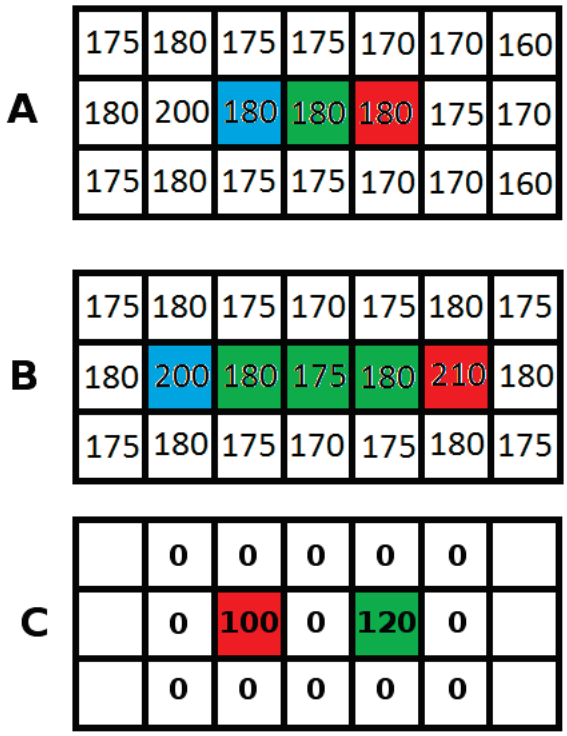

Figure 2.9: Definition of terms distinguishability, discriminability a and resolution for the image. The numbers represent intensity values.
A - The pixels of the same value (marked by blue, green and red) are discriminable due to their different positions. All these pixels can be part of one object but pixels itself are discriminable. This means that property called as resolution of the camera (or image) is not resolution but it is the number of discriminable points.
B - Two pixels with intensity values of 200 and 210 (blue and red) are distinguishable due to their separation by green points of lower intensity. This means that between two peaks (highest values) there is a valley (lower values). We can guess that this can be two separated objects with overlapping PSF (resp. OSF).
C - Two pixels (red - value 100 and green - value 120) are in distance of resolution if between them there is at least one pixel with the minimal value (in case of intensity it is a 0). This means that resolution is not the minimal distance. The maximal resolution of the image has quarter value (half in both direction) than the value which is given by standard meaning.

2.2 Models

There are two possibilities how the behaviour of the light on its path through the microscope can be understood. The first option is by simulation. Simulation of Airy disc for diffracting light or ENZ theory for fluorescent microscopy can be used. The second option is via experiments with particles of defined properties, i.e. latex or gold nanoparticles.

Airy disc simulation describes the behaviour of light in the sense of the ray optics. The simulation according to ENZ theory describes the light as waves.

2.2.1 Airy Disc Simulation – Diffraction

The simplest way how to simulate the PSF is the simulation of Airy Disc. Airy disc is named after the English astronomer and mathematician Sir George Biddell Airy. Airy Disc and Airy Pattern are description of diffraction of the light in the best focal plane and using perfect lens.

$$I(\Theta) = I_0 \left(\frac{2J_1(k\alpha sin(\Theta))}{k\alpha sin(\Theta)} \right)^2 = I_0 \left(\frac{2J_1(x)}{x} \right)^2 \tag{2.17}$$

Creation of Airy disc is described by equation 2.17. Where $I(\Theta)$ final intensity, I_0 is maximum intensity (Intensity of original light beam), J_1 is Bessel function of the first order, $k = \frac{2\pi}{\lambda}$ is the wave-number, a is radius of aperture and Θ is angle of observation.

$$x = k\alpha sin(\Theta) = \frac{2\pi a}{\lambda} \frac{q}{R} = \frac{\pi q}{\lambda N} \tag{2.18}$$

Where q is radial distance in focal plane, R is observation distance and $N = \frac{R}{2a} = \frac{R}{d}$ is f-number of the system. F-number is dimensionless number and it is also known as focal ratio, f-ratio, f-stop or relative aperture. It describes optical system by the ration between focal length and size of the entrance pupil. It is quantitative measure of the lens speed.

Airy discs are caused by the diffraction of the light on the circular aperture. Diffraction is described by Huygens-Fresnel principle. This prin-

ciple says how the light is diffusing in the space. It means that each point of advancing wave (electromagnetic, acoustic, mechanic, etc.) is considered as a source of new waves. Huygens-Fresnel principle provides us better understanding of the wave propagation and behaviour near the obstacles. In such simple case we can look at the light just from the view of ray optics but it is not correct. Due to the wave-particle dualism we have to think about the light also from quantum mechanical point of view.

2.2.2 ENZ Simulation – Fluorescence

Another way how to simulate PSF is using Extended Nijboer Zernike (ENZ) theory. Application of this theory allows us to simulate PSF under different condition [49, 50, 51]. We used MATLAB® codes that can be downloaded from http://www.nijboerzernike.nl/ [51]. These codes were proposed for simulation of the confocal microscope but we were also able to use them for simulation of standard light microscope. Theoretical behaviour of PSF can be described by following equation.

$$U(r,\phi,f) = \frac{1}{\pi}\int_0^1 \int_{2\pi}^0 e^{if\rho^2} P(\rho,\Theta) e^{2\pi\rho r cos(\Theta-\phi)} \rho d\rho d\Theta \tag{2.19}$$

Where $U(r,\phi,f)$ is intensity at point described by polar coordinates r,ϕ in distance f (defocus parameter) and $P(\rho,\Theta)$ is pupil function.

$$P(\rho,\Theta) = A(\rho,\Theta)e^{i\phi(\rho,\Theta)} \tag{2.20}$$

Where ρ and Θ are cylindrical coordinates, ϕ is aberration phase function $A(\rho,\Theta)$ is transfer function of the system. For simulation we are using discrete version of equation 2.19

$$U(r,\phi,f) = 2\sum_{n,m} i^m \beta_n^m V_n^m(r,f) cos(m\phi) \tag{2.21}$$

Where $V_n^m(r,f)$ is power-Bessel series, m,n are defining type of aberration and β_n^m is power or "weight" of aberration. Using equation 2.21 we can set-up many different parameters in the MATLAB® scripts. Basic param-

eters are type of aberration expressed by Zernike polynomials, distance of focal plane, and size of simulated area.

In mathematics, the Zernike polynomials are a sequence of polynomials that are orthogonal to unit disk. They are normalized according to eq. 2.22

$$\int_0^{2\pi} \int_0^1 Z_j^2 \rho d\rho d\theta = \pi \tag{2.22}$$

Where Z is Zernike polynomial and j is Noll's index.

2.2.2.1 Aberration

Optical aberration occurs in an optical system when light from a point source does not converge to (or does not diverge from) a single point after transmission through this optical system. Optical aberration is caused by different optical properties of the part (or whole) of the optical system.

There are two different types of optical aberrations - monochromatic and chromatic [37]. Monochromatic aberrations are caused by the geometry of the lens and occur both when light is reflected and when it is refracted. They appear even when using monochromatic light. Chromatic aberrations are caused by dispersion, the variation of a lens's refractive index with the wavelength. Chromatic aberration does not appear when the monochromatic light is used.

Tilt

Tilt is a deviation in the direction a beam of light propagates. This can be caused when the axis of the lens is not parallel to the plane of the sample. Tilt quantifies the average slope in both X and Y directions of a wavefront or phase profile across the pupil of an optical system (Fig. 2.10). Tilt can be expressed as Zernike polynomials (Eq. 2.23, 2.24):

$$X - Tilt : Z_2 = 2\rho cos(\theta) \tag{2.23}$$

$$Y - Tilt : Z_3 = 2\rho sin(\theta) \tag{2.24}$$

Figure 2.10: Scheme of Tilt Aberration. Green line is our plane of interest and red line is actually focused position.

Defocus

Defocus simply means shift along the optical axis (Fig. 2.11). This means that object is not in perfect focus. Defocus aberration blurs the image, reduce the sharpness and contrast of the image. The sensitivity of the optical system to the defocus parameter depends on the depth of focus. If the focus depth is very shallow (typically in high magnification) the system is very sensitive. Even small shift causes big blurring. Defocus can be modelled by Zernike polynomial (Eq. 2.25)

$$Z_4 = \sqrt{3}(2\rho^2 - 1) \tag{2.25}$$

Figure 2.11: Scheme of defocus aberration. Green line is our plane of interest and red line is actually focused position.

Astigmatism

The optical system has astigmatism aberration if the lens is not symmetric and the rays are propagated differently in two perpendicular planes. In case of astigmatism there are two different focal point one for horizontal and one for vertical plane. There are two different form of astigmatism. First one occurs for objects away from optical axis and even if the optical system is perfectly symmetrical. This one is the third-order aberration. Second type of astigmatism occurs when the optical system is not symmetrical about the optical axis (This one is usual in human eyes). This aberration can be corrected by using cylindrical lenses. Following equations are describing the case of symmetrical optical system (third-order aberration).

$$Z_5 = \sqrt{6}\rho^2 sin(2\theta) \tag{2.26}$$

$$Z_6 = \sqrt{6}\rho^2 cos(2\theta) \tag{2.27}$$

Coma

Coma (comatic aberration) is caused by imperfection of lenses and it is created by off-axis light source (Fig. 2.12). The light rays entering the lens are diffracted irregularly this means that the object will have tail. Coma can be also function of wavelength, in that case it is a type of chromatic aberration.

$$Z_7 = \sqrt{8}(3\rho^3 - 2\rho)sin(\theta) \tag{2.28}$$

$$Z_8 = \sqrt{8}(3\rho^3 - 2\rho)cos(\theta) \tag{2.29}$$

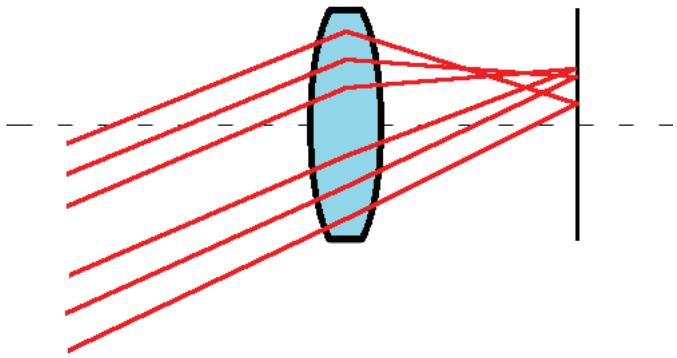

Figure 2.12: Scheme of Coma Aberration

Spherical aberration

Spherical aberration is caused by different refraction of light rays in the central part of the lens and on the edge (Fig. 2.2.2.1). The effect of spherical aberration can be minimized by using of the combination of convex and concave lenses or by using so called aspheric lenses. Zernike polynomial for spherical aberration:

$$Z_{11} = \sqrt{5}(6\rho^4 - 6\rho^2 + 1) \tag{2.30}$$

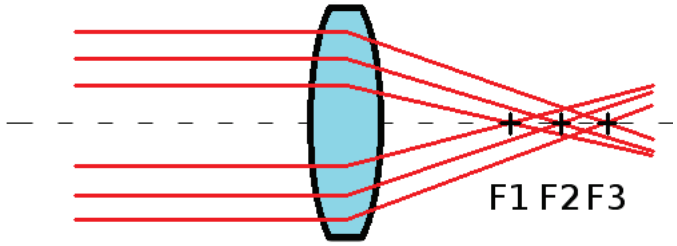

Figure 2.13: Each part of lens in different distance from optical axes has different focal point. F1, F2 and F3 are different focal points.

Results of simulation of given aberration are in section 5.2.

Field curvature

Field curvature is optical aberration which projects flat plane on the curved plane. This means that we are not able to focus whole flat object, but only the center or the edge.

Chromatic aberration

Chromatic aberration (achromatism, chromatic distortion) is type of distortion when the lens does not transfer correctly all wavelengths. Each color of spectrum is transferred through the lens differently and has different focus (Fig. 2.14).

This aberration can be corrected by using two lenses, usually one concave lens of flint glass and second convex lens made of crown glass. Another correction of chromatic aberration can be done by using some diffraction elements with exactly opposite aberration.

It is possible to combine simulations of different aberrations to obtain complex behaviour of the optical system. Using these combinations we can try to obtain the same shape of the PSF by the simulation as we obtained

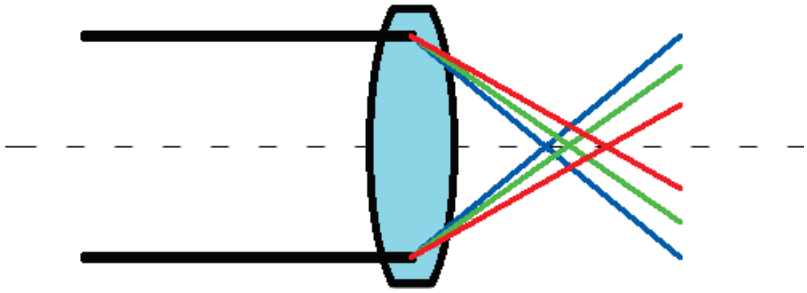

Figure 2.14: Different wavelength has different focal point. Shorter wavelengths have shorter focal length.

by real measurement. It is not easy to find exact combination of aberration to simulate real behaviour of microscope because of many different optical elements.

2.3 Image processing and analysis

2.3.1 Segmentation algorithms

The task of segmentation algorithms is to separate object(s) of our interest from its background on the basis of their different properties. These algorithms usually results in black-and-white (logical) images where pixels of intensity 1 (white color) and 0 (black color) correspond to the detected object and background, respectively.

Different colors

The easiest way of the object's detection is in case of the object's different color (intensity), where the proper color channel is only selected 2.15.

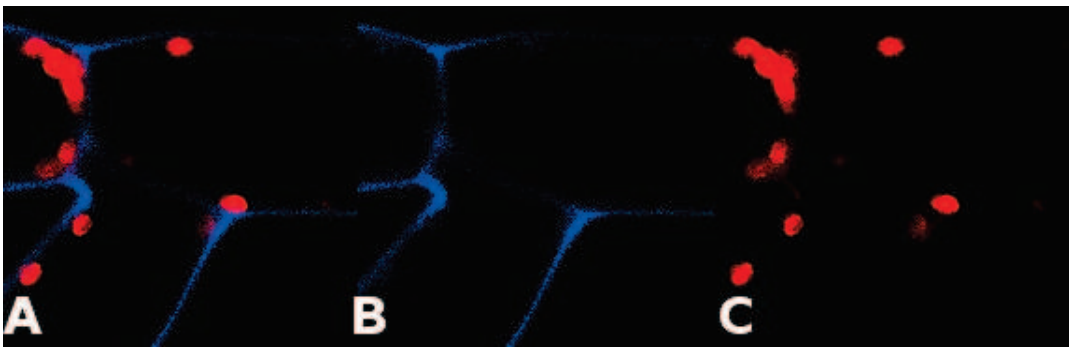

Figure 2.15: Detection based on the different color channel. A – Red and blue channel together, B – blue channel separated (mainly cell walls), C – red channel separated (mainly cell nuclei).

Clustering methods

Clustering methods are based on the assumption that objects' and background's pixels belong to different clusters. One of these methods is K-mean clustering, which iteratively divides an image into K clusters [52]. The first step of this algorithm is a selection of cluster centres. This can be done randomly or by some analysis. In the second step, each pixel is assigned into one of the clusters due to the minimization of the distance between the pixel and the cluster's centers. In the third step, the centres are recalculated by averaging the position of all pixels in the cluster. Steps two and three are repeated while changes of pixels in the clusters occur (i.e., until convergence is attained).

The basic questions of this algorithm is the setting the number of clusters (i.e., the number of possibly detected objects) and position of the clusters' centres. These initial conditions can influence the results of the clustering.

Compression-based methods

There are two compression methods, which work in different way. The loss compression is based on replacing pixels of the same or similar properties (color and intensity) by block of pixel. The similarity of the pixels is given

by the level of compression (or vice versa). The lossless compression finds the way how to encode regions of the same property without describing all pixels and without any loss of data. These regions can be taken as separated objects.

Histogram-based methods, thresholding of intensities

These methods are fast and effective because they do not require to go through all pixels repeatably. The information on the number of pixels of the same intensity is given by the histogram. By the analysis of peaks and valleys of histogram we can separate image into several clusters by the similarity in intensity.

One of Histogram-based methods is an intensity thresholding of the image. If the object and the background have the same color but different intensity some of thresholding methods has to be used(2.17). That means that all pixels with value lower (in case of dark object and light background) or higher (in case of bright object and dark background) than the threshold belong to the object and the others are located in background.

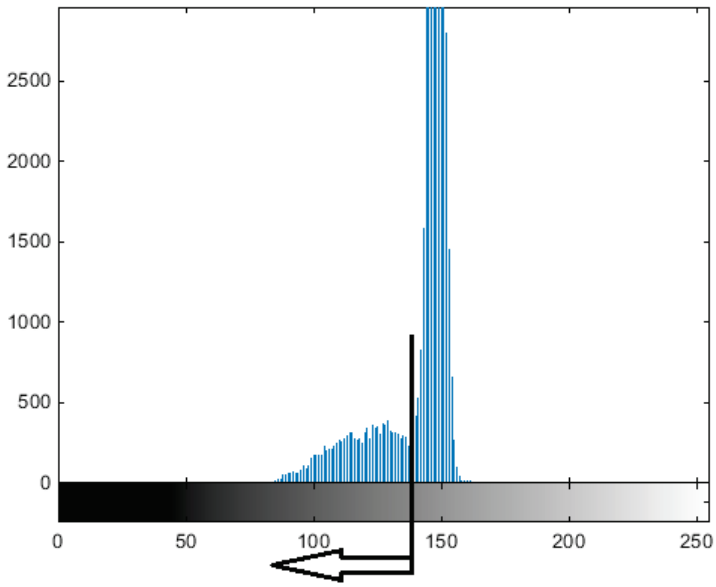

Figure 2.16: Histogram of image 2.17B. Black line shows value of Otsu threshold and arrow shows values that remain in the image 2.17C

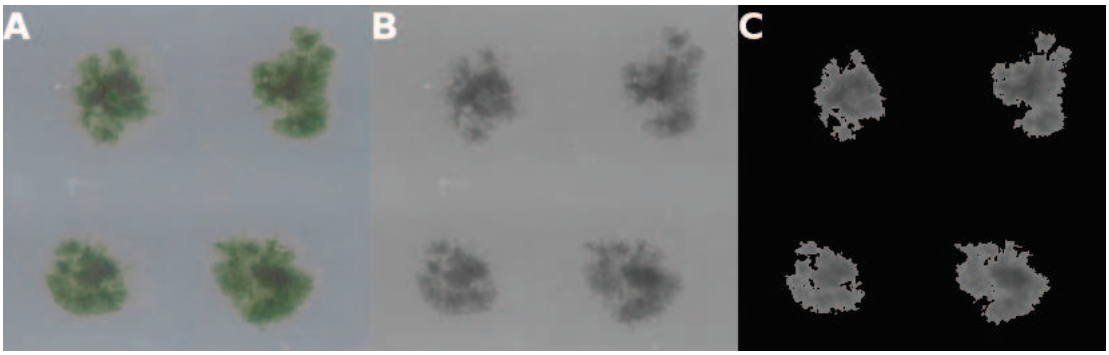

Figure 2.17: Example of threshold. A - original image, B - green channel, C - green channel below Otsu threshold.

There are several methods how to select the threshold in the histogram. One of the mostly used methods is Otsu thresholding [53] (2.17, 2.16), another is balanced histogram or looking for maximum or minimum value in histogram or looking for some valley in it.

Edge detection

On the edges (borders of the object) there are intensity gradients. The object can be detected by its borders. The problem is that the edges can be disconnected, but the object is closed (border of the object is one line). So when the edge detector is applied on the image further processing (like morphological operation) of the result must be done.

Watershed Transformation

The grayscale image can be consider as a topological surface. The watershed transformation is based on flooding of this surface. Flooding starts from the minima and it is forbidden to mix the water coming from different sources (2.18). What will remain after these operation are the borders of different regions [54]. There are several modification of this algorithm like waterfall and others [55].

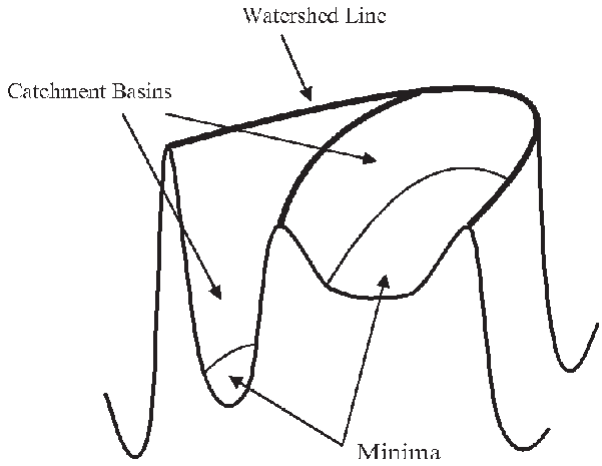

Figure 2.18: Illustration of watershed algorithm

Trainable segmentation

Under the trainable segmentation can be hidden different algorithms like active shape model (ASM), genetic algorithms or neural network algorithms. This trainable segmentation is based on machine learning.

In case of ASM you manually define the shape of the object in training image and the algorithm is trying to search for the same shape in other images. This can be used on the images where the objects have significant borders and they can vary in size and very little in their shape. [56]

Genetic algorithms in image processing can be used for different purposes, for example for image segmentation [57], clustering [58] or thresholding [59].

Opposite to this can be neural networks. For their utilisation it is necessary to have training set manually annotated by some user and some basic settings of the weights on each neuron. Neural network learning involves the changes of the initial weights on each neuron to obtain the same results as in testing set [60].

2.3.2 Deconvolution

Every image can be consider as combination of the original image and image distortion (for example PSF). This combination can be described by the equation 2.31.

$$f \cdot g = h \tag{2.31}$$

where f is original image, g is convolution function and h is obtained image. Usually the situation is little bit complicated by the noise (Eq. 2.32).

$$(f \cdot g) + \epsilon = h \tag{2.32}$$

where ϵ is noise. Deconvolution is process of removing of the distortion from the image. In mathematical way it is looking for the function g^{-1} in case of eq. 2.31. In case of eq. 2.32 it is necessary firstly remove noise ϵ and then find the g^{-1} function. In microscopy (and in other imaging techniques such as astronomy) we can consider that the g function (convolution kernel) is the PSF. If there is a possibility to measure the PSF we can use this for deconvolution. If not there exist technique called blind deconvolution. This is mathematical technique where the convolution kernel is estimated. Blind

deconvolution is iterative method where the estimated deconvolution kernel is improved in some steps. Improving of the deconvolution kernel continues until there is no statistical improvement of the final image.

2.3.3 Entropy

Advanced image processing methods are based on calculation of entropy values. Different types of entropy can be used for different purpose. Edges in the images can be detected by calculation of Havrda and Charvat's entropy [61] or Shannon entropy [62] or Rényi entropy [63]. Calculation of Tsallis entropy can be used for thresholding of image [64, 65] or for image segmentation [66]. Calculation of Shannon's and Renyi information entropy can be used for measuring of the information content of the images.

Information entropy approach to image processing was developed on our institute by Jan Urban [67, 68]. It was used for image enhancement and especially for improving visibility of borders of the objects. It also can be used for enhancing or extraction of different features in the image [69, 70, 71, 72, 73, 74]. It was based on Shannon Information Entropy [75] (equation 2.33).

$$H\left(S\right) = -\sum_{i=1}^{n} P(s_i) \log_2 P(s_i) \tag{2.33}$$

We decided to extend this approach by using Rényi Entropy(equation 2.34) because the Shannon Entropy is special case of Rényi Entropy for $\alpha = 1$.

$$H_\alpha(X) = \frac{1}{1-\alpha} \log \left(\sum_{i=1}^{n} p_i^\alpha \right) \tag{2.34}$$

Calculation of different entropies can be used for statistical texture feature extraction [76]

Comprehensive description of the Rényi entropy for extraction of details of the image is reported in [77].

3 Aims

Aim of this thesis is to introduce methods for better discrimination of the objects in the microscopic images. These methods will be demonstrated on the nanoparticles.

The way to develop and describe methods for analysis of microscopy images starts with the understanding how the image in the microscope is created. It is necessary to make simulation of different aberrations and analyse this results. Comparison of the simulations and real experiments must be done.

Next step is to develop algorithms for advanced image analysis using information entropy and also algorithms for image conversion. It was also necessary to develop algorithms for automatic detection of PSF and apparent PSF core.

Different models of PSF has to be created for better understanding behaviour of PSF.

All gained knowledge will be applied on the results from real experiments.

4 Methods and Materials

4.1 Equipment

Nanoscope

Microscopy was performed using a versatile sub-microscope: a nanoscope, developed for the School of Complex Systems FFPW by the company Optax Ltd. (Czech Republic). The optical path consisted of two Luminus 360 light emitting diodes, the condenser system, a firm sample holder, and an objective system made of two complementary lenses that allow a change of distance between the objective lens and the sample. Next, a projective lens magnified the image to project on the 4872 x 3248 point camera chip. The latter arrangement was necessary to achieve the expected resolution without losing the size of the observed scene. The size of the original camera pixel using 60x primary magnification was 20 x 20 nm, and the size of the final pixel after de-mosaicing was 40 x 40 nm. During the experiment, the optical system was facilitated by an infrared and UV filter. The z-scan was performed automatically by the programmable piezo mechanics, and the step size was 100 nm. The microscope driving software was programmed for the given experimental setup and allowed complete mechanical control over the experiment as well as over storing the primary signal from the camera.

Confocal Laser Scanning Microscope (CLSM)

The fluorescent images were obtained by using Leica TCS SP5 DM-6000 CS which is located in Core Facility Cell Imaging and Ultrastructure Research, Faculty of Life Sciences at University of Vienna. Protocols of experiments can be seen in Appendix A.

4.2 Materials

Nanoparticle – $0.14\mu m$

Fluoresbrite Carboxylate microspheres 2.5% solid latex, size $0.14\mu m, sd = 0.01$, polyscience, inc. Warrington, pa, $cat.\ number = 17146$

Nanoparticle – $0.22\mu m$

FluoSpheres, carboxylate-modified microspheres, 2% solids, crimson fluorescent (625/645), size $0.22\mu m$, Molecular Probes, Eugene, Oregon, USA, Leiden, The Netherlands

Nanoparticle – $0.53\mu m$

Fluoresbrite Carboxylate microspheres, size $0.53\mu m, sd = 0.009$, polyscience, inc. Warrington, pa, $cat.\ number = 18339$

Nanoparticle – $1.17\mu m$

Fluoresbrite Carboxylate microspheres 2.5% solid latex, size $1.17\mu m, sd = 0.04$, polyscience, inc. Warrington, pa, $cat.\ number = 17458$

Agarose specification

1% concentration Agarose Type I-A Low EEO Sigma chemical company, St. Louis, MO 63178, USA

4.3 Software

Matlab

All algorithms were developed and tested in Matlab® developed by MathWorks Inc [78]. Two different versions were used – Version 7.0.4.365 (R14), service pack 2, January 29, 2005; and Version R2014b (8.4.0.260532), 64-bit, September 15, 2014.

Entropy Calculator

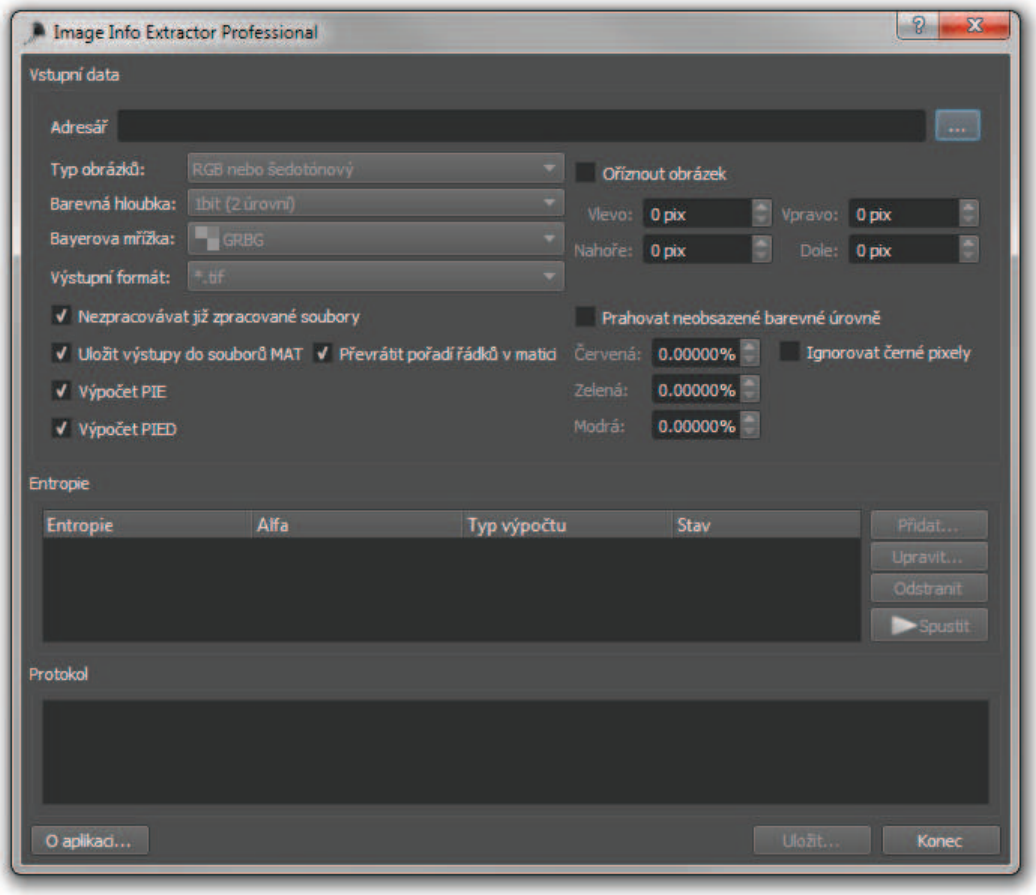

Figure 4.1: Screenshot of Entropy Calculator GUI.

One of the software developed on our institute during this work is Entropy Calculator. It is designed for calculation point information gain and derived quantities [77] of single image or series of images. On Fig. 4.1 it is shown that it has many different settings. It can works with different types of images – coloured (RGB) images, greyscale or black and white images or RAW images. Images can also have different bit depth – 1 bit (Black-White images), 8 bits, 12 bits or 16 bits. When raw images are used proper Bayer mask of the camera can easily selected. It is possible also to crop the images or to omit intensities with exceptionally low occupancy (designed for removing of defect camera pixels). In the settings of Entropy calculation there are also different parameters to set up. PDG or PIG can be selected (see more details about Information Entropy Calculation in section 5.1). For calculation of syntactic entropy different neighbourhood can be selected – cross, rectangle, elliptic.

LIL Convertor

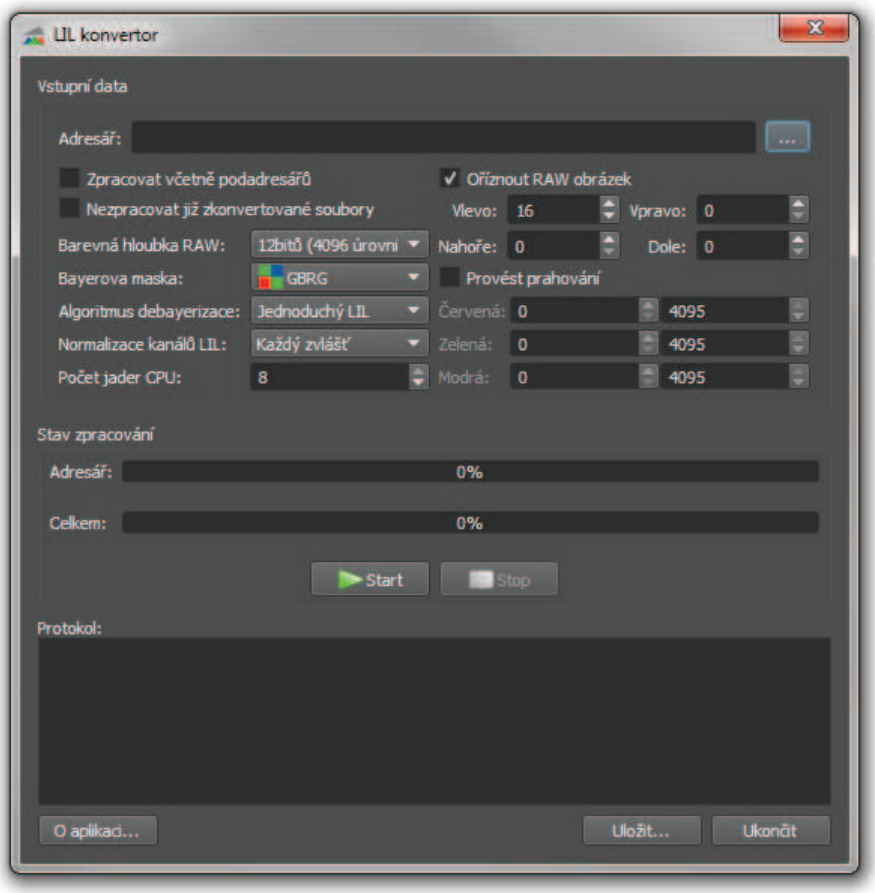

Figure 4.2: Screenshot of LIL Convertor GUI.

LIL Convertor allows to convert images with bit depth than higher 8 down to 8 bit. Algorithm is described in details in the section 5.1.

On the Fig. 4.2 is shown the the graphical user interface(GUI) of the software. It is possible to load RGB images, grayscale images even RAW images. If RAW images are loaded appropriate Bayer mask can be selected. Images can be cropped or (and) threshold and normalization of color channels can be applied. It is possible to normalize color channels either separately or together. The program is optimized for using multi core CPUs.

There are several possibilities how LIL (Least Information Loss) conversion can be applied on the image or series of images.

Color channels can be normalized together for keeping the same ratio between color channels. This means that the empty (unoccupied) levels are removed only in case that they are empty in all channels.

If color channels are normalized separately more information in the image are preserved but information about color is completely destroyed.

Part of the LIL Convertor is also algorithm for debayerisation for processing of RAW image. There are five options, four for different bayer mask and one for grayscale image.

Threshold can be applied on images in case of removing defect camera pixels - both bright or dark.

Last option is cropping of the image. Camera use some rows or columns for calibration of digital noise. This part of the image should be removed because it does not contain any relevant information. This can be used also for selection of part of the image that will be processed.

4.4 Experiment Description

The experiments were planned according to results of the simulations. All experiments were done on our microscope (which was described above, sec. 4.1) with different settings and with different samples. First step was the preparation of the samples. In the analogy to the use substitute for light point, i.e. fluorescent particle, source small latex particles were used. Latex particles had $0.22\mu m$ in diameter and were obtained in dense solution from our partner institute - University of Vienna, Core Facility Cell Imaging and Ultrastructure Research (See the specification of all used particles in Section 4.2).

It was necessary to dilute these solutions to obtain images of separate particles. Dilution ratio was 1:9. High resolution camera was used. Size of the image was 4872x3248 pixels before applying Bayer mask. Size of the pixel in the original grayscale image is 19nm x 19nm,p after RGB conversion is one half of the original. This means that in original image the size of the particle

of $0.22\mu m$ is diameter should be around 10 x 10 px and after the conversion approx 5 x 5 px. Best results were obtained with using dried samples. After drying nanoparticles are stable and do not move during experiments. This state allows to scan the same particles on the same position under different light conditions. The intensity of the light was changed via changing current on the LEDs. Current was changed from 1000mA to 3500mA with the step of 500mA to see the real dependency on the light intensity. The LED diode current is used instead of any light intensity units as we do not have any independent way for the calibration of the microscope camera and there is also no way to calculate the light intensity after the passage through the camera optics. Main experiments described in this article were done with $0.22\mu m$ particles. Further image series of $0.14\mu m$, $0.53\mu m$ and $1.17\mu m$ latex particles were also performed. Experiments using $0.02\mu m$ nanogold particles were not reported as we have never been able to achieve sufficient stability of the object on the microscope glass and it was also difficult to discriminate between the real object and, perhaps, non-idealities in the glass itself. Image series were taken as z-scans in bright field microscopy.

In all cases the point divergence gain entropy calculation was performed to extract maximum information from every image[77]. After this processing MATLAB ® script for 3D reconstruction was applied. Due to construction of our microscope different wavelengths of light cannot be used. Instead of using different wavelengths illuminating light images were processed according to sensitivity of the camera chip to different wavelengths (separation to color channels - R, G, B).

Experiments on Confocal Laser Scanning Microscope (CLSM) were made to have the comparison between bright field and fluorescent microscopy. These experiments were done on equipment of our Vienna partner under supervision of Mag. Dr. Wolfram Adlassnig, MBA and Mag. Stefan Sassmann. The CLSM was Leica TCS SP5 DM-6000 CS. Different sample preparations were tested. The best results were obtained when particles were stabilized by using agarose (See the specification in Section 4.2, see the results in section 5.4.2).

5 Results

5.1 Developed Algorithms

Nowadays the limit for the discriminability of object by the microscope is ultimately the size of a projected area on a pixel at the camera chip. If there is no possibility to change camera to increase resolution it is need to use another techniques.

The physical limits considered so far certainly apply. The use of using monochromatic (single wavelength) light exercises the superposition of various PSF geometries which limits the intelligibility of the image. For this effect you can imagine superposition of images on the figure 5.14.

Next step is using lower wavelength contributes the slimness of he PSF which was in according to equation 2.9.

The effect of microscopy with videoenhancement (VEM) is less clear. The method is based on increase of the intensity of light in the brightfield microscopy [12, 14]. Effect of VEM can be seen on the figure 5.26. It is quite clear that the effect can not be attributed solely to the improvement of the signal to noise ratio [12] but some effects in the realm of quantum mechanics should be considered. A rough explanation was proposed by Lipson [14], but it is quite likely that proper interpretation should be sought by the weak experiment theory [79].

If these methods provide still not sufficient to detect desired image details there exist respective image processing algorithms. One of them is based on series of images with sub-pixel shift. If there were some object just on the border of two or four pixels after sub-pixel shift the object is on one pixel resp. on the border of two pixels depending on the direction of the

shift. When we make shifts in all possible direction and then combine all images together the resulting image will have better resolution.

Entropy Calculation

The area corresponding to one particles is small (as mentioned in section 4.4) which in effect means that it deviates from the rest of the image in relatively negligible way. It is necessary to use some image enhancing approach. One of the ways is to use point information gain, the information contribution by one pixel, to measure information carried by each pixel in the image.

Principle of calculation of information carried by the image point was described in a few articles [80, 81, 77]. It can be calculated as simple difference of the information calculated from the whole image and from the image with out that particular pixel.

$$PIG_{\alpha,x,y} = \frac{1}{1-\alpha} ln \left(\sum_{i=1}^{n} p_{i,x,y}^{\alpha} \right) - \frac{1}{1-\alpha} ln \left(\sum_{i=1}^{n} p_{i}^{\alpha} \right) \tag{5.1}$$

Where α is Rényi parameter, $p_{i,x,y}^{\alpha}$ and p_{i}^{α} are probabilities of occurrence of given intensity in the image without and with the examined point.

$$PIE_{\alpha} = \sum_{j=0}^{m} \sum_{i=0}^{n} PIG_{\alpha,x,y} \tag{5.2}$$

Where m is number of points in x direction and n is number of points in y direction and $PIG_{\alpha,x,y}$ is calculated according equation 5.1

See the example of entropy transformation on Fig. 5.1.

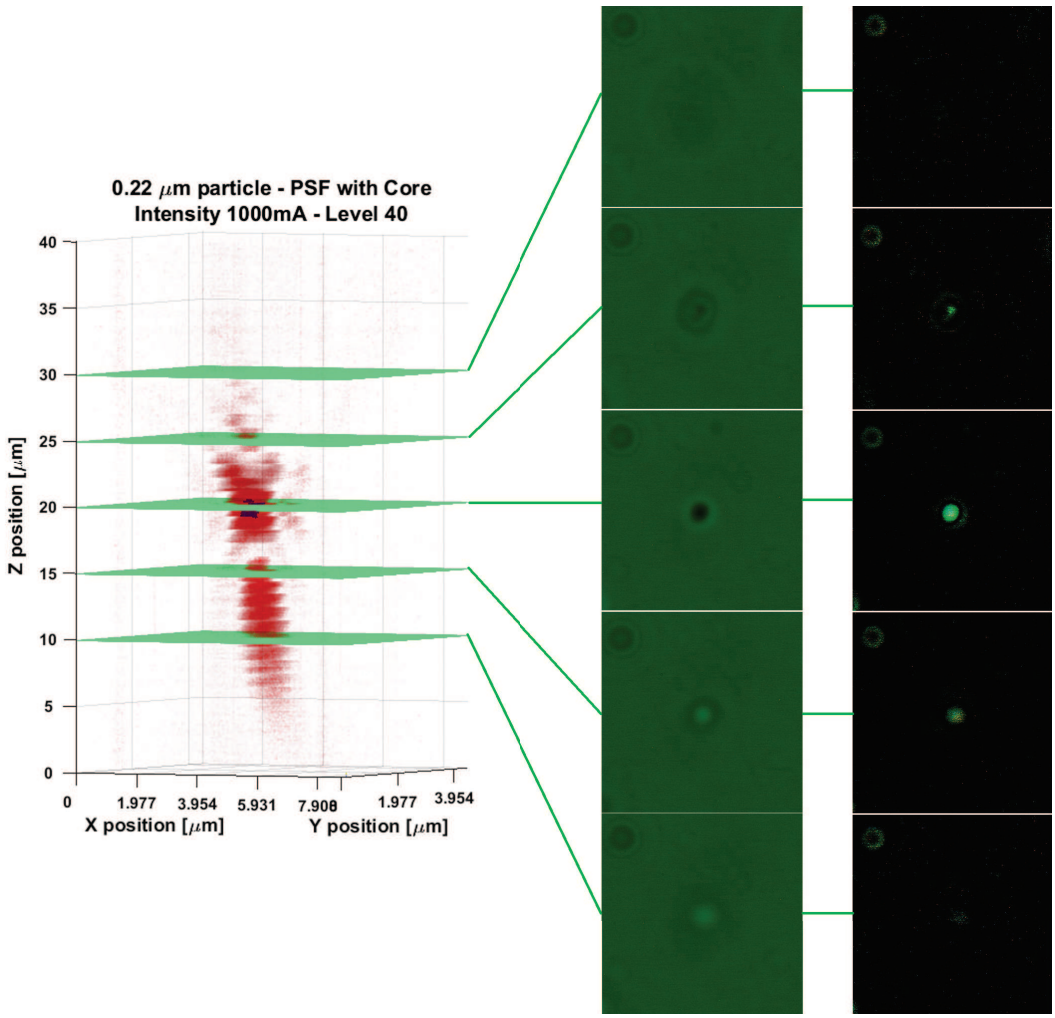

Figure 5.1: This image shows PSF reconstruction of $220nm$ on the left, original images in the first column. Entropy transformed images are in the right column. The Rényi parameter α was 0.5.

Calculation of PDG (Point Divergence Gain, eq. 5.3), calculation of the change of information between subsequent images, was also introduced. This calculation quantifies the diversity, uncertainty, and randomness in 3D space.

$$PDG_{\alpha,x,y} = \frac{1}{1-\alpha} log_2 \frac{\sum_{i=1}^{n} p_i^{\alpha}}{\sum_{i=1}^{n} p_{i,x(l+1),y(l+1)}^{\alpha}} \tag{5.3}$$

Sometimes the resulting image of calculation of information entropy has dense histogram. This means that intensities in same regions are almost the same. In this case human eyes may not be capable to discriminate the difference but for automatic (computer) processing is a solution. And the calculation of the point information gain using different α coefficients not only allows to discriminate and enhance all possible discriminable regions but also may be used for quantification of local discriminability, i.e. by calculation of minimal α step which lead to resolution of two least different intensity occurrences.

In this thesis the calculation of the point information gain may also be understood as a tool for image transformation allowing visual comparison of images of diffracting objects and light emitting objects. This is usually a complicated task. While the image of the light emitting object exhibits the smallest projection of the point spread function and the highest electromagnetic field intensity at the same position in space, in the image of the diffracting object the smallest object should coincide with the lowest electromagnetic field intensity (not in all cases, but at least in the case of very small objects exhibiting Rayleigh diffraction rules). In the image transformed into point information gain levels the smallest object - i.e. rarest, contributing by highest information, - is the most intensive and the apparent focal plane is also attributed to the most intensive object. The discrepancy mentioned above is, in fact, overlooked even by the major microscope producers and leads to different results of the autofocusing software for fluorescent and diffracting detection of the same object.

Least Information Loss (LIL)

Camera can usually provide some kind of RAW image. This should be information with minimum changes read from the camera chip. Such image is often unavailable for visual inspection on the computer screen. In order to preserve maximum of the information for visual inspection we developed the LIL algorithm.

In our case information obtained by the camera is 12bit grayscale

(intensity) image. First step is applying the Bayer mask on the grayscale image. Each pixel in the image is formed from 4 camera pixels, one is dedicated to blue color, one to red and two others are green. Standard processing of the image gives the same resolution as the camera chip has but some pixels are interpolated.

The idea of LIL conversion is not to introduce any information to the RAW image, no interpolation is used (see Fig.5.2). The resulting image has quarter size(half resolution in both X and Y direction). RGB image, still 12bit in our case, is obtained after applying of the Bayer mask. Last step is the 12bit to 8bit conversion which is necessary for displaying of the image but not for processing.

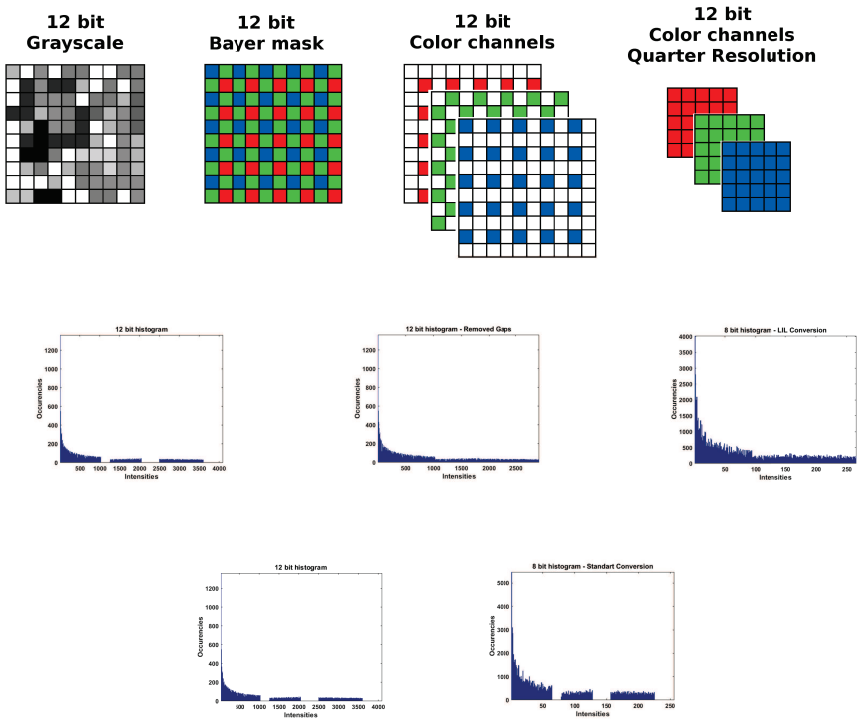

Figure 5.2: Scheme of LIL Conversion. First row shows processing of the image obtained directly from camera chip. First image shows information from camera chip, second image shows applying of the Bayer mask. Third images is creation of RGB image from Bayer mask. Fourth image shows RGB image of quarter resolution of the original image. Graphs in the second rows shows principle of LIL conversion. First graph is histogram of original 12bit image. Second graph is histogram of the image after removing unoccupied intensity levels. The last graph in the second row is histogram of the LIL converted 8bit image. Bottom row shows standard conversion of the 12bit image to 8bit image.

The main idea of the algorithm is based on the assumption that in images with bit depth higher than 8 are usually some levels unoccupied (Tab.5.1,5.2, Fig. 5.4,5.6). In standard conversion all levels are converted, regardless to their occupancy. We suggested that the number of converted intensity levels can be lowered if unoccupied levels are removed. Then the merging of intensity levels follows. This will change the color of the image

but this is not relevant for automatic image processing. In the worst case when all intensity levels in the 12bit image are occupied the result of the LIL conversion will be the same as standard conversion.

Information about removed and shifted intensity levels are stored in EXIF in each image file. This can be used for backwards conversion.

Theoretical example of conversion

12bit image has $2^{12}(= 4096)$ intensity levels in each color channel. 8bit image has $2^8(= 256)$ intensity levels. During standard conversion $16(\frac{2^{12}}{2^8} = \frac{4096}{256} = 16)$ levels must be merged to one level. Usually not all levels in 12bit image are occupied.

If the image has for example half occupied levels $(2048 = 2^{11})$ only 8 levels are merged into one. This means that in the image converted by the LIL approach more information is preserved.

Practical example of conversion

Applying LIL conversion on real image will results in image with changed colors (Fig.5.3,5.5). In case that color information in the image is needed LIL conversion cannot be applied. When the camera is used as a kind of spectrometer (images taken by camera have the pseudo-colors) LIL conversion can helps.

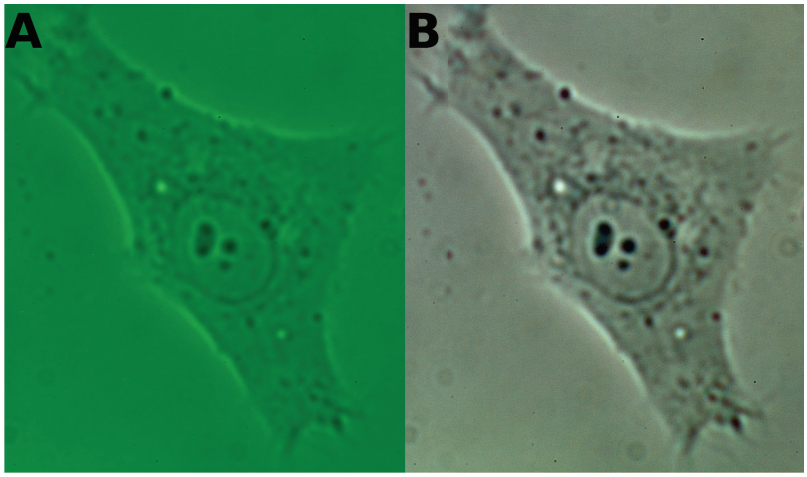

Figure 5.3: Example of LIL Conversion. A Standard 12bit to 8bit conversion, B LIL Conversion

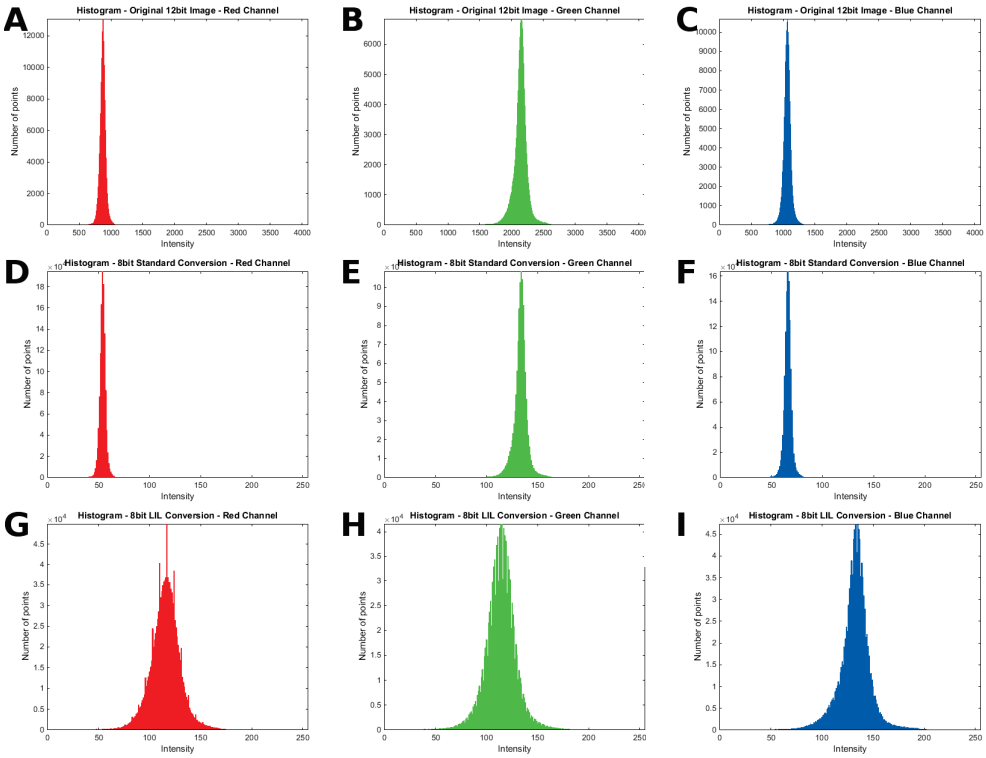

Figure 5.4: Histograms of images: A-C Histograms of Original 12bit image, D-E Histograms of 8bit image with standard conversion, G-I Histograms of LIL Converted 8bit image. All rows from left to right: Red channel, Green channel and Blue channel of the image.

Table 5.1: Occupied levels - HeLa Cell

	Red Channel	**Green Channel**	**Blue Channel**
Original 12bit Image	805	1735	956
8bit Image Standard Conversion	84	132	89
8bit Image LIL Conversion	256	256	256

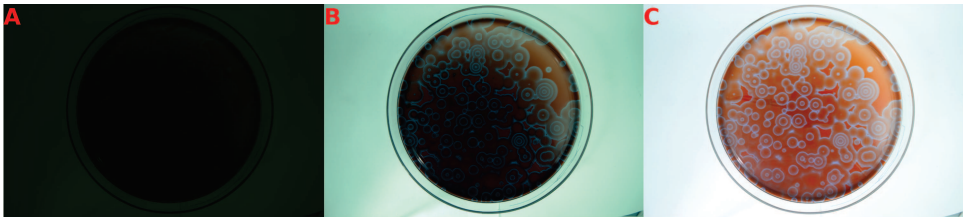

Figure 5.5: Images of different conversion of images of BZ reaction. A - Standard conversion, B - LIL conversion, C - NEF to PNG conversion

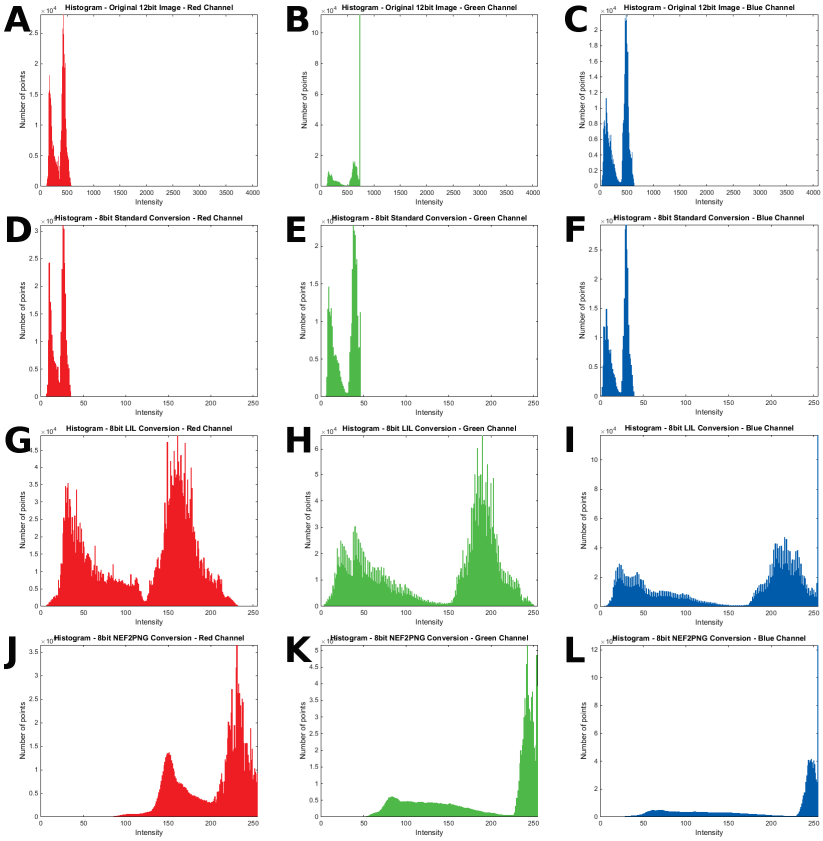

Figure 5.6: Histograms of images: A-C Histograms of Original 12bit image, D-E Histograms of 8bit image with standard conversion, G-I Histograms of LIL Converted 8bit image, J-L Histograms of NEF to PNG conversion. All rows from left to right: Red channel, Green channel and Blue channel of the image.

Also standard RAW images can be used. As an example the NEF (Nikon RAW format) was converted(Fig. 5.5). On the Fig. 5.6 can be seen how standard procedures transform the image. The number of occupied level in each image is shown in Tab. 5.2.

Table 5.2: Occupied levels - BZ Reaction

	Red Channel	**Green Channel**	**Blue Channel**
Original 12bit Image	524	648	633
8bit Image Standard Conversion	37	42	41
8bit Image LIL Conversion	256	256	256
8bit Image - NEF to PNG Conversion	187	214	244

Detection of Apparent Point Spread Function Core

Detection of the core is based on calculation of the PDG and analysis of the images. If the object is compact and the step between two images is smaller than the size of the object we can say that image of this object will not change between two steps. Because PDG calculates information changes between two images only points with PDG value zero are considered as valid points. These points are used for creating binary mask. Next step is making 3D model using binary masks - PDG model. Once the PDG model is created the core of the object can be found. The assumption is that the image of borders of the object will have the same intensity. This means that after the contour plot of the image is made the most darkest contour of the model can be selected. The darkest part is selected because diffraction of the light on the object is registered.

The complete interpretation of observed structures is, nevertheless, rather complicated. Even in the case of single object they of finite size the are result of Mie scattered wavefronts imaged by the lens system. Although it is still true that the darkest point lies behind the center of the object, the interference pattern behind the object may be rather complicated and their projection by the lense is basically unpredictable. Thus the apparent PSF core is the best option for the interpretation of the result.

Principle of the detection of core in one image is shown on Fig. 5.7 in 3D it is on Fig. 5.8. The position of the detected core is inside region in which the PSF is most compact (Fig. 5.10) and is analysed with respect to the intensity.

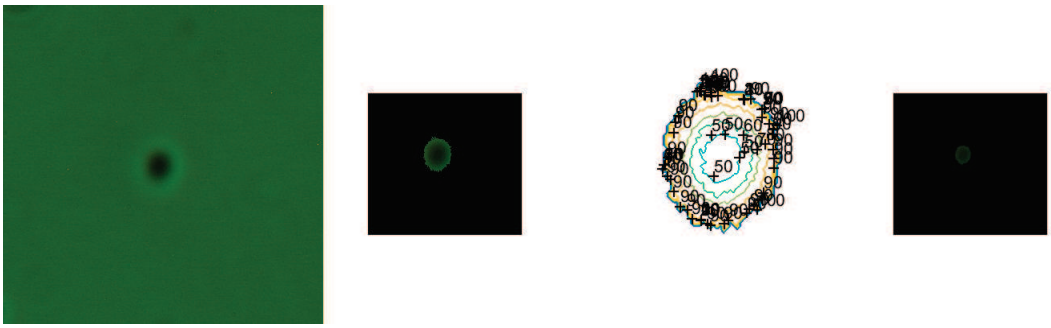

Figure 5.7: Principle of PSF Core detection. Left image is the original image. Latex particle $220nm$ in diameter and at light intensity $2000mA$. Second image from the left shows which part of the original image is stable (has no changes) during the PDG analysis. Third image is contour plot of the stable part. The right image shows area inside the contour 60.

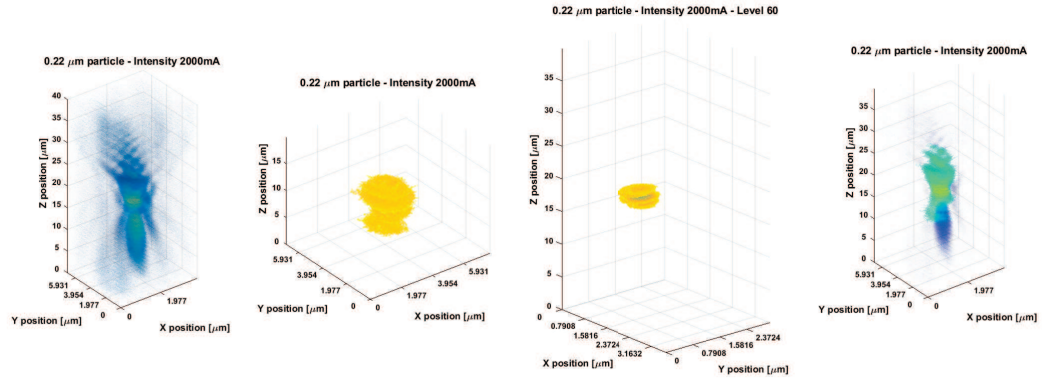

Figure 5.8: Principle of PSF Core detection 3D image. Latex particle $220nm$ in diameter and at light intensity $2000mA$. Left image is the original PSF. Second image from the left is 3D PDG model Third image is 3D reconstruction of the core at contour 60. The right image shows all three images in one.

It can be proven that selection of the darkest contour in the PDG model corresponds to the center of the object image(Fig. 5.10). The calculated volume of the $220nm$ latex particle and the measured volume of 3D reconstruction of it's detected core shows that the smallest contour has smaller diameter than the ball (Tab. 5.3).

Results of 3D reconstruction of PDG models under different light intensity are shown on Fig. 5.9. These PDG models were used for detection of the cores and calculation of their volumes(Tab. 5.4). The Tab. 5.4 shows the light dependency.

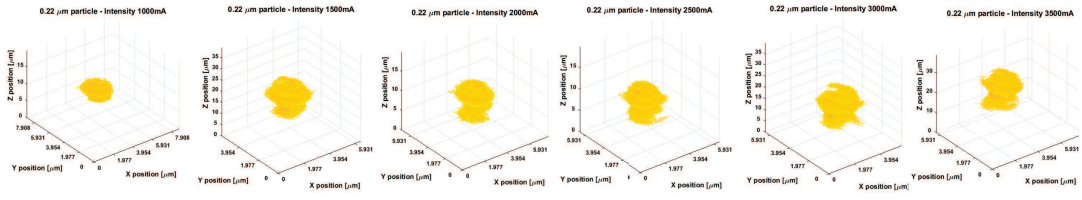

Figure 5.9: PDG model under different light condition. Intensity of the light on the left image is $1000mA$. Intensity is increasing from left to right with step $500mA$ till $3500mA$ on the right image.

Table 5.3: Volume (μm^3) of detected PSF, PDG and CORE at intensity 2000mA. Comparison with size of the real particle.

	Volume (μm^3)
PSF	1469.961
PDG	27.13051
CORE at cont. 60	0.956652
CORE at darkest cont.	0.00297
Real Particle	0.005575

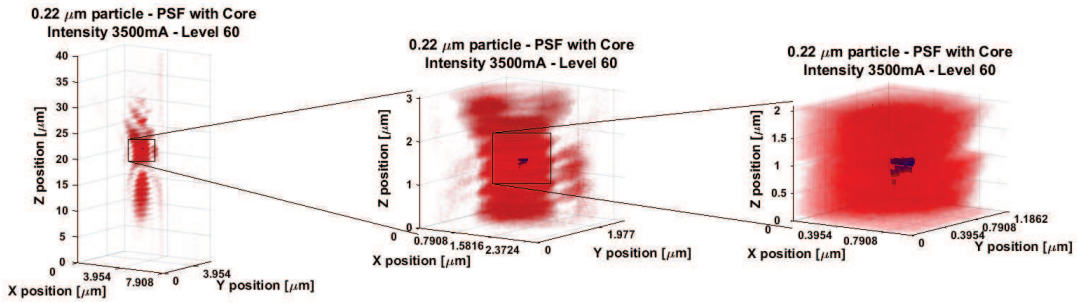

Figure 5.10: Detection of PSF core - detailed view. Red part is whole PSF, blue part is detected core (real particle).

5.2 Models

Airy Disc

This simulation gives us information how the PSF looks like in the plane of the particle (Fig.5.11). This plane may be called as Airy focal plane. But problem of this method is that we cannot simulate behaviour of the microscope and we are not able to obtain simulation in different focal plains. Shape of PSF in different focal planes can help us to find objective

Table 5.4: Dependency of Volume (μm^3) of detected PSF, PDG and CORE at different light intensity.

	1000mA	**1500mA**	**2000mA**
PSF	1071.518	1364.693	1469.961
PDG	20.4241	22.6521	27.1305
CORE at cont. 60	1.920807	1.045922	0.956652
CORE at darkest cont.	0.189329	0.007504	0.00297
	2500mA	**3000mA**	**3500mA**
PSF	1817.626	2106.781	1909.721
PDG	25.0918	24.8955	32.7061
CORE at cont. 60	0.280789	0.052687	0.003909
CORE at darkest cont.	0.002345	0.052687	0.003909

definition of focus.

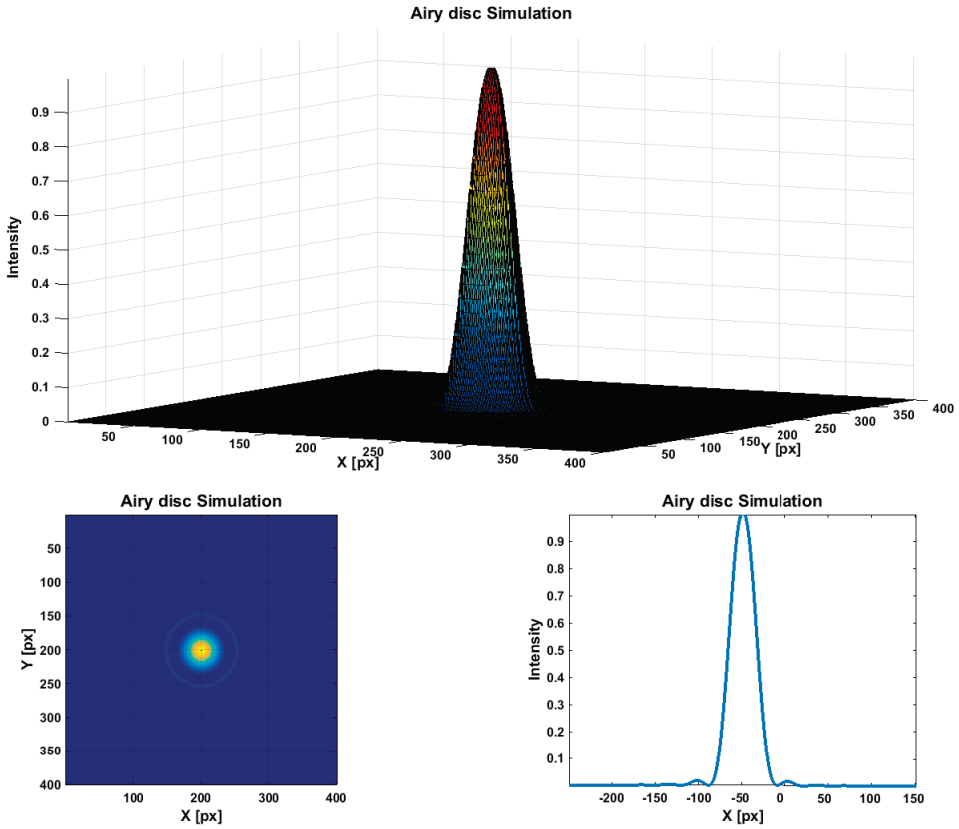

Figure 5.11: Airy disc simulation - top image - 3D view, left bottom image - top view, right bottom image - intensity profile

ENZ

PSF was simulated according to knowledge presented in section 2.2.2. All simulation used codes from http://www.nijboerzernike.nl/. Codes were changed to produced complete 3D simulation instead of sections.
PSF without any aberration can be simulated using Zernike polynomial Z_0^0, where $m = 0$ and $n = 0$. This settings will simulate the ideal situation where no aberration is present (Fig. 5.12).

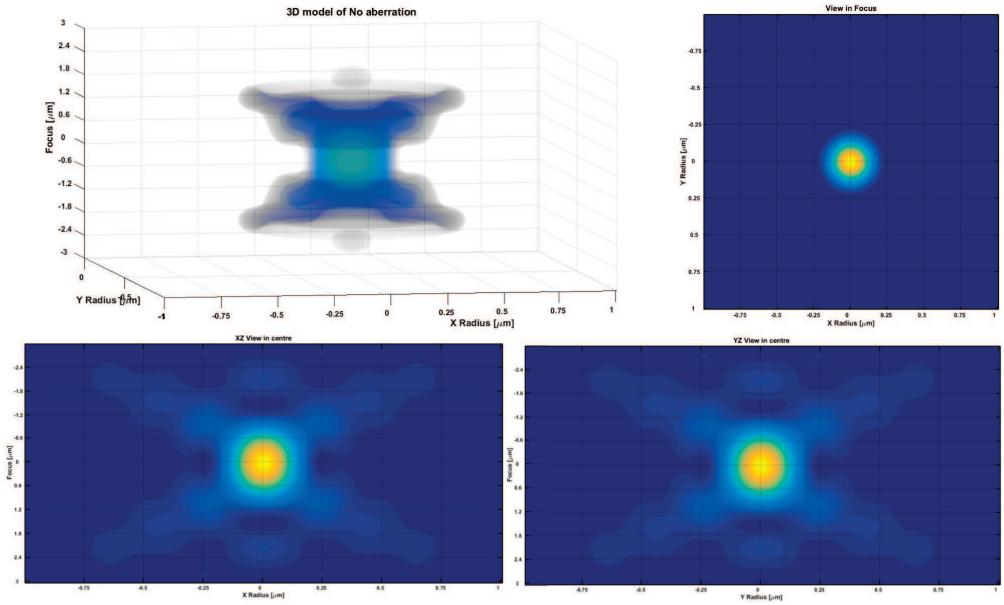

Figure 5.12: ENZ simulation of PSF without any Aberration. Upper left image shows 3D reconstruction of PSF without any aberration, upper right shows image in focus position, bottom row shows side view. Left image XZ section and right image YZ section in the centre of the particle.

Using this basic example the dependency of the size and the shape of PSF on the size of the particle (Fig. 5.13) and on the wavelength (Fig. 5.14,5.15) can be shown.

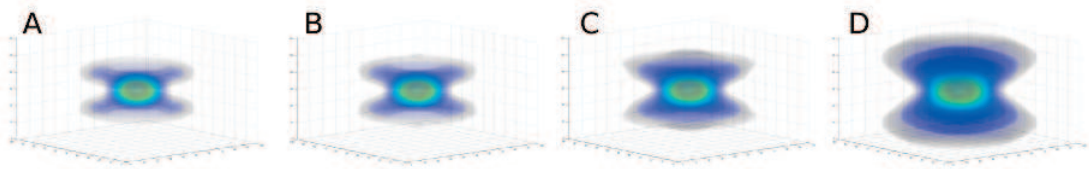

Figure 5.13: This set of images describes changes of PSF with changing of the particle's size. Parameters of simulation were $\lambda = 200nm$, NA (numerical aperture) was 0.5, and without any aberration ($m = 0, n = 0$). A - $d = 200nm$; B - $d = 300nm$; C - $d = 400nm$; D - $d = 500nm$

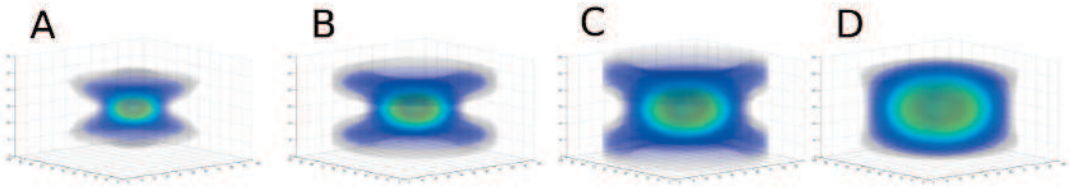

Figure 5.14: This set of images describes changes of PSF with changing of the light wavelength. Parameters of simulation were diameter was 400nm, NA (numerical aperture) was 0.5, and without any aberration ($m = 0, n = 0$). A - $\lambda = 200nm$; B - $\lambda = 300nm$; C - $\lambda = 400nm$; D - $\lambda = 500nm$

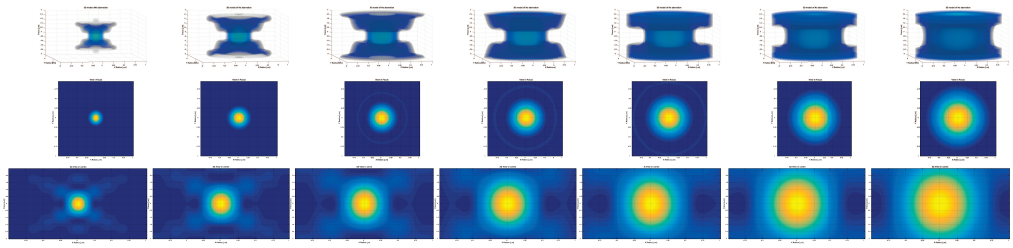

Figure 5.15: ENZ simulation – Wavelength dependency. Top row shows 3D model of ENZ simulation, middle row shows view in focus, bottom row shows side view. Each column shows different wavelength. From left to right – $0.2\mu m$; $0.3\mu m$; $0.4\mu m$; $0.5\mu m$; $0.6\mu m$; $0.7\mu m$; $0.8\mu m$.

Other parameters which can help us with simulation of specific microscope and experiment are numerical aperture of objective, diameter of light source (in our case diameter of our particle, Fig. 5.13), wavelength of used light (Fig. 5.14), and rotation of aberration. Equations 2.19 and 2.21 tell us that PSF is periodical function and also if there are some aberrations PSF can be non-symmetrical.

According to eq. 2.21 it is possible to simulate different types of aberrations.

Simulation of **Tilt** aberration using eq. 2.23,2.24 shows the symmetry along the central XY plane (Fig. 5.16).

Defocus aberration describes by eq. 2.25 shows shift of the image of the object along Z axis (Fig. 5.17) The PSF in this case is symmetrical along

central XZ and YZ plane.
Also **Astigmatism** shows the symmetry along same planes (Fig. 5.18), but here it depends on parameter θ in eq. 2.26, 2.27.
Coma aberration (Fig. 5.19) shows symmetry along central XY and XZ planes, but again is the symmetry θ dependent (eq. 2.28, 2.29).
Spherical aberration (Fig. 5.2) shows symmetry along central XZ and YZ planes.

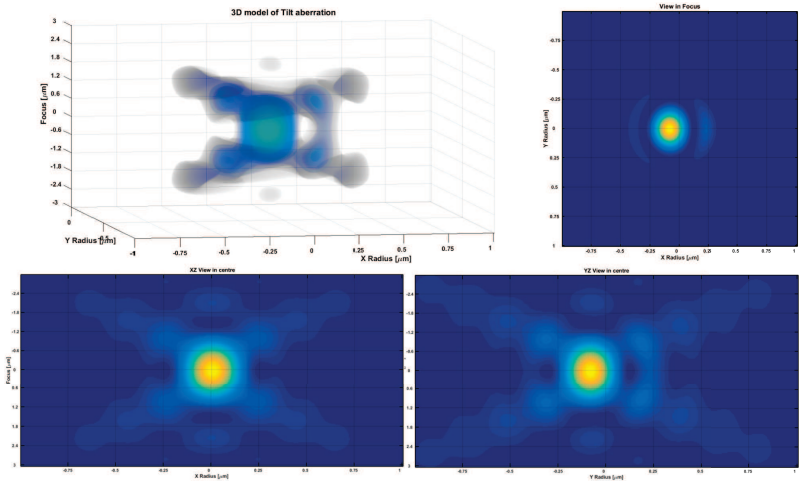

Figure 5.16: ENZ simulation of Tilt Aberration. Upper left image shows 3D reconstruction of Tilt aberration, upper right shows image in focus position, bottom row shows side view. Left image XZ section and right image YZ section in the centre of the particle.
Parameters of the simulation: $na = 0.5$, $d = 0.2\mu m$, $\lambda = 0.2\mu m$, Z *(power of aberration)* $= 0.3$, $m = 1$, $n = 1$.

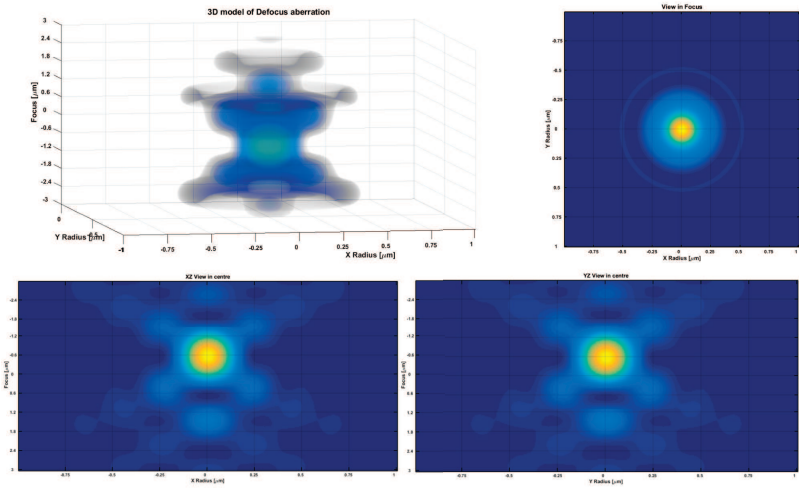

Figure 5.17: ENZ simulation of Defocus Aberration. Upper left image shows 3D reconstruction of Defocus aberration, upper right shows image in focus position, bottom row shows side view. Left image XZ section and right image YZ section in the centre of the particle.
Parameters of the simulation: $na = 0.5$, $d = 0.2\mu m$, $\lambda = 0.2\mu m$, Z *(power of aberration)* $= 0.3$, $m = 0$, $n = 2$.

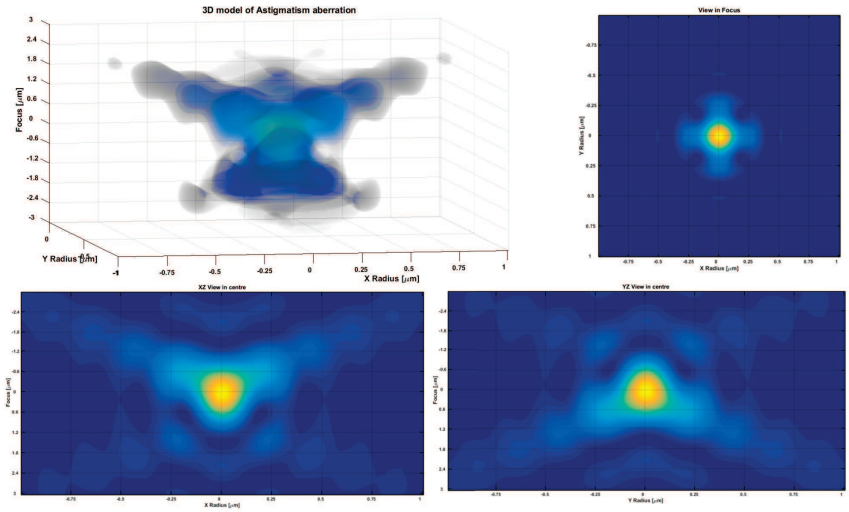

Figure 5.18: ENZ simulation of Astigmatism. Upper left image shows 3D reconstruction of Astigmatism aberration, upper right shows image in focus position, bottom row shows side view. Left image XZ section and right image YZ section in the centre of the particle.
Parameters of the simulation: $na = 0.5$, $d = 0.2\mu m$, $\lambda = 0.2\mu m$, Z *(power of aberration)* $= 0.3$, $m = -2$, $n = 2$.

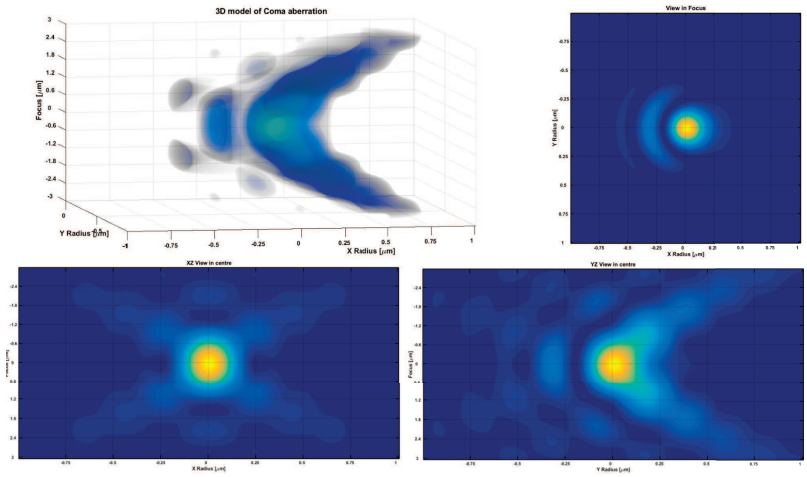

Figure 5.19: ENZ simulation of Coma Aberration. Upper left image shows 3D reconstruction of Coma aberration, upper right shows image in focus position, bottom row shows side view. Left image XZ section and right image YZ section in the centre of the particle.
Parameters of the simulation: $na = 0.5$, $d = 0.2\mu m$, $\lambda = 0.2\mu m$, Z *(power of aberration)* $= 0.3$, $m = -1$, $n = 3$.

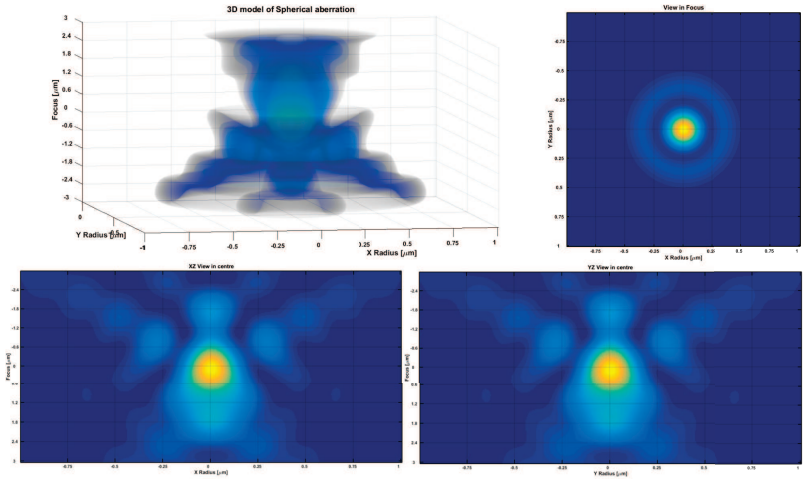

Figure 5.20: ENZ simulation of Spherical aberration. Upper left image shows 3D reconstruction of Coma aberration, upper right shows image in focus position, bottom row shows side view. Left image XZ section and right image YZ section in the centre of the particle.
Parameters of the simulation: $na = 0.5$, $d = 0.2\mu m$, $\lambda = 0.2\mu m$, *Z (power of aberration)* $= 0.3$, $m = 0$, $n = 4$.

5.3 Resolution, Discriminability, Distinguishability

In order to understand origin of physical limits of discriminability and distiguishability as defined in the section 2.1.3 we may use available models. The most appropriate for this purpose seems to be the ENZ theory (Fig. 5.21) and Airy disc simulation. The Airy disc simulation may, in fact, be understood as a section of ENZ model in the focal plane (Fig. 5.22, 5.23). At Fig. 5.24 and Fig. 5.25 is shown the experimental reality.

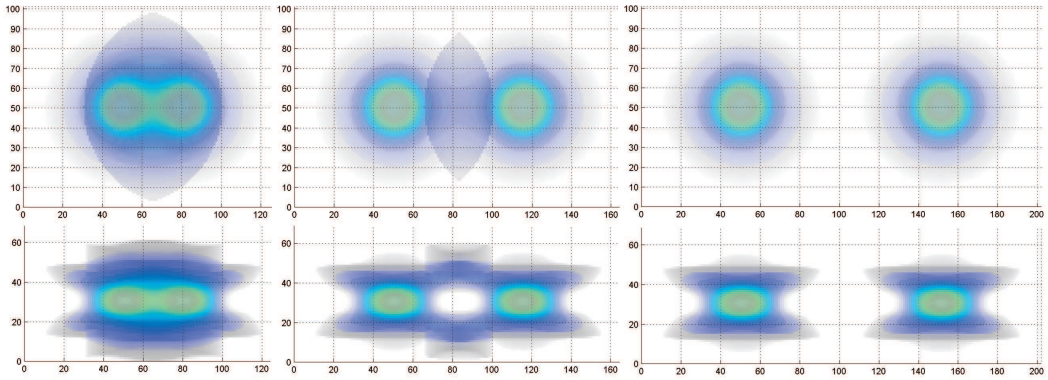

Figure 5.21: First and second column show discriminable particles. Third column show particles in distance of resolution. Upper row shows top view, bottom row shows side view.
Parameters of the simulation: $na = 0.5$, $d = 0.2\mu m$, $\lambda = 0.2\mu m$, $m = 0$, $n = 0$.

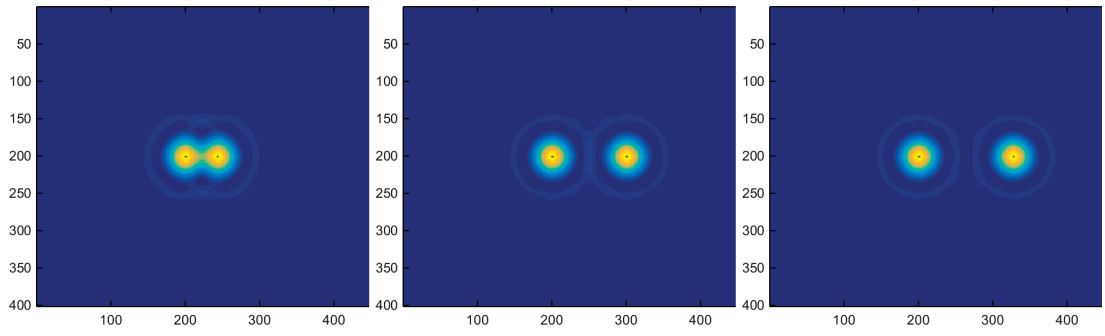

Figure 5.22: Left image shows particles not discriminable, there is no valley between maxima. Particles on the middle image are discriminable. Particles on the right are in the distance of resolution.
Parameters of the simulation: $na = 0.5$, $d = 0.2\mu m$, $\lambda = 0.2\mu m$, $m = 0$, $n = 0$.

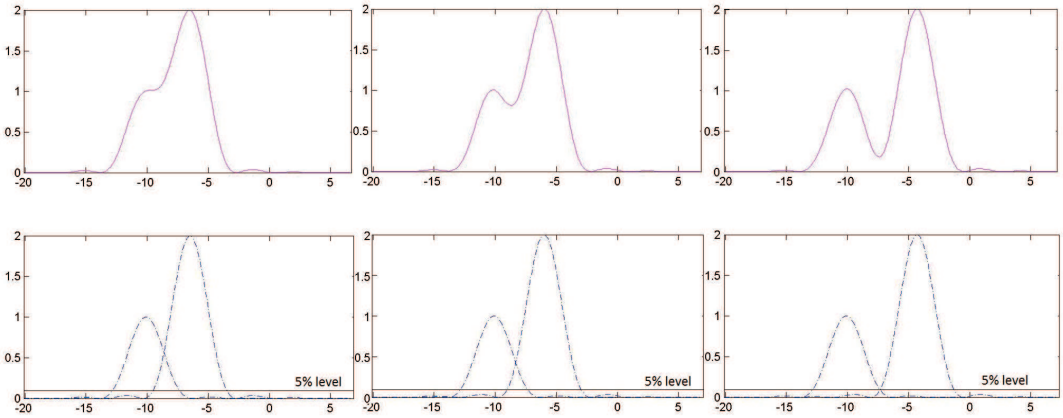

Figure 5.23: First column shows particles (peaks) not discriminable, there is no valley between maxima. Particles (peaks) in the second column are discriminable. Particles (peaks) in the third column are in the distance of resolution. Upper row shows cumulative peaks, bottom row shows individual peaks.

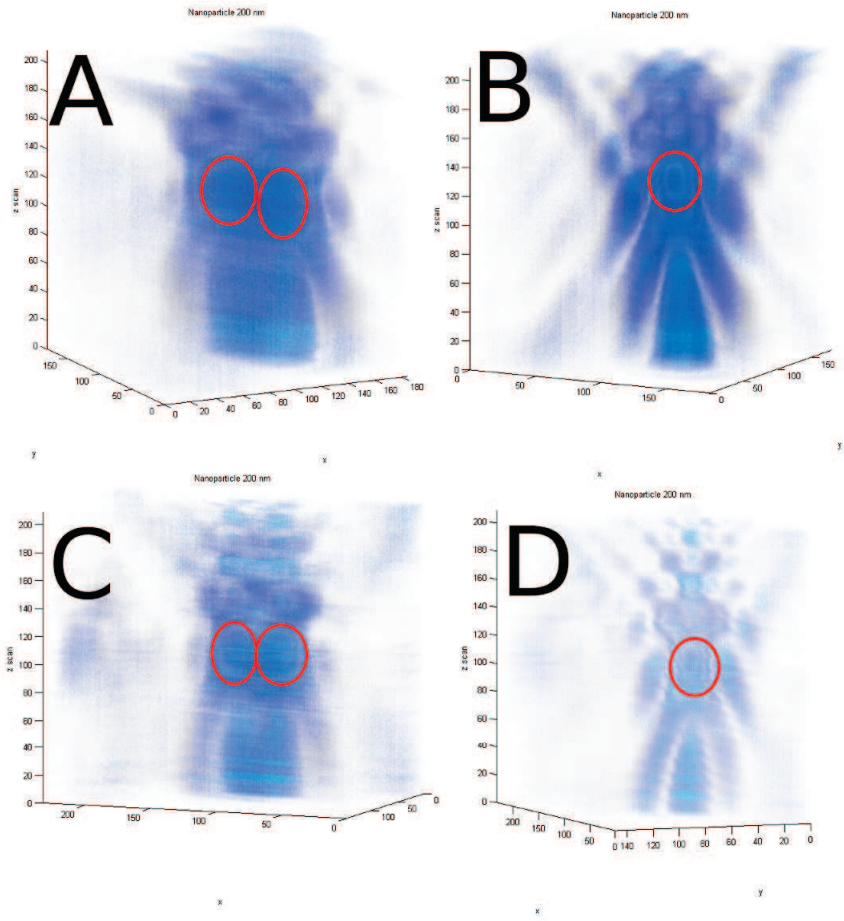

Figure 5.24: This image shows situation were 2 220nm latex particles are closer than resolution. A and C shows different particles from the side view, B and D shows same particles as A and C but from different side. Red circle show position of real particle. X and Y axis are in pixels, Z axis show number of layers, distance between layers is 100nm.

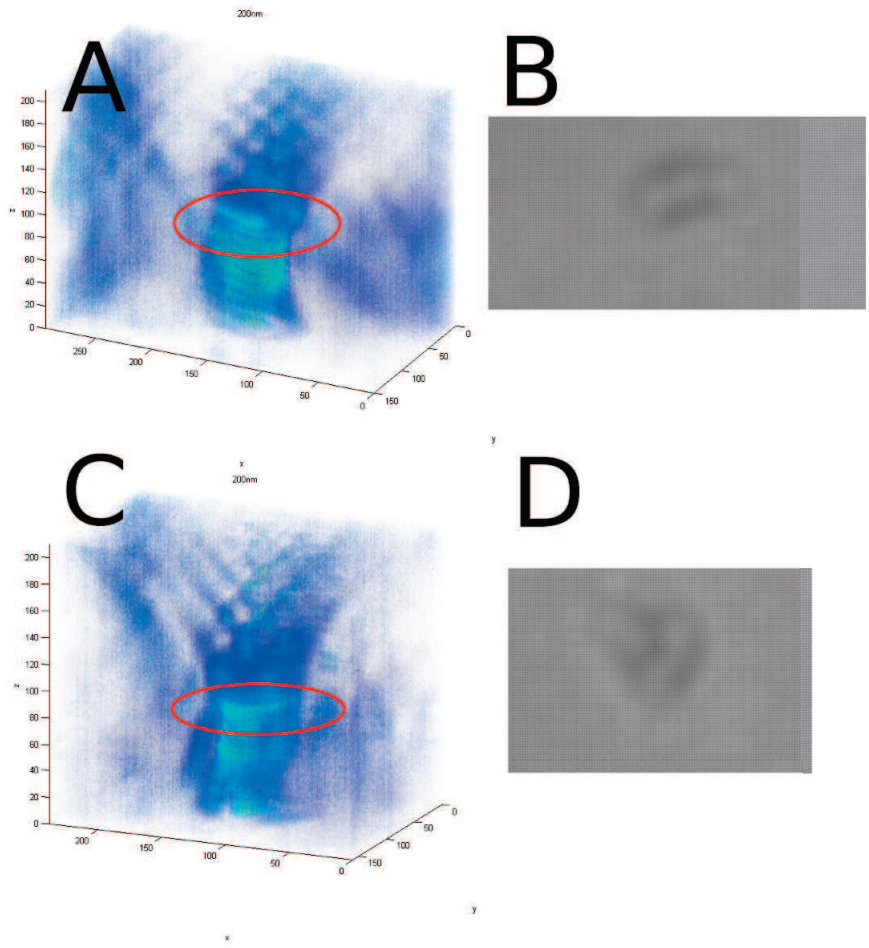

Figure 5.25: Part A shows 3D reconstruction of situation when 3 $220nm$ latex particles are in one row. Part B is the top view on situation A. Part C show 3D reconstruction of 4 particles in one cluster, on part D you can see how the same situation looks in microscope. Red circle show position of real particle. X and Y axis are in pixels, Z axis show number of layers, distance between layers is $100nm$.

5.4 Experiments

5.4.1 Bright field microscopy

Due to conflicts between the physical interpretation and known experiments described above we have decided to analyse a few basic experiments.

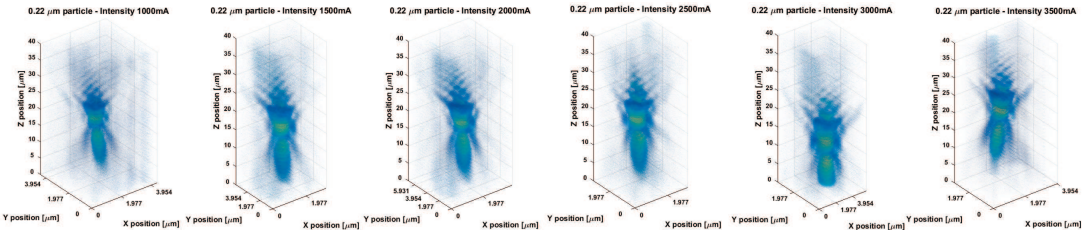

Figure 5.26: Real PSF under different light condition. Intensity is increasing from the left ($1000mA$) to the right ($3500mA$) with the step of $500mA$.

We, indeed, found out that there is dependency of the size and shape of PSF on size of the particle and on light intensity (Fig. 5.26). The reality is indeed much more complex than the simplified predictions of the influence of light intensity, where Mizushima [12] predicts ***sole*** increase of the signal - to noise ratio and Lipson [14] predicts - in real terms - increase of the slimness of the PSF. We see overall change of the shape of the PSF.

Part of the problem may originate from non-ideality of the latex particle, more likely, however, the problem comes from its scattering as described by the Mie simulation 2.3. The particle scatters light into distorted wavefront which is consequently translated by the lens into the image. The interference pattern thus becomes practically non-intelligible. Upon increase of the light intensity on the PSF certainly changes. We observe a complicated change of the point spread function. As for the size of the darkest object in the image interior we observe a minimum at the 3000 mA diode current fig. 5.27.

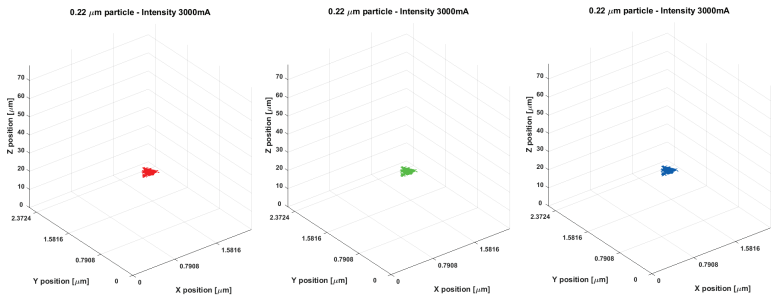

Figure 5.27: Core of PSF at $3000mA$ in three different channels (from left to right - red, green, blue)

The simple prediction of signal to noise origin of the increase of discriminability of objects in the brightfield microscope was not confirmed. The proposition that the point spread function becomes slimmer with increasing light intensity is realistic to a certain limit. It needs to be considered that it was developed for the microscopy of light emitting point sources and it relies on a very simplified interpretation of quantum mechanics. The ENZ theory, not talking about any simplified versions of the resolution, are not applicable on this simplest possible experiment. On the other hand, it was confirmed that upon appropriate choice of light conditions we may observe signal from an object which is localised in one camera pixel, in fact the *discriminable* signal is smaller than the size of the object itself.

According to simulation we should also analysed the dependency on the wavelength. We used different color channels on camera for partial discrimination between wavelengths. But still each color channel contains set of different wavelengths. The dependency of measured PSF and detected core can be seen on Fig. 5.28. This figure (5.28) shows intensity and wavelength dependency. The effect which is examined here is the analogy of the term chromatic aberration of the microscope. Indeed this aberration is changing with the light intensity differently for each group of wavelengths.

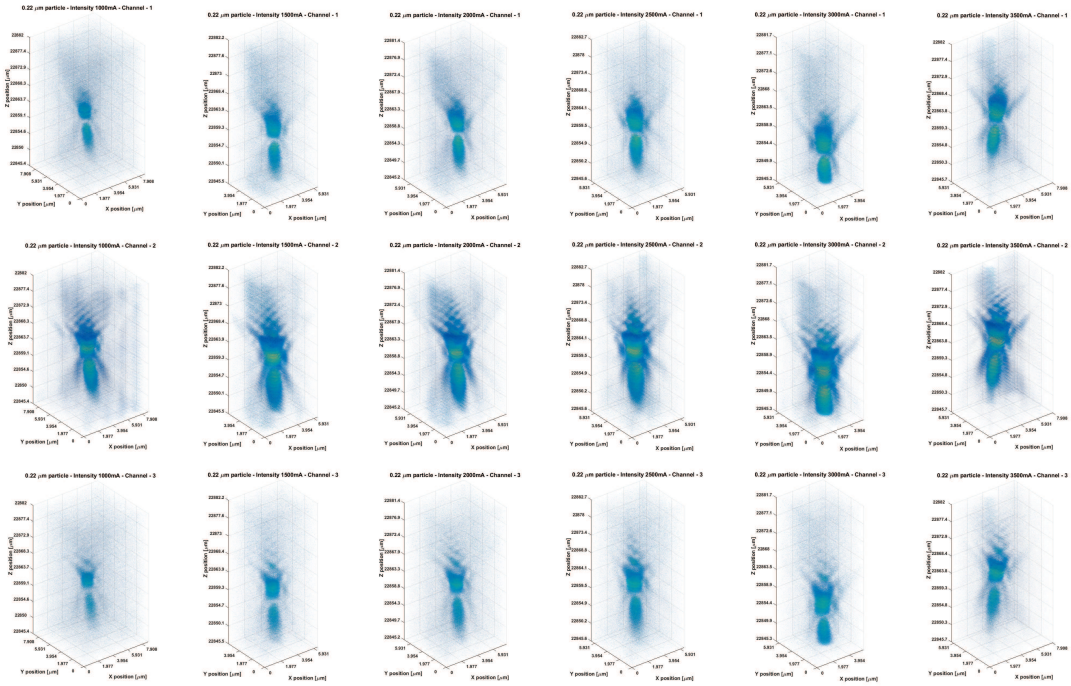

Figure 5.28: Wavelength dependency of real PSF under different light condition. Intensity is increasing from the left ($1000mA$) to the right ($3500mA$) with the step of $500mA$. First row shows red channel, second row shows green channel, third row shows blue channel.

5.4.2 Fluorescent microscopy - CLSM

The fluorescent microscopes' software usually has some automatic procedures to suppress the PSF and to eliminate the errors (such as elongation in the Z axis direction). Such software represents certain minimal approximation to the PSF too.

Method used for improving images obtained by the bright field microscopy gives us better results than the CLSM techniques. The CLSM experiments were done using the same particles as for the bright field images. The only difference was in the preparation of the sample, for the CLSM experiments was necessary to stabilize the particles by using the agarose. This means that the results are fully comparable. Complete experimental setup can be seen in Appendix A.

The smallest particle is almost not visible even in fluorescence microscope (Fig. 5.29).

On the figures 5.29, 5.30, 5.31 and 5.32 can be seen how the size of the particle affects the size and the shape of PSF.

The size of PSF is not affected only by the size of the particle but also by the wavelength of the light as can be seen on ENZ models (fig.5.15).

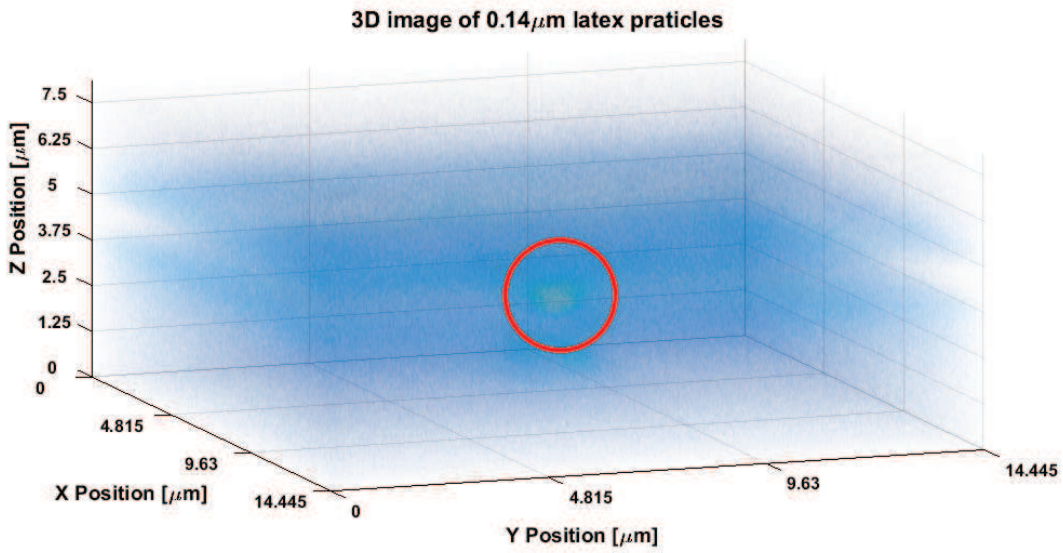

Figure 5.29: CLSM 3D image of $0.14\mu m$ particles. Red circle marks the position of the particle.

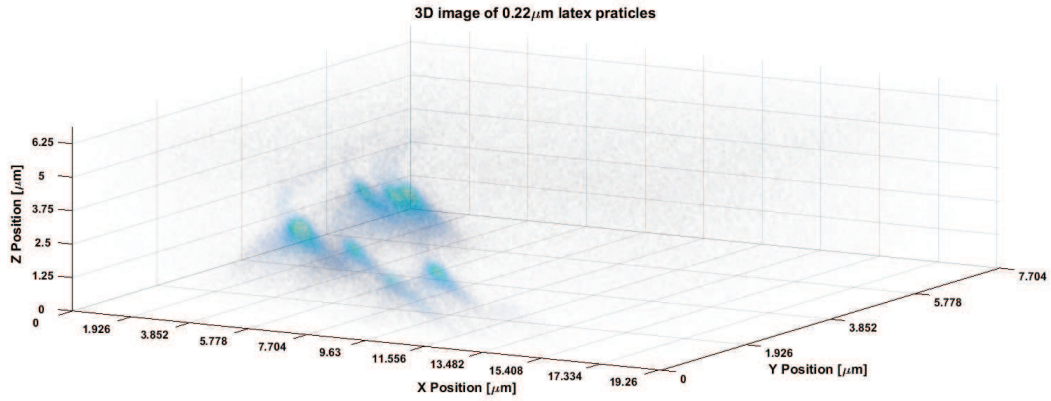

Figure 5.30: CLSM 3D image of $0.22\mu m$ particles.

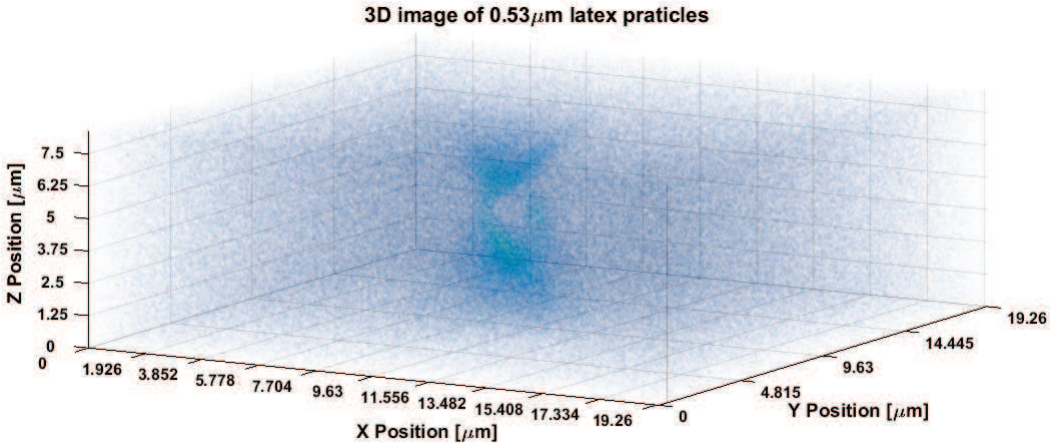

Figure 5.31: CLSM 3D image of $0.53\mu m$ particles.

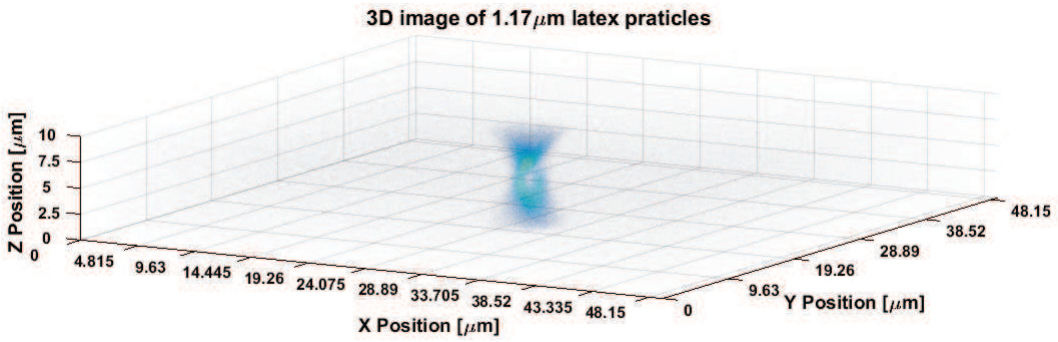

Figure 5.32: CLSM 3D image of $1.17\mu m$ particles.

5.5 Focus - new definitions

From the results presented above it follows that focusing in real experiment significantly differs from the theory. In diffracting samples, the PSF exhibits multiple maxima and minima of the area of projection into the XY plane. But also the fluorescence emission microscopy needs to be considered carefully to obtain the true "focal to be" plane. Thus if we want to observe image at one plane instead of focusing through the object, we have to redefine the notion of focusing. This is particularly important since many systems contain automatic focusing software which can focus on different position in fluorescence and in BF mode. On the contrary, proper focusing algorithm my help the acquisition of images, namely in case of sensitive samples, significantly.

In our new definition the goal of finding the best focus is to see maximum of details on the image. This requires a new definition of optimal focal plane. Different types of focus can be defined (Fig. 5.33, 5.34). In this case results of experiments with $0.5\mu m$ particle were used because of using phase contrast. On fig. 5.34 experiments with $220nm$ particles are shown.

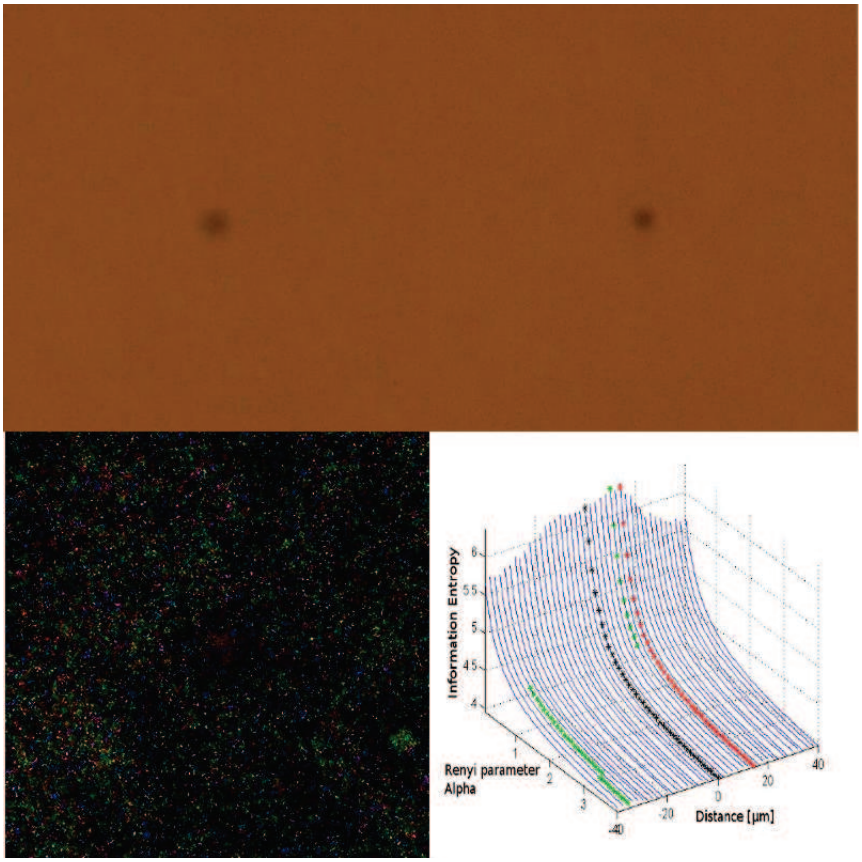

Figure 5.33: Different focal planes - A - focus by human eye ("expert" focus) - position $0\mu m$, B - Airy focus - $+18\mu m$, C - Information focus (entropy image) - $\alpha = 0.1 - 0.9$ - position $+14\mu m; \alpha 1.0 - 3.1$ - position $-34\mu m; \alpha = 3.2 - 4.0$ - position $-36\mu m$; , D - 3D graph of distance of different focuses

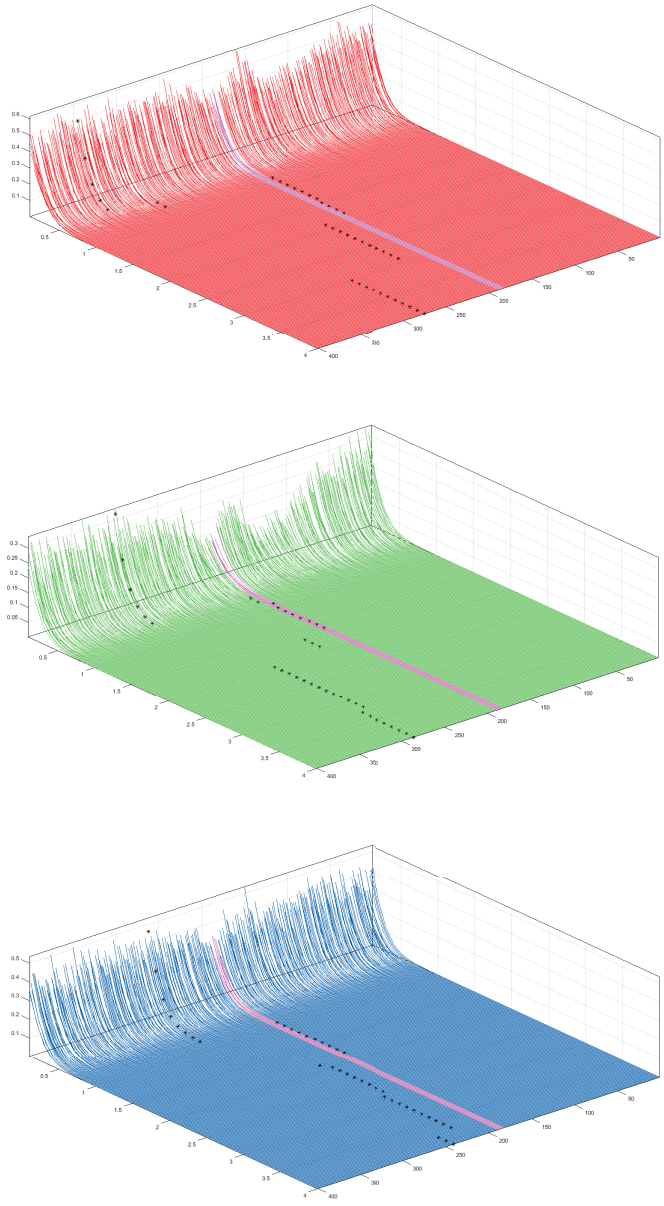

Figure 5.34: Entropy Focus at light intensity $2000mA$ in different color channels (red, green, blue). Violet lines show position of particles detected by algorithm for finding the core of PSF. Black stars are position of entropy (information) focus. In graphs the X axis are values of parameter α, Y axis show position in z-scan, and Z axis show value PIE.

One of the focal planes can be called Airy focus. The position of this focus corresponds to the definition by the optics. We call it Airy focus because the imaging of the point looks same as the simulation of Airy disc. Airy focus is objectively defined focus *for one separate object*. This position can be obtained by matching the intensity profile of the latex particle with simulation of Airy disc as mentioned in part 2.1. This focal plane corresponds to the position where we are observing real particle. Indeed for diffracting objects we may obtain several apparent Airy focus planes.

Second focus, called as Expert focus, is the position where the maximum details can be seen by human eyes. It is called Expert focus because the position is find by the operator of the microscope. Problem is that every man or woman can consider this focal plane in different z-position. This means that this position is subjective but good for manual analysis.

Third focus called as Entropy (or Information) focus can be defined as the position where we can obtain maximum information from the image. The Entropy focus was obtained by using the point information gain (PIG) approach and defines the position of lowest point information gain entropy [80, 82, 81]. This focus is objective and good for automatic analysis.

Depending on what should be analyse different value of parameter α in eq. 2.34 and eq. 5.1 should be selected. Value of the α parameter determines parts of image which will be enhanced. α lower than 1 enhance rare points, α higher than 1 enhance common points (large areas of the same colour). We used different α parameters from 0.1 to 4.0 with step 0.1. We find maximum for each α. This maximal value of PIE_α is maximum information we can obtained from the image. Therefore we call this position Information focus. Airy focus was in our case 18 micrometers from "expert" focus. This difference between Airy and "expert" focus is given by the size and shape of PSF, so this distance will be different for each experiment. Summary of the focusing experiments is shown in the Tab. 5.5.

The information focus differs from both of previously defined focuses due to the principle of calculation of information content of the image. However we can consider the information focus as equally objectively achieved focal plane as Airy focus. Advantage of this method is indepen-

Table 5.5: Size of the object in different focal plane. Real size of the object is $0.5\mu m$. Size of the pixel is approx. $0.1\mu m$.

Focus	**Size in px**	**Approx. size in μm**
A - "Expert" focus	12 px	1.2 μm
B - Airy focus	8 px	0.8 μm
C - Information focus	6 px	0.6 μm

dence on the observed object. This means that this method can be used for all samples and not only for nanoparticles. Entropy focus is α dependent, this means it depends on which part of the image we are focusing.

There are also other terms related to the focus; Focal length, depth of field and depth of focus. Focal length characterize the strength of optical system. It describes how strongly the optical system focus light. System with shorter focal length has more optical power.

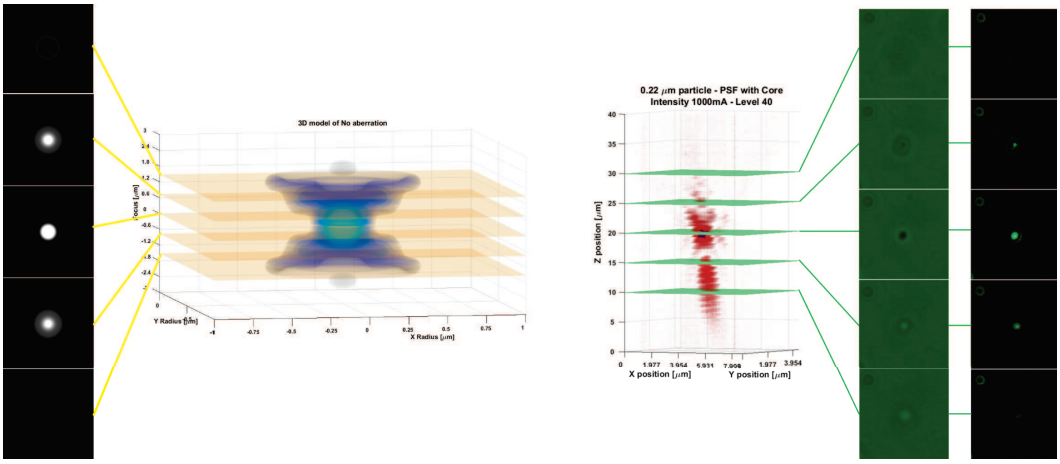

Figure 5.35: This image shows comparison of ENZ simulation and real PSF. The left part shows ENZ simulation and with appropriate section. Parameters of the simulation are $na = 0.5$, $d = 0.2\mu m$, $\lambda = 0.2\mu m$, $m = 0$, $n = 0$. The central section shows focus position. Right part shows measured PSF with appropriate section. First column shows real RGB images and the second column shows entropy transformed images. The central section shows focus position.

On the figure 5.35 is shown how the focusing works. If we consider only the focus defined by ray optics (red lines) we can say that on this position is the diameter of the PSF minimal. This means that image of really small object is only point or circle. If we will use the knowledge of the PSF we can use for the focusing some higher position (positions 184, 150 on the figure 5.35). On this position will be the shape of the object more visible. This effect is caused by behaviour of Airy rings. Maxima of Airy disc in the focus defined by the ray optics are close to the image of the particle, in higher (or lower) positions the maxima of Airy discs are farther from the image of the object.

5.6 Example of complete analysis

As a proof of presented method I show complete analysis of images of $0.22\mu m$ latex particle. On the following images (Fig. 5.36, 5.37, 5.38, 5.39,

5.40, 5.41) are presented results of this analysis. Each of this images shows complete description of imaging of one particle at certain light intensity. Set of these images presents dependency of results of observation of the small particle on the light intensity. It shows that there is some optimum of the light intensity which allows us to observe really small details in the image. Each image also presents dependency of the size and shape of PSF on the wavelength of the light. In this case this is presented as analysis in separated color channels. Each color channel still contains different wavelength but differences between channels can be easily observed.

The analysis is based on Z-scan of the latex particle in the brightfield mode. Images were transformed by PIG algorithm afterwards for better visualisation of PSF 3D reconstruction. Next step is the PDG transformation and core analysis. Data for PSF visualization were thresholded to have better overview of the PSF. The problem is how to define proper threshold. In this case Otsu method [53] were used. If the PDG and thresholded PSF is compared the PDG model can looks bigger. This is caused by the principle of calculation of the PDG model. The PDG model is created on the comparison of two consecutive images. On the positions were pixels have the same value the PDG model is defined. This means that PDG model can be defined also out of the PSF.

Core of the PSF is located inside of the PDG model as the darkest points. If we will look for the darkest points in the PSF, repetition of the image of the object can be found. So it is necessary to use the PDG model for finding of the core.

This simple experiment can be used also for defining of the focus. It is easier to define proper focus due to using small a and well defined particle. The position of the particle in the 3D reconstruction can be find as the narrowest part of the PSF or the round part of the thresholded PSF or as the darkest part of the PDG model. The position of the particle is shown in violet color on the Fig. 5.34. The black stars on the Fig. 5.34 shows the position of entropy (information) focus. The position of this focus corresponds with the position of the particle when the information focus is calculated with value of α parameter from 1.0 to 1.5, in some case from 0.5

to 1.5. In the worst case information focus gives the lowest Z position of the particle.

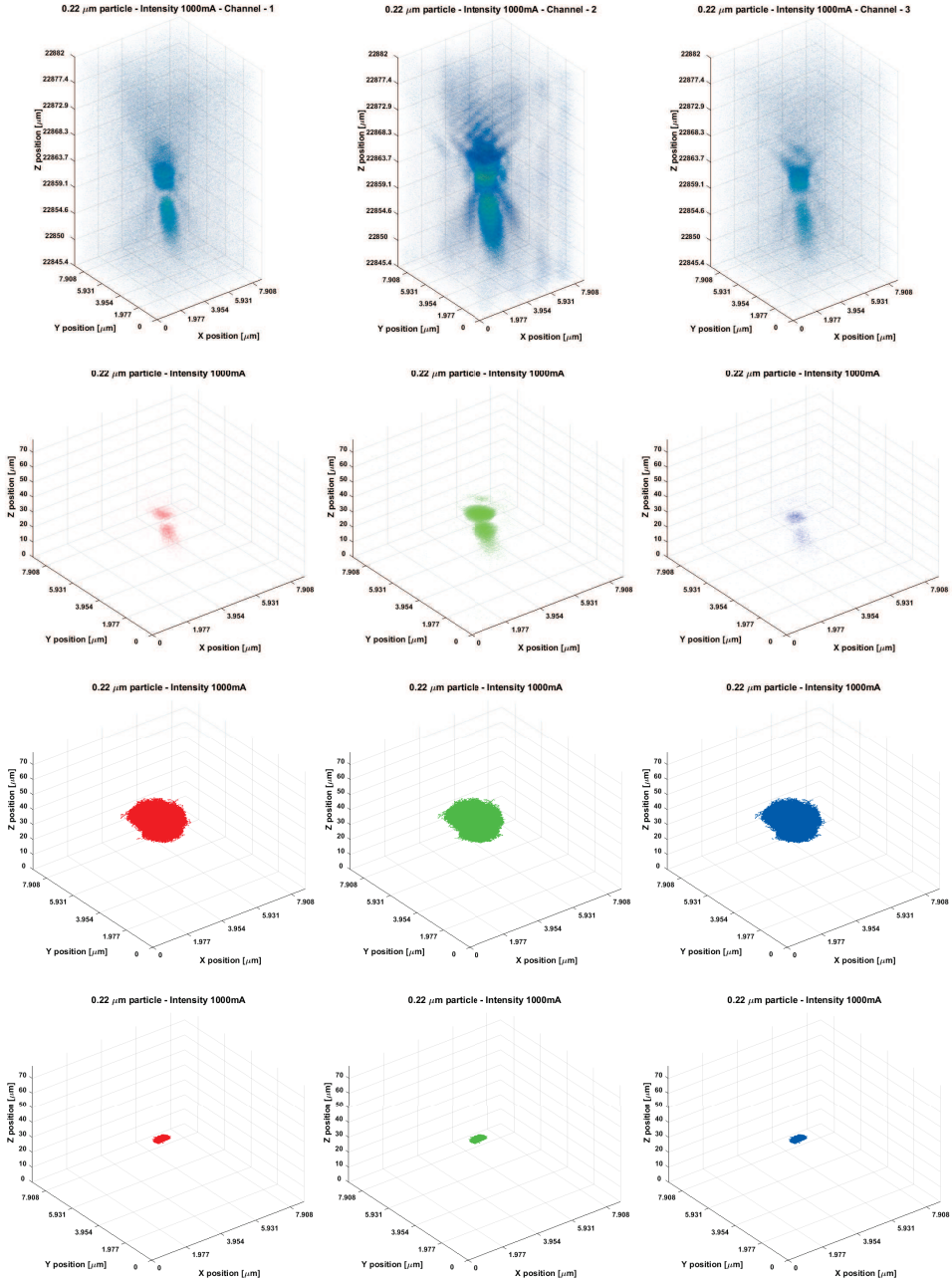

Figure 5.36: 3D reconstruction of PSF (first row), Tresholded PSF (second row), PDG (third row) and Core of PSF (bottom row) at 1000mA light intensity. Columns show different color channels (red, green, blue).

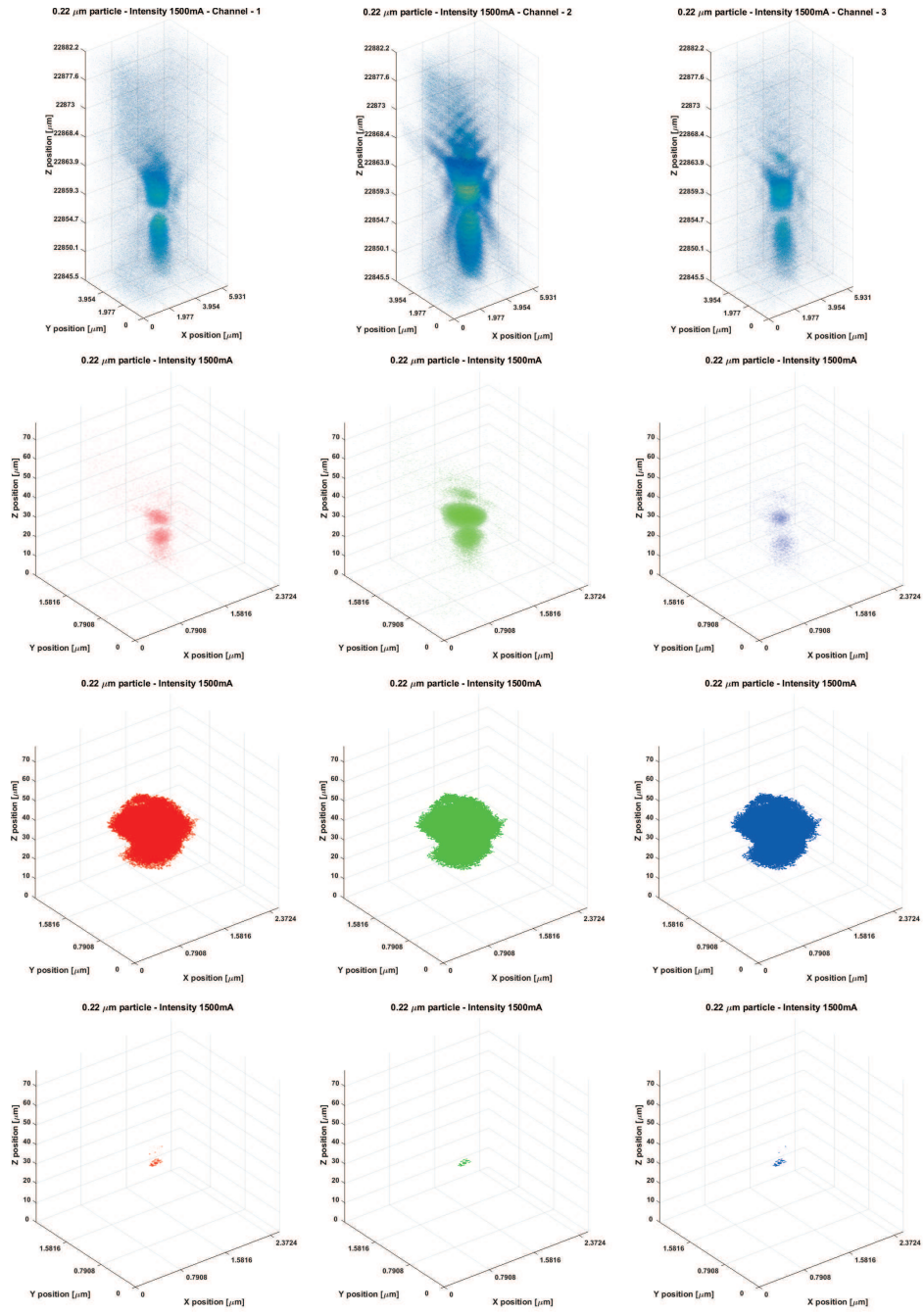

Figure 5.37: 3D reconstruction of PSF (first row), Tresholded PSF (second row), PDG (third row) and Core of PSF (bottom row) at 1500mA light intensity. Columns show different color channels (red, green, blue).

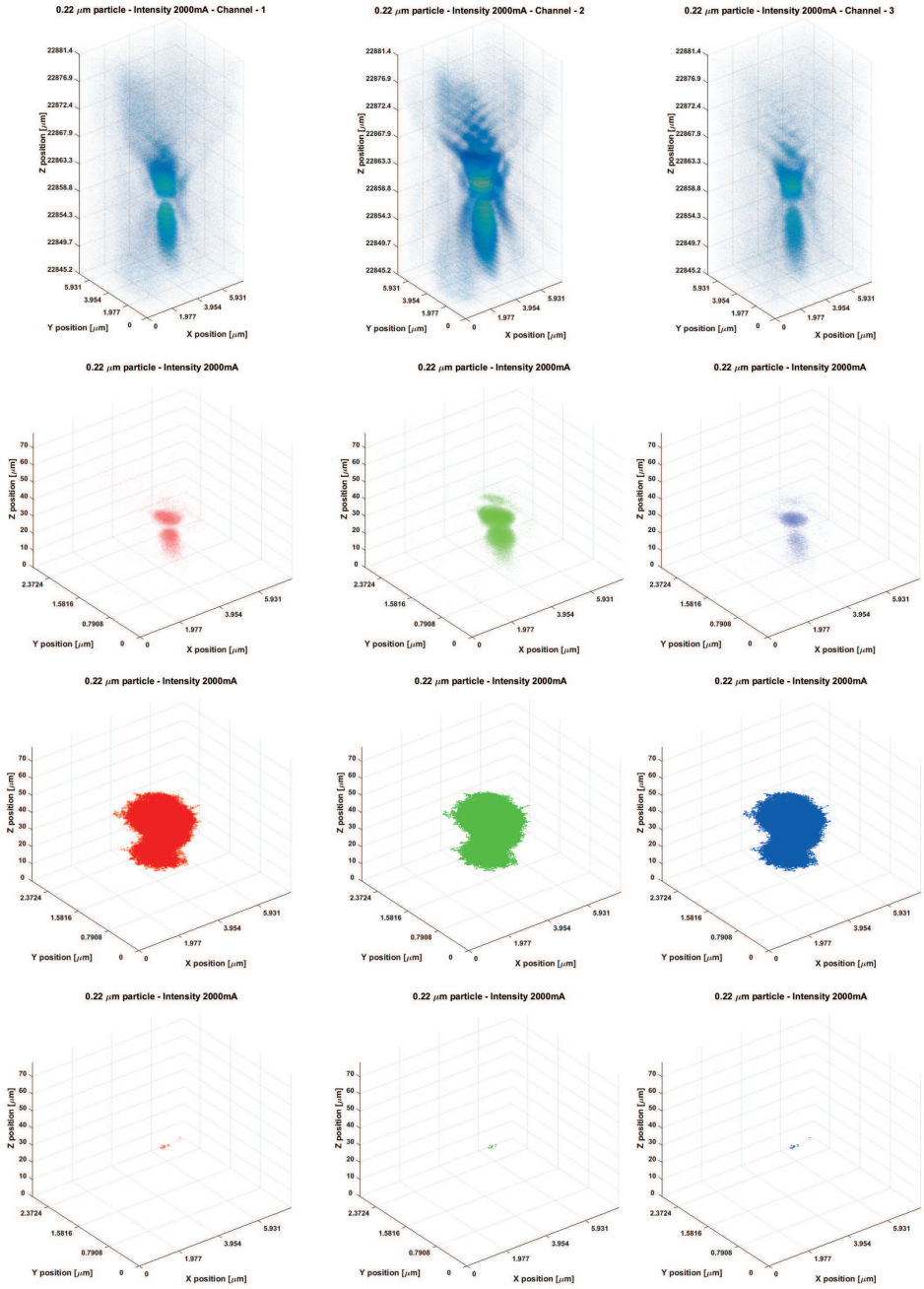

Figure 5.38: 3D reconstruction of PSF (first row), Tresholded PSF (second row), PDG (third row) and Core of PSF (bottom row) at 2000mA light intensity. Columns show different color channels (red, green, blue).

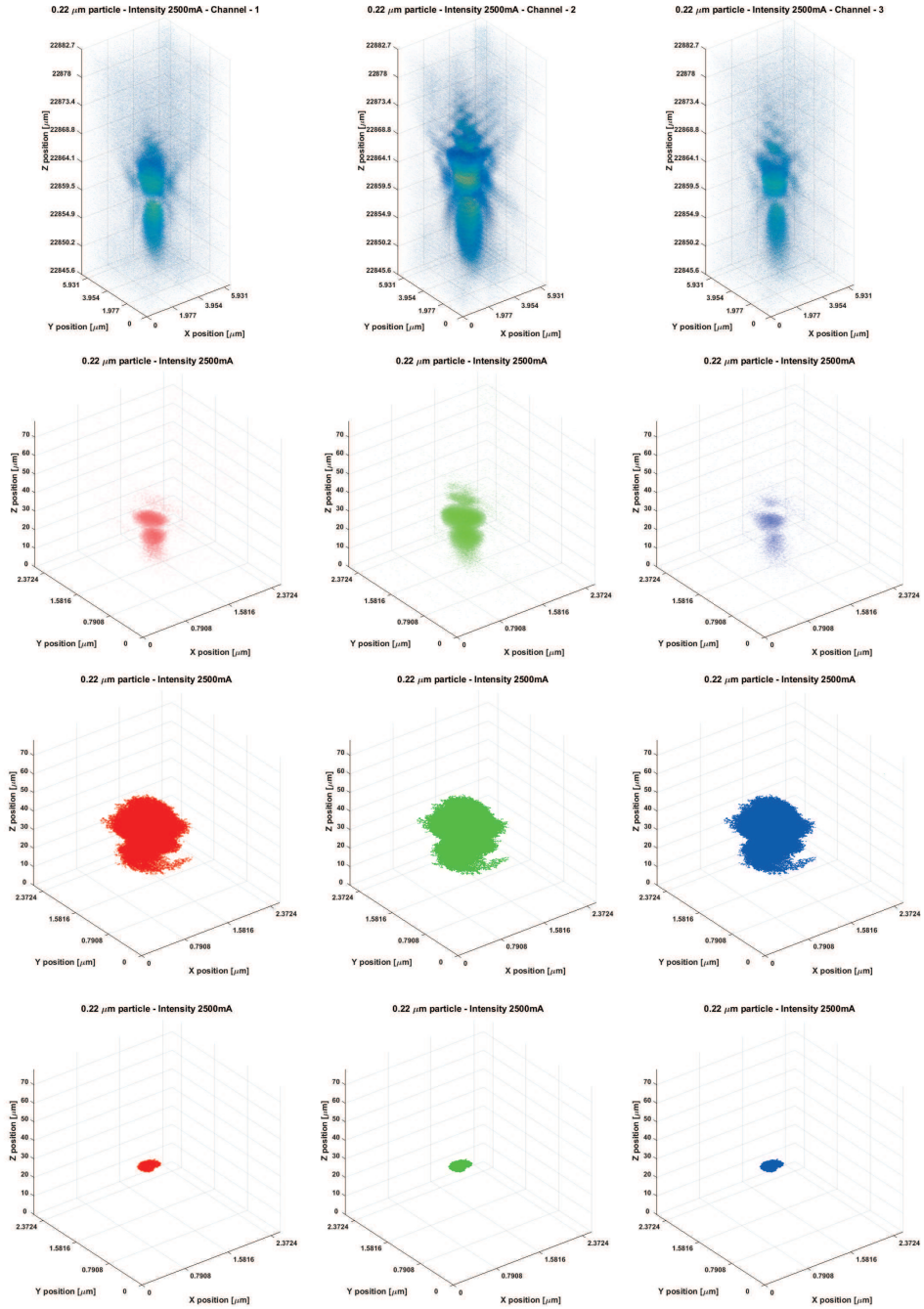

Figure 5.39: 3D reconstruction of PSF (first row), Tresholded PSF (second row), PDG (third row) and Core of PSF (bottom row) at 2500mA light intensity. Columns show different color channels (red, green, blue).

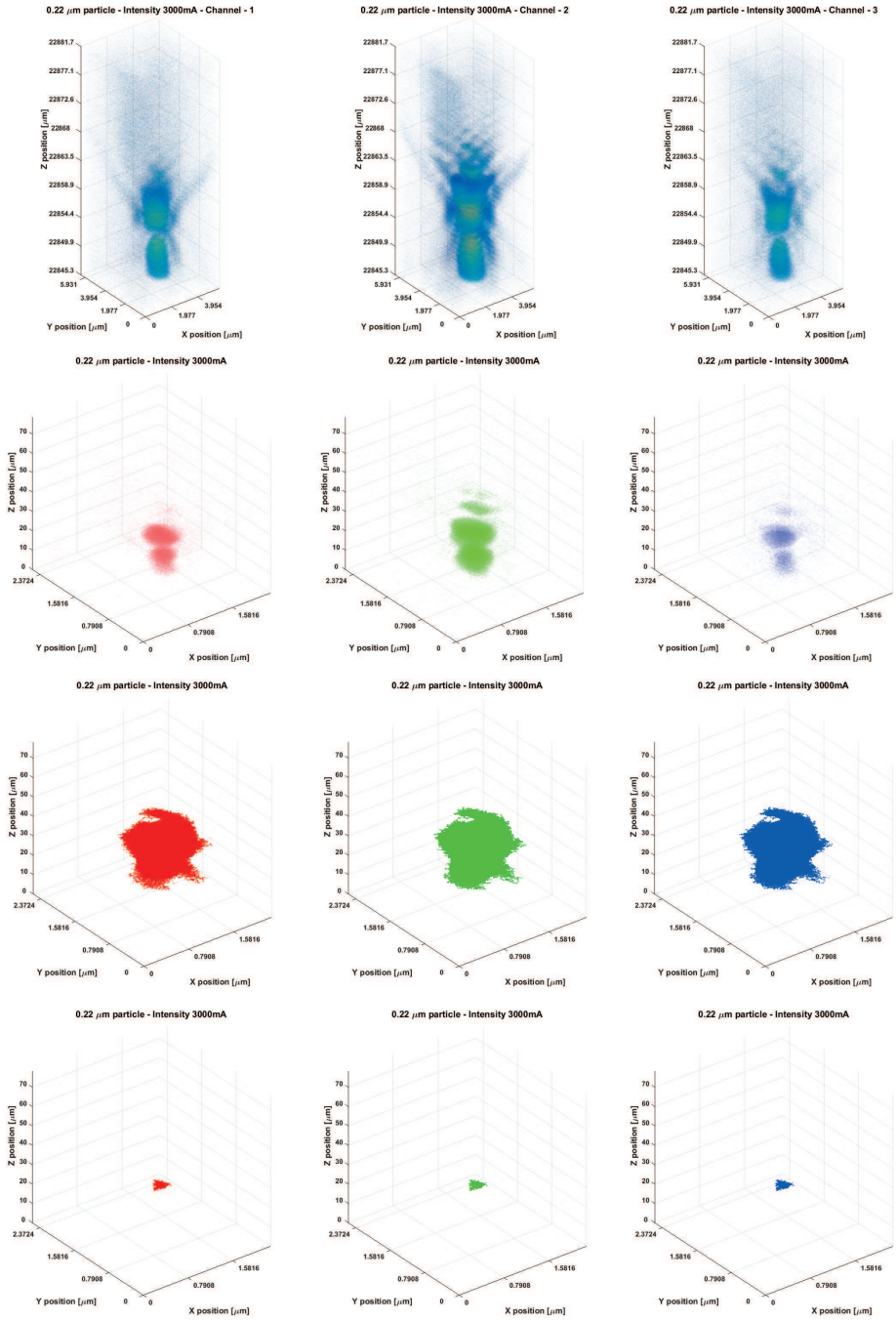

Figure 5.40: 3D reconstruction of PSF (first row), Tresholded PSF (second row), PDG (third row) and Core of PSF (bottom row) at 3000mA light intensity. Columns show different color channels (red, green, blue).

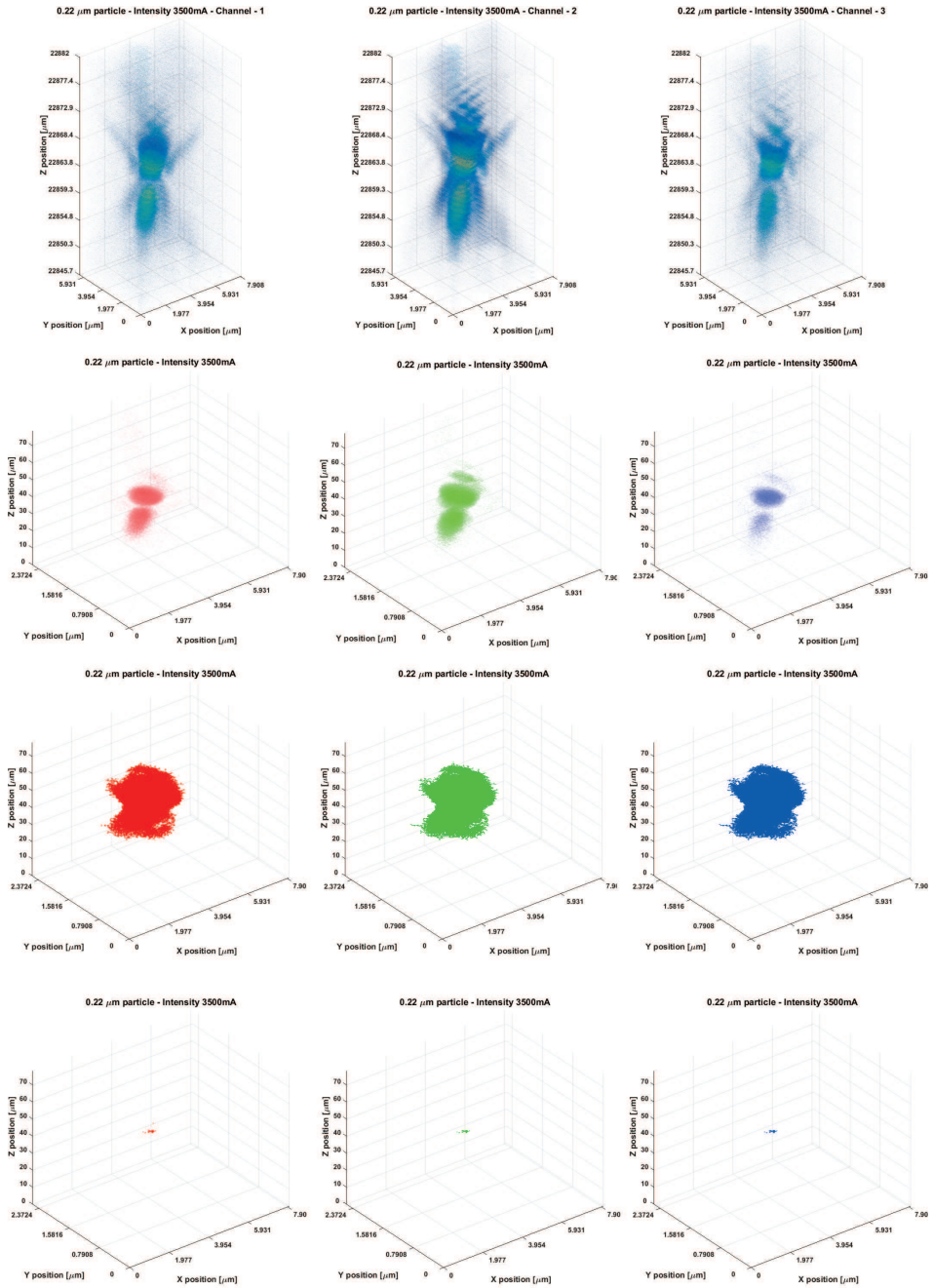

Figure 5.41: 3D reconstruction of PSF (first row), Tresholded PSF (second row), PDG (third row) and Core of PSF (bottom row) at 3500mA light intensity. Columns show different color channels (red, green, blue).

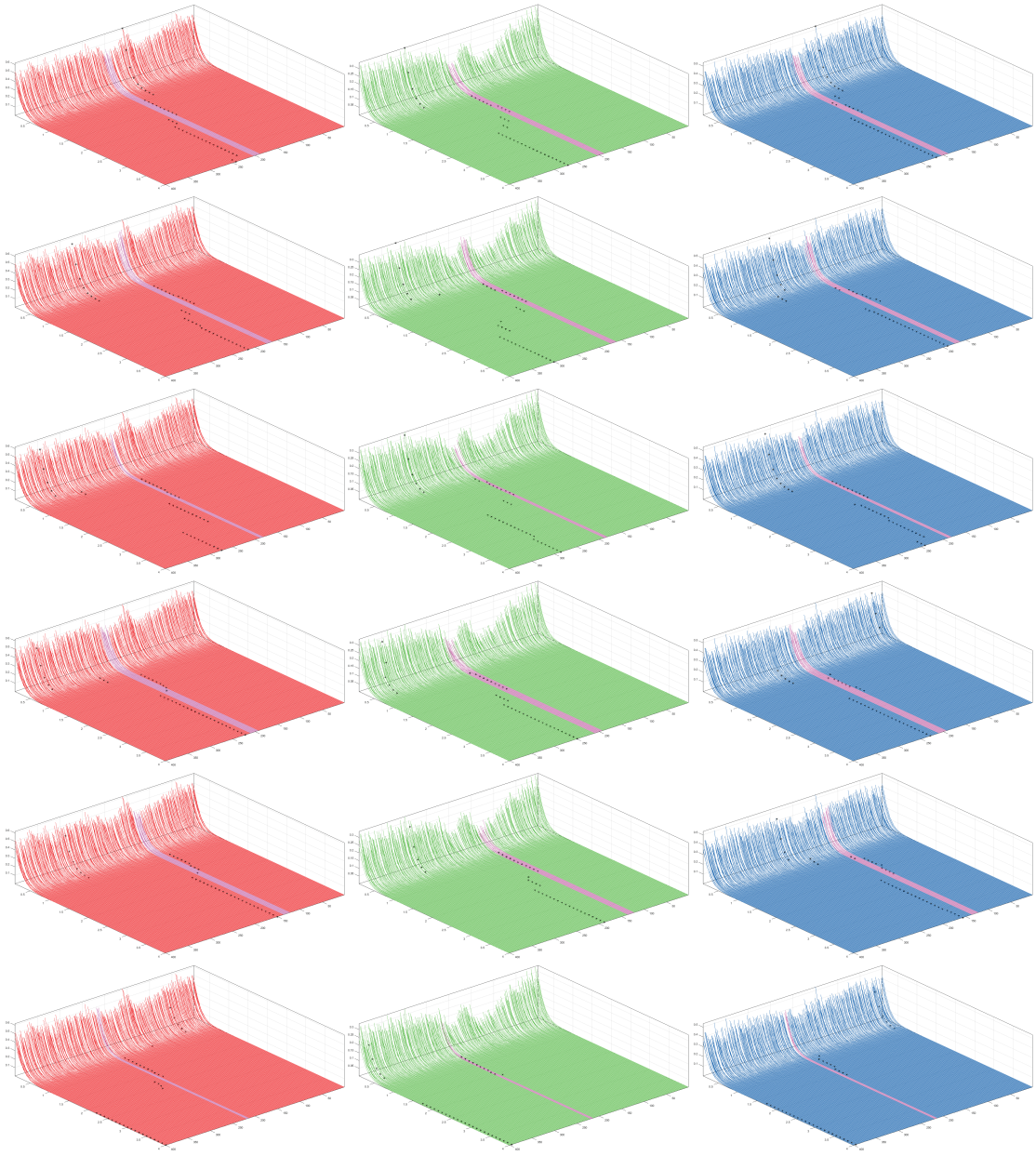

Figure 5.42: Each row shows different light condition - $1000mA$, $1500mA$, $2000mA$, $2500mA$, $3000mA$. Each column shows different color channel (red, green and blue). Violet lines show position of particles detected by algorithm for finding the core of PSF. Black stars are position of entropy (information) focus. In graphs the X axis are values of parameter α, Y axis show position in z-scan, and Z axis show value PIE.

6 Analysis and Discussion

I presented in this thesis new insight into a few of the crucial problems of optical microscopy. Especially problems around observing very small objects - problems of resolution, discriminability, distinguishability and focus. In these days are limits for detecting of small objects given by resolution (number of pixels) of used camera. Problems how to find focus usually depends on the operator of the microscope. This means that everyone who is using microscope should make experiments for measuring of the PSF. The knowledge of PSF will lead us to definition of optimal focus.

I also presented method for objective detection of focus using information entropy. We would like to use this method for setup our microscope and controlling of the microscope during experiments.

I explained some of the basic features of the distortion of the simple image of a light emanating object. Explanation of the influence of scattered light on the distortion is individual for each size and optical property of the observed object. The projection of the scattered light at the given optical axis' level reaches a lens and is then projected along the optical axis. The observed image then results from the interference of inhomogeneous wavefronts which brings about a very complicated pattern with several light intensity minima and maxima. The only general assumption which may be made is that at the position of focus, there should be the smallest discriminable image of the object accompanied by the minimal intensity of the electrical field.

Measurement of the PSFs was done using the microscope developed at the Institute of Complex Systems FFPW USB (see Chapter 4.1). Instead of the usage of a light point source we used 200-nm latex and 15-nm gold

nanoparticles (see 4.2). Size of the gold particles was beyond the theoretical resolution (for more information about the resolution, see Chapter 2.1.3) of the microscope and for its visualisation is necessary to use some special technique. A known method for the visualisation of sub-resolution objects is the video-enhanced microscopy (VEM) which is a special case of the ordinary bright field microscopy through the processing of images by the information entropy approach. [12, 83]

I was able to measure the PSF on our microscope under different condition and identify several parameters which are influencing the PSF. I compare theoretical parameters given by ENZ theory with parameters that I was able to identify from the results of experiments. I was not able to measure PSF under different wavelength due to construction of our microscope but this was substituted by analysis of individual color channels. It is not the same as using different wavelengths because the color channels still contains lot of different wavelengths (Fig. 6.1).

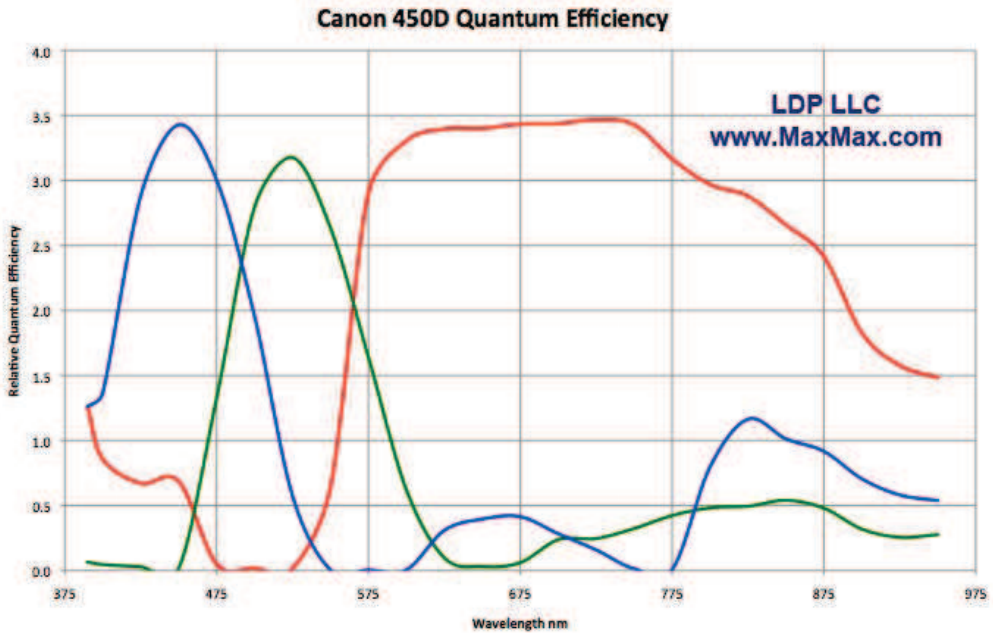

Figure 6.1: Spectral response of Canon 450D. Each color show sensitivity to different light wavelengths [84]. On the graphs is shown that blue pixels response also to signal from red and near infra-red (IR) part of spectra. The same case is with the green pixels. Red pixels also react on the signals from blue part of spectra.

This knowledge of the PSF can be used to improve our experiments. Also it can be used for image enhancement and for critical interpretation of its limits. It is possible to use measured PSF as a criterion for estimation of deconvolution kernel in blind deconvolution function. This knowledge was also used for definition of the focus and resolution (Fig. 2.8, 5.21, 5.33).

I also bring in the question about the resolution. The resolution is the feature of the experiment not of the measuring device. I showed that resolution is not the crucial for understanding of the image. Instead of using resolution as the measure of the quality of the image I suggest to use term discriminability.

I introduced several algorithms and procedures how to deal with presented problems. Calculation of information entropy can help with identifying more detailed structures in the image. Information entropy is also

one of the answers to definition of the objective focus.

When images with higher bit depth are acquired but cannot be processed as they are LIL conversion can helps. In the worst case the result of LIL conversion will be the same as conversion using standard methods but usually it preserves much more information.

Algorithm for detection of core in combination with difference algorithm is now used for analysis of living cells. This analysis allows to detect organelles and in-organelles structures. Next step in this analysis is preparation of 3D model of the cell.

7 Conclusion

New algorithms for the image analysis were developed and presented. Using these algorithms I was able to measure the information content of the image. Due to usage 12bit camera it was necessary to develop algorithm for transformation of 12bit images to 8bit to be able to visualize them and to preserve maximum information. This algorithm (LIL, sec: 5.1) can be basically used for every image not only for microscopy image. There was a need to find real position of the particle in Z-scan. To satisfy this need the algorithm for finding of the core of PSF was developed. This function allows us to find and detect real position of the object and even discriminate object (7.1) which should not be visible according to Abbe's definition.

These algorithms, developed mostly in collaboration with Renata Rychtáriková and Dalibor Štys form a basis for new concept of acquisition of images and analysis of their information content in brightfield microscopy. They substantiate respective patent application and are a basis of professional software whose usage may be extended into all fields of digital imaging.

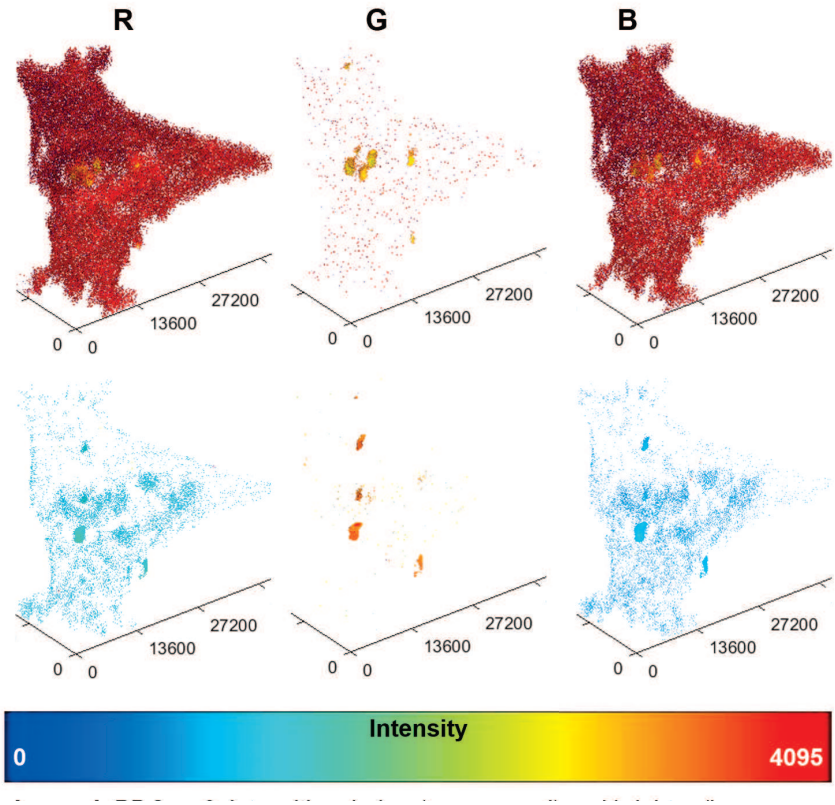

Figure 7.1: Image of Hela cell with detected organelles inside. $PDG_{\alpha=5} = 0$, intensities darker (upper row), and brighter (bottom row) than modus of background. Each column corresponds to different color channel. Height of the cell in Z axis is approx. $4.8\mu m$.

Algorithm for detection of the organelles and 3D reconstruction consists of acquiring Z-scan raw images with 12bit depth, detection of cell, detection of images in focus, export detected organelles and modelling of organelles and structure analysis. RAW images are debayerized without any interpolation to preserve images unchanged. Image is automatically separated to background and the cell. Point Information Entropy Density (PIED) is calculated for images of the cell. Images in focus are detected using clustering methods. Images of cell in the focus are processed by PDG calculation. PDG images, background and images of the cell are used as inputs for the script for organelles detection. Detection is based on the assumption that PSF (or Object Spread Function - OSF) of the stable object bigger than two z-steps is do not change in two consecutive images. This means that if difference between these two images gives zero on the position where the object is. This gives us the PDG model of the object.

To get image of the real object it is necessary to find the darkest part in detected object. This procedure is called finding the core of PSF (or OSF). When the object is detected in all possible images the 3D reconstruction follows.

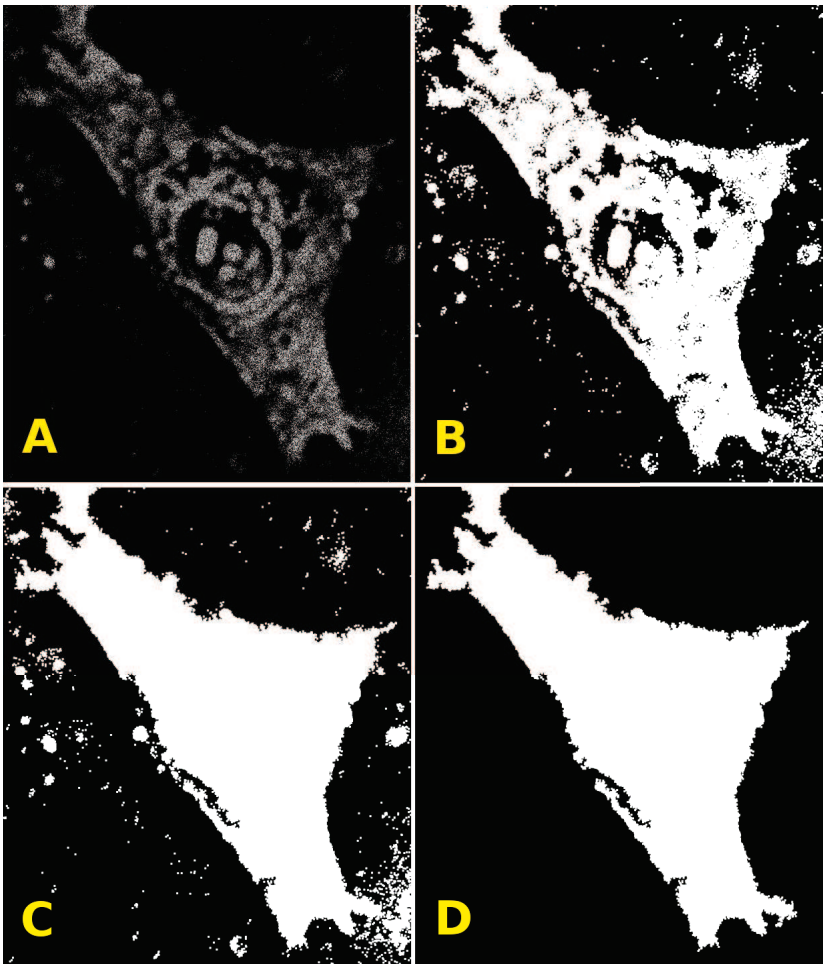

Figure 7.2: Cell detection. A - cumulative image, B - dilated cumulative image, C - mask with filled holes, D - mask after removing undesired objects. Automatic detection of the cell is based on on subtractive images. Binary mask is created from the subtractive image where the values of pixels are equal to zero. Binary mask is applied on the original image and dark intensities are taken into account. Cumulative image is made from the whole Z-scan. Cumulative image is dilated, holes are filled and undesired objects are removed.

I showed new approach for definition of the focus. Information focus defined as the position in which the image has maximum information content. For analysis of the whole object in 3D it is necessary to make a Z-scan. If the Z-scan contains enough image the position of the object can be find properly (PSF Core detection).

Models of PSF are mostly done for fluorescent (light emitting) microscopy due to this are not directly useful for bright-field (light diffracting) microscopy. They provide some information how the PSF looks at all levels along the z-axis, an aspect which is often overlooked in the interpretation of microscopic images.

Models and 3D reconstructions of real PSF's give us possibility to define proper focus. It is also possible to use models and 3D reconstructions to answer the question of resolution. I claim that the resolution is not the crucial parameter of the image. The crucial parameter is discriminability, because distance between two discriminable objects can be smaller than the distance between objects in the distance of resolution (eq. 2.16). Discriminable object can be still clearly seen as separated objects (Fig. 5.21, 5.22, 5.23).

Applying presented algorithms on the data from real experiment with nanoparticles results in the well positioned image of that particle (sec. 5.6). When are these algorithms applied on the image of the cell we are able to obtain almost complete 3D model of the mammalian living cell (Fig. 7.1).

Bibliography

[1] Jean-Baptiste Sibarita. Deconvolution microscopy. In *Microscopy Techniques*, pages 201–243. Springer, 2005.

[2] Joshua W Shaevitz and Daniel A Fletcher. Enhanced three-dimensional deconvolution microscopy using a measured depth-varying point-spread function. *JOSA A*, 24(9):2622–2627, 2007.

[3] James G McNally, Tatiana Karpova, John Cooper, and José Angel Conchello. Three-dimensional imaging by deconvolution microscopy. *Methods*, 19(3):373–385, 1999.

[4] BRA Nijboer. The diffraction theory of optical aberrations: Part I: General discussion of the geometrical aberrations. *Physica*, 10(8):679–692, 1943.

[5] Bernard Roelof Andries Nijboer. The diffraction theory of optical aberrations: Part II: diffraction pattern in the presence of small aberrations. *Physica*, 13(10):605–620, 1947.

[6] K Nienhuis and BRA Nijboer. The diffraction theory of optical aberrations: Part III: General formulae for small aberrations; experimental verification of the theoretical results. *Physica*, 14(9):590–608, 1949.

[7] Gustav Mie. Beiträge zur Optik trüber Medien, speziell kolloidaler metallösungen. *Annalen der physik*, 330(3):377–445, 1908.

[8] John W Strutt. XV. On the light from the sky, its polarization and colour. *The London, Edinburgh, and Dublin Philosophical Magazine and Journal of Science*, 41(271):107–120, 1871.

[9] John William Strutt Baron Rayleigh. *On the scattering of light by small particles*. 1871.

[10] John W Strutt and Lord Rayleigh. On the electromagnetic theory of light. *Phil. Mag*, 12:81–101, 1881.

[11] Lord Rayleigh. XXXIV. On the transmission of light through an atmosphere containing small particles in suspension, and on the origin of the blue of the sky. *The London, Edinburgh, and Dublin Philosophical Magazine and Journal of Science*, 47(287):375–384, 1899.

[12] Yoshihiko Mizushima. Detectivity limit of very small objects by video-enhanced microscopy. *Applied optics*, 27(12):2587–2594, 1988.

[13] IK Lichtscheidl and I Foissner. Video microscopy of dynamic plant cell organelles: principles of the technique and practical application. *Journal of Microscopy*, 181(2):117–128, 1996.

[14] SG Lipson. Why is super-resolution so inefficient? *Micron*, 34(6):309–312, 2003.

[15] Ignacio Izeddin, Mohamed El Beheiry, Jordi Andilla, Daniel Ciepielewski, Xavier Darzacq, and Maxime Dahan. PSF shaping using adaptive optics for three-dimensional single-molecule super-resolution imaging and tracking. *Optics express*, 20(5):4957–4967, 2012.

[16] Gregory Bothun. Atmospheric Stuff, 2015.

[17] ERNST Meyer. Atomic force microscopy. *Progress in surface science*, 41(1):3–49, 1992.

[18] Steven K Buratto. Near-field scanning optical microscopy. *Current Opinion in Solid State and Materials Science*, 1(4):485–492, 1996.

[19] Robert C Dunn. Near-field scanning optical microscopy. *Chemical reviews*, 99(10):2891–2928, 1999.

[20] Lothar Schermelleh, Rainer Heintzmann, and Heinrich Leonhardt. A guide to super-resolution fluorescence microscopy. *The Journal of cell biology*, 190(2):165–175, 2010.

[21] Bonnie O Leung and Keng C Chou. Review of super-resolution fluorescence microscopy for biology. *Applied spectroscopy*, 65(9):967–980, 2011.

[22] Mats GL Gustafsson. Surpassing the lateral resolution limit by a factor of two using structured illumination microscopy. *Journal of microscopy*, 198(2):82–87, 2000.

[23] Mats GL Gustafsson. Nonlinear structured-illumination microscopy: wide-field fluorescence imaging with theoretically unlimited resolution. *Proceedings of the National Academy of Sciences of the United States of America*, 102(37):13081–13086, 2005.

[24] Dan Dan, Baoli Yao, and Ming Lei. Structured illumination microscopy. *Optical Nanoscopy and Novel Microscopy Techniques*, page 23, 2014.

[25] Manish Saxena, Gangadhar Eluru, and Sai Siva Gorthi. Structured illumination microscopy. *Advances in Optics and Photonics*, 7(2):241–275, 2015.

[26] Jörg Bewersdorf, Alexander Egner, and Stefan W Hell. 4pi microscopy. In *Handbook of biological confocal microscopy*, pages 561–570. Springer, 2006.

[27] Marion C Lang, Johann Engelhardt, and Stefan W Hell. 4pi microscopy with linear fluorescence excitation. *Optics letters*, 32(3):259–261, 2007.

[28] Michael J Rust, Mark Bates, and Xiaowei Zhuang. Sub-diffraction-limit imaging by stochastic optical reconstruction microscopy (STORM). *Nature methods*, 3(10):793–796, 2006.

[29] Bo Huang, Wenqin Wang, Mark Bates, and Xiaowei Zhuang. Three-dimensional super-resolution imaging by stochastic optical reconstruction microscopy. *Science*, 319(5864):810–813, 2008.

[30] Samuel T Hess, Thanu PK Girirajan, and Michael D Mason. Ultra-high resolution imaging by fluorescence photoactivation localization microscopy. *Biophysical journal*, 91(11):4258–4272, 2006.

[31] Travis J Gould, Vladislav V Verkhusha, and Samuel T Hess. Imaging biological structures with fluorescence photoactivation localization microscopy. *Nature protocols*, 4(3):291–308, 2009.

[32] Stefan W Hell and Jan Wichmann. Breaking the diffraction resolution limit by stimulated emission: stimulated-emission-depletion fluorescence microscopy. *Optics letters*, 19(11):780–782, 1994.

[33] Thomas A Klar, Egbert Engel, and Stefan W Hell. Breaking Abbes diffraction resolution limit in fluorescence microscopy with stimulated emission depletion beams of various shapes. *Physical Review E*, 64(6):066613, 2001.

[34] Wouter Sempels, Sebastian Bernig, Kris Janssen, Maarten Roeffaers, and Johan Hofkens. STimulated Emission Depletion Microscopy. *status: published*, 2011.

[35] Tomáš Náhlík and Dalibor Štys. Microscope point spread function, focus and calculation of optimal microscope set-up. *International Journal of Computer Mathematics*, 91(2):221–232, 2014.

[36] Dalibor Štys. *Technické a teoretické aspekty mikroskopie živé buňky.* České vysoké učení technické, 2012.

[37] Sidney F Ray. *Applied photographic optics: Lenses and optical systems for photography, film, video, electronic and digital imaging.* Focal Press, 2002.

[38] Duane C Brown. Decentering distortion of lenses. *Photometric Engineering*, 32(3):444–462, 1966.

[39] Max Born and Emil Wolf. *Principles of optics: electromagnetic theory of propagation, interference and diffraction of light.* Cambridge university press, 1999.

[40] Robert Edward Fischer, Biljana Tadic-Galeb, Paul R Yoder, and Ranko Galeb. *Optical system design*. Citeseer, 2000.

[41] Luis Alvarez, Luis Gomez, and J Rafael Sendra. Algebraic lens distortion model estimation. *Image Processing On Line*, (2010), 2010.

[42] Lichtscheidl I.K. Volgger, M. Lichtmikroskopie online - Theorie und Anwendung, 2008.

[43] Nikon Instruments Inc. Nikon Instruments - Learn & Explore, 2015.

[44] Olympus America Inc. Olympus Microscopy Resource Center, 2015.

[45] Ernst Abbe. Ueber einen neuen Beleuchtungsapparat am Mikroskop. *Archiv für mikroskopische Anatomie*, 9(1):469–480, 1873.

[46] Jan Urban, Nils Kristian Afseth, and Dalibor Štys. Fundamental definitions and confusions in mass spectrometry about mass assignment, centroiding and resolution. *TrAC Trends in Analytical Chemistry*, 53:126–136, 2014.

[47] Werner Heisenberg. *The physical principles of the quantum theory*. Courier Corporation, 2013.

[48] Michael Richmond. Heisenberg's Microscope, 2015.

[49] Joseph Braat, Peter Dirksen, and Augustus JEM Janssen. Assessment of an extended Nijboer–Zernike approach for the computation of optical point-spread functions. *JOSA A*, 19(5):858–870, 2002.

[50] Joseph JM Braat, Sven van Haver, Augustus JEM Janssen, and Peter Dirksen. Assessment of optical systems by means of point-spread functions. *Progress in Optics*, 51:349–468, 2008.

[51] Joseph JM Braat, Sven van Haver, Augustus JEM Janssen, and Peter Dirksen. Extended Nijboer-Zernike (ENZ) Analysis and Aberration Retrieval, 2015.

[52] Kardi Teknomo. K-means clustering tutorial. *Medicine*, 100(4):3, 2006.

[53] Nobuyuki Otsu. A threshold selection method from gray-level histograms. *Automatica*, 11(285-296):23–27, 1975.

[54] Serge Beucher and Fernand Meyer. The morphological approach to segmentation: the watershed transformation. *OPTICAL ENGINEERING-NEW YORK-MARCEL DEKKER INCORPORATED-*, 34:433–433, 1992.

[55] Serge Beucher. Watershed, hierarchical segmentation and waterfall algorithm. In *Mathematical morphology and its applications to image processing*, pages 69–76. Springer, 1994.

[56] Timothy F Cootes, Christopher J Taylor, David H Cooper, and Jim Graham. Active shape models-their training and application. *Computer vision and image understanding*, 61(1):38–59, 1995.

[57] Philippe Andrey. Selectionist relaxation: genetic algorithms applied to image segmentation. *Image and Vision Computing*, 17(3):175–187, 1999.

[58] Ujjwal Maulik and Sanghamitra Bandyopadhyay. Genetic algorithm-based clustering technique. *Pattern recognition*, 33(9):1455–1465, 2000.

[59] Dae N Chun and Hyun S Yang. Robust image segmentation using genetic algorithm with a fuzzy measure. *Pattern recognition*, 29(7):1195–1211, 1996.

[60] Michael Egmont-Petersen, Dick de Ridder, and Heinz Handels. Image processing with neural networksa review. *Pattern recognition*, 35(10):2279–2301, 2002.

[61] Mohamed A El-Sayed and Hamida AM Sennari. Multi-threshold algorithm based on Havrda and Charvat entropy for edge detection in satellite grayscale images. *Journal of Software Engineering and Applications*, 2014, 2013.

[62] Baljit Singh and Amar Partap Singh. Edge detection in gray level images based on the Shannon entropy 1. 2008.

[63] Mohamed A El-Sayed. Edges detection based on renyi entropy with split/merge. *Computer Engineering and Intelligent Systems*, 3(9):32–41, 2012.

[64] M Portes de Albuquerque, IA Esquef, and AR Gesualdi Mello. Image thresholding using Tsallis entropy. *Pattern Recognition Letters*, 25(9):1059–1065, 2004.

[65] Carlos AB Mello and Luciana A Schuler. Thresholding images of historical documents using a Tsallis-entropy based algorithm. *Journal of Software*, 3(6):29–36, 2008.

[66] Yan Li, Xiaoping Fan, and Gang Li. Image segmentation based on Tsallis-entropy and Renyi-entropy and their comparison. In *Industrial Informatics, 2006 IEEE International Conference on*, pages 943–948. IEEE, 2006.

[67] Jan Urban, Jan Vanek, and Dalibor Stys. Preprocessing of microscopy images via Shannon's entropy. 2009.

[68] Jan Urban and Jan Vanek. Preprocessing of microscopy images via Shannon's entropy on GPU. *GraVisMa 2009*, page 48.

[69] J Urban. Automatic image segmentation of hela cells in phase contrast microphotography. *Lap LAMBERT Academic Publishing, Germany*, 2012.

[70] Anna Zhyrova, Dalibor Stys, and Petr Cisar. Information entropy approach as a method of analysing belousov-zhabotinsky reaction wave formation. *CHEMICKE LISTY*, 107:S341–S342, 2013.

[71] Jan Urban, Jan Vanek, and Dalibor Stys. Maximisation of image contrast in label-free microscopy of living cells using information entropy computation. In *Cytokinematics 2009 Microscopy of Live Cells in the Post Genomics Era*, 2009.

[72] Tomas Nahlik, Dalibor Stys, Jan Urban, and Petr Cisar. Shannon and Rényi entropy in microscope image processing. In *Microscale Bioseparations*, 2010.

[73] Tomáš Náhlík, Jan Urban, Dalibor Štys, Petr Císař, Aliaksandr Pautsina, and Jan Vaněk. The state trajectory of cell using Rényi entropy coefficients. *Procedia Computer Science*, 7:212–213, 2011.

[74] T Náhlík, J Urban, P Císař, J Vaněk, and D Štys. Entropy based approximation to cell monolayer development. In *5th European Conference of the International Federation for Medical and Biological Engineering*, pages 563–566. Springer, 2012.

[75] Claude Elwood Shannon. A mathematical theory of communication. *ACM SIGMOBILE Mobile Computing and Communications Review*, 5(1):3–55, 2001.

[76] Amar Partap Singh Pharwaha and Baljit Singh. Shannon and Non-Shannon measures of entropy for statistical texture feature extraction in digitized mammograms. In *proceedings of the World Congress on Engineering and Computer Science*, volume 2, pages 20–22, 2009.

[77] Renata Rychtarikova, Tomas Nahlik, Rebecca Smaha, Jan Urban, Dalibor Stys Jr, Petr Cisar, and Dalibor Stys. Multifractality in imaging: Application of information entropy for observation of inner dynamics inside of an unlabeled living cell in bright-field microscopy. In *ISCS 2014: Interdisciplinary Symposium on Complex Systems*, pages 261–267. Springer, 2015.

[78] The MathWorks Inc. MathWorks - MATLAB and Simulink for technical computing, 2015.

[79] Boaz Tamir and Eliahu Cohen. Introduction to weak measurements and weak values. *Quanta*, 2(1):7–17, 2013.

[80] Dalibor Štys, Jan Urban, Jan Vaněk, and Petr Císař. Analysis of biological time-lapse microscopic experiment from the point of view of the information theory. *Micron*, 42(4):360–365, 2011.

[81] Dalibor Stys, Jan Vanek, Tomas Nahlik, Jan Urban, and Petr Cisar. The cell monolayer trajectory from the system state point of view. *Molecular biosystems*, 7(10):2824–2833, 2011.

[82] Dalibor Štys, Petr Jizba, Štěpán Papáček, Tomáš Náhlík, and Petr Císař. On measurement of internal variables of complex self-organized systems and their relation to multifractal spectra. In *Self-Organizing Systems*, pages 36–47. Springer, 2012.

[83] DM Shotton. Video-enhanced light microscopy and its applications in cell biology. *Journal of cell science*, 89(2):129–150, 1988.

[84] Maxmax. LDL LLC - www.maxmax.com, 2015.

Appendices

A CLSM Experimental setup

Description of CLSM Experimental setup as it was exported from Leica software.

Image: **0.14_Z-Series-1**

Size: **17.04 MB**

File Location:
D:\users\Wolfram\Microbeads_14102014.lif

Start Time: **10/14/2014 2:27:17 PM.571**

End Time: **10/14/2014 2:55:15 PM.018**

Total Exposures: **65 (1 channels, 65 frames)**

Dimensions

Dimension	Logical Size	Physical Length	Physical Origin
X	512	49.21 µm	71.34 µm
Y	512	49.21 µm	-1.32 µm
Z	65	-8.06 µm	-1.00 µm

Scanner Settings

SuperContVisible Shutter	0
UV Shutter	1
Visible Shutter	0
ScanMode	xyz
Pinhole [m]	102.9 µm
Pinhole [airy]	1.00
Size-Width	49.2 µm
Size-Height	49.2 µm
Size-Depth	-8.1 µm
StepSize	0.13 µm
Voxel-Width	96.3 nm
Voxel-Height	96.3 nm
Voxel-Depth	125.9 nm
Voxel-Volume	1167557.571 nm³
Zoom	5.0
Scan-Direction	1
SequentialMode	0
Frame-Accumulation	1
Frame-Average	1
Line-Average	5
Resolution	8 bits
Channels	1
Format-Width	512 pixels
Format-Height	512 pixels
Line-Accumulation	1
Sections	65

Scanner Settings Details (Show)

Hardware Settings

WLL AOTF (470)	0.00 %
WLL AOTF (471)	0.00 %
WLL AOTF (472)	0.00 %
WLL AOTF (473)	0.00 %
WLL AOTF (667)	0.00 %
WLL AOTF (668)	0.00 %
WLL AOTF (669)	0.00 %
WLL AOTF (670)	0.00 %
AOTF (405)	70.00 %
AOTF (458)	0.00 %
AOTF (476)	0.00 %
AOTF (488)	0.00 %
AOTF (496)	0.00 %
AOTF (514)	0.00 %
PMT 1	Active
PMT 1 (Offs.)	-0.2 %
PMT 1 (HV)	1029.1
PMT 1 (HV_Unit)	V
PMT 1 (Preamp)	Direct
PMT 2	Inactive
PMT 3	Inactive
PMT 4	Inactive
PMT Trans	Inactive
System Number	5100001358
Laser (405 Diode, UV)	On
Laser (Argon, visible)	Off
Laser (Argon, visible) (Power)	-11 %
Laser (WLL, WLL)	Off
Scan Field Rotation	0 degrees
Z Scan Actuator (POS)	0.000 µm
Scan Speed	100 Hz
Objective	HCX PL APO CS 63.0x1.30 GLYC 21°C UV
Numerical aperture (Obj.)	1.30
Refraction index	1.45
DM6000 Stage Pos x	0.00386012009393
DM6000 Stage Pos y	0.01516290727565
Emission bandwidth PMT 1: begin - end	425nm - 610nm

Hardware Settings Details (Hide)

AOBS (0)	Intensity	0
AOBS (1)	Intensity	0
AOBS (2)	Intensity	0
AOBS (3)	Intensity	0
AOBS (4)	Intensity	0
AOBS (5)	Intensity	0

AOBS (6)	Intensity	0
AOBS (7)	Intensity	0
AOBS (0)	Intensity	0
AOBS (1)	Intensity	0
AOBS (2)	Intensity	0
AOBS (3)	Intensity	0
AOBS (4)	Intensity	0
AOBS (5)	Intensity	0
AOBS (6)	Intensity	0
AOBS (7)	Intensity	0
Constant Power Lambda Begin	ConstantPowerLambdaBegin	0
Constant Power Lambda End	ConstantPowerLambdaEnd	0
Constant Power Mode	ConstantPowerMode	0
AOTF (470)	Intensity	0.00
AOTF (471)	Intensity	0.00
AOTF (472)	Intensity	0.00
AOTF (473)	Intensity	0.00
AOTF (667)	Intensity	0.00
AOTF (668)	Intensity	0.00
AOTF (669)	Intensity	0.00
AOTF (670)	Intensity	0.00
AOTF (470)	CheckState	0.00
AOTF (471)	CheckState	0.00
AOTF (472)	CheckState	0.00
AOTF (473)	CheckState	0.00
AOTF (667)	CheckState	0.00
AOTF (668)	CheckState	0.00
AOTF (669)	CheckState	0.00
AOTF (670)	CheckState	0.00
AOTF (470)	UIVisibleState	1.00
AOTF (471)	UIVisibleState	0.00
AOTF (472)	UIVisibleState	0.00
AOTF (473)	UIVisibleState	0.00
AOTF (667)	UIVisibleState	0.00
AOTF (668)	UIVisibleState	0.00
AOTF (669)	UIVisibleState	0.00
AOTF (670)	UIVisibleState	0.00
AOTF (470)	Intensity	0.00
AOTF (471)	Intensity	0.00
AOTF (472)	Intensity	0.00
AOTF (473)	Intensity	0.00
AOTF (667)	Intensity	0.00
AOTF (668)	Intensity	0.00
AOTF (669)	Intensity	0.00

AOTF (670)	Intensity	0.00
AOTF (405)	Intensity	70.00
AOTF (405)	Intensity	0.00
AOTF (458)	Intensity	0.00
AOTF (476)	Intensity	0.00
AOTF (488)	Intensity	0.00
AOTF (496)	Intensity	0.00
AOTF (514)	Intensity	0.00
AOTF (458)	Intensity	0.00
AOTF (476)	Intensity	0.00
AOTF (488)	Intensity	0.00
AOTF (496)	Intensity	0.00
AOTF (514)	Intensity	0.00
PMT 1	State	Active
PMT 1 (Offs.)	VideoOffset	-0.2
PMT 1 (HV)	HighVoltage	1029.1
PMT 1 (HV_Unit)	HighVoltageUnit	V
PMT 1 (Preamp)	PreampMode	Direct
PMT 2	State	Inactive
PMT 3	State	Inactive
PMT 4	State	Inactive
PMT Trans	State	Inactive
Galvo Slider	Filter	Galvo X Normal
Polarization FW	Filter	Empty 1
Reson. Galvo Pan	Filter	Galvo X Pan Center
Target Slider	Filter	Target Park
UV Lens FW	Filter	Lens 63x/1.30 GLYC
Hardware Type No.	Machine_Type	7
System Number	System_Number	5100001358
Laser (405 Diode, UV)	Power State	On
Laser (Argon, visible)	Power State	Off
Laser (Argon, visible) (Power)	Output Power	-11 %
Laser (WLL, WLL)	Power State	Off
TLD_Settings	TLD_Settings	100
RLD_Settings	RLD_Settings	-1
Scan Field Rotation	Scan Rotation	0
Rotation Direction	Rotation Direction	1
X Scan Actuator	ScanPlane	Active
X Scan Actuator (POS)	IsWholeRangeOfSuperZEnabled	0
X Scan Actuator (Gain)	Gain	5.00000476837613
X Scan Actuator (Offs.)	Offset	0.00449420584077
Y Scan Actuator	ScanPlane	Active
Y Scan Actuator (POS)	IsWholeRangeOfSuperZEnabled	0
Y Scan Actuator (Gain)	Gain	5.00000476837613
Y Scan Actuator (Offs.)	Offset	-8.32592249976755E-05

Z Scan Actuator	ScanPlane	Inactive
Z Scan Actuator (POS)	IsWholeRangeOfSuperZEnabled	0
Z Scan Actuator (POS)	Position	0.000
Scan Speed	Speed	100
Phase	Phase	-34.346532387274
Y-Phase	Y-Phase	0
SMD-Phase	SMD-Phase	0
SP Mirror Channel 1 (left)	Wavelength	425.0
SP Mirror Channel 1 (right)	Wavelength	610.0
SP Mirror Channel 2 (left)	Wavelength	616.8
SP Mirror Channel 2 (right)	Wavelength	669.0
SP Mirror Channel 3 (left)	Wavelength	669.0
SP Mirror Channel 3 (right)	Wavelength	721.3
SP Mirror Channel 4 (left)	Wavelength	721.3
SP Mirror Channel 4 (right)	Wavelength	773.8
Magnification-Changer	Magnification	SCANx
Position	Position	1
Objective	Objective	HCX PL APO CS 63.0x1.30 GLYC 21°C UV
Order number (Obj.)	OrderNumber	11506194
Numerical aperture (Obj.)	NumericalAperture	1.30
Refraction index	RefractionIndex	1.45
DM6000 Stage XOrigin	XPosOrigin	0
DM6000 Stage YOrigin	YPosOrigin	0
DM6000 Stage ZOrigin	ZPosOrigin	0
DM6000 Stage Pos x	XPos	0.00386012009393
DM6000 Stage Pos y	YPos	0.01516290727565
Emission bandwidth PMT 1: begin - end	Bandwidth	425nm - 610nm
DM6000 Stage Pos z	ZPos	0

Time Stamps:

Frame (Show All)	**Relative Time (s)**	**Absolute Time (h:m:s.ms)**	**Date**
1	0	2:27:17 PM.571	10/14/2014
65	1677.447	2:55:15 PM.18	10/14/2014

Image: **0.22_Z-Series-1**

Size: **14.42 MB**

File Location:
D:\users\Wolfram\Microbeads_14102014.lif

Start Time: **10/14/2014 10:42:13 AM.172**

End Time: **10/14/2014 10:56:22 AM.595**

Total Exposures: **55 (1 channels, 55 frames)**

Dimensions

Dimension	Logical Size	Physical Length	Physical Origin
X	512	49.21 µm	86.93 µm
Y	512	49.21 µm	-87.74 µm
Z	55	6.80 µm	-13.85 µm

Scanner Settings

SuperContVisible Shutter	0
UV Shutter	1
Visible Shutter	0
ScanMode	xyz
Pinhole [m]	102.9 µm
Pinhole [airy]	1.00
Size-Width	49.2 µm
Size-Height	49.2 µm
Size-Depth	6.8 µm
StepSize	0.13 µm
Voxel-Width	96.3 nm
Voxel-Height	96.3 nm
Voxel-Depth	125.9 nm
Voxel-Volume	1167557.571 nm³
Zoom	5.0
Scan-Direction	1
SequentialMode	0
Frame-Accumulation	1
Frame-Average	1
Line-Average	3
Resolution	8 bits
Channels	1
Format-Width	512 pixels
Format-Height	512 pixels
Line-Accumulation	1
Sections	55

Scanner Settings Details (Show)

Hardware Settings

WLL AOTF (470)	0.00 %
WLL AOTF (471)	0.00 %
WLL AOTF (472)	0.00 %
WLL AOTF (473)	0.00 %
WLL AOTF (667)	0.00 %
WLL AOTF (668)	0.00 %
WLL AOTF (669)	0.00 %
WLL AOTF (670)	0.00 %
AOTF (405)	60.00 %
AOTF (458)	59.00 %
AOTF (476)	0.00 %
AOTF (488)	0.00 %
AOTF (496)	0.00 %
AOTF (514)	0.00 %
PMT 1	Inactive
PMT 2	Active
PMT 2 (Offs.)	-0.1 %
PMT 2 (HV)	841.9
PMT 2 (HV_Unit)	V
PMT 2 (Preamp)	Direct
PMT 3	Inactive
PMT 4	Inactive
PMT Trans	Inactive
System Number	5100001358
Laser (405 Diode, UV)	On
Laser (Argon, visible)	On
Laser (Argon, visible) (Power)	25 %
Laser (WLL, WLL)	Off
Scan Field Rotation	0 degrees
Z Scan Actuator (POS)	0.000 µm
Scan Speed	100 Hz
Objective	HCX PL APO CS 63.0x1.30 GLYC 21°C UV
Numerical aperture (Obj.)	1.30
Refraction index	1.45
DM6000 Stage Pos x	0.0087295853742
DM6000 Stage Pos y	0.01131119538054
Emission bandwidth PMT 2: begin - end	425nm - 609nm

Hardware Settings Details (Hide)

AOBS (0)	Intensity	0
AOBS (1)	Intensity	100
AOBS (2)	Intensity	0
AOBS (3)	Intensity	0
AOBS (4)	Intensity	0
AOBS (5)	Intensity	0

AOBS (6)	Intensity	0
AOBS (7)	Intensity	0
AOBS (0)	Intensity	0
AOBS (1)	Intensity	0
AOBS (2)	Intensity	0
AOBS (3)	Intensity	0
AOBS (4)	Intensity	0
AOBS (5)	Intensity	0
AOBS (6)	Intensity	0
AOBS (7)	Intensity	0
Constant Power Lambda Begin	ConstantPowerLambdaBegin	0
Constant Power Lambda End	ConstantPowerLambdaEnd	0
Constant Power Mode	ConstantPowerMode	0
AOTF (470)	Intensity	0.00
AOTF (471)	Intensity	0.00
AOTF (472)	Intensity	0.00
AOTF (473)	Intensity	0.00
AOTF (667)	Intensity	0.00
AOTF (668)	Intensity	0.00
AOTF (669)	Intensity	0.00
AOTF (670)	Intensity	0.00
AOTF (470)	CheckState	0.00
AOTF (471)	CheckState	0.00
AOTF (472)	CheckState	0.00
AOTF (473)	CheckState	0.00
AOTF (667)	CheckState	0.00
AOTF (668)	CheckState	0.00
AOTF (669)	CheckState	0.00
AOTF (670)	CheckState	0.00
AOTF (470)	UIVisibleState	1.00
AOTF (471)	UIVisibleState	0.00
AOTF (472)	UIVisibleState	0.00
AOTF (473)	UIVisibleState	0.00
AOTF (667)	UIVisibleState	0.00
AOTF (668)	UIVisibleState	0.00
AOTF (669)	UIVisibleState	0.00
AOTF (670)	UIVisibleState	0.00
AOTF (470)	Intensity	0.00
AOTF (471)	Intensity	0.00
AOTF (472)	Intensity	0.00
AOTF (473)	Intensity	0.00
AOTF (667)	Intensity	0.00
AOTF (668)	Intensity	0.00
AOTF (669)	Intensity	0.00

AOTF (670)	Intensity	0.00
AOTF (405)	Intensity	60.00
AOTF (405)	Intensity	0.00
AOTF (458)	Intensity	59.00
AOTF (476)	Intensity	0.00
AOTF (488)	Intensity	0.00
AOTF (496)	Intensity	0.00
AOTF (514)	Intensity	0.00
AOTF (458)	Intensity	0.00
AOTF (476)	Intensity	0.00
AOTF (488)	Intensity	0.00
AOTF (496)	Intensity	0.00
AOTF (514)	Intensity	0.00
PMT 1	State	Inactive
PMT 2	State	Active
PMT 2 (Offs.)	VideoOffset	-0.1
PMT 2 (HV)	HighVoltage	841.9
PMT 2 (HV_Unit)	HighVoltageUnit	V
PMT 2 (Preamp)	PreampMode	Direct
PMT 3	State	Inactive
PMT 4	State	Inactive
PMT Trans	State	Inactive
Galvo Slider	Filter	Galvo X Normal
Polarization FW	Filter	Empty 1
Reson. Galvo Pan	Filter	Galvo X Pan Center
Target Slider	Filter	Target Park
UV Lens FW	Filter	Lens 63x/1.30 GLYC
Hardware Type No.	Machine_Type	7
System Number	System_Number	5100001358
Laser (405 Diode, UV)	Power State	On
Laser (Argon, visible)	Power State	On
Laser (Argon, visible) (Power)	Output Power	25 %
Laser (WLL, WLL)	Power State	Off
TLD_Settings	TLD_Settings	100
RLD_Settings	RLD_Settings	-1
Scan Field Rotation	Scan Rotation	0
Rotation Direction	Rotation Direction	1
X Scan Actuator	ScanPlane	Active
X Scan Actuator (POS)	IsWholeRangeOfSuperZEnabled	0
X Scan Actuator (Gain)	Gain	5.00000476837613
X Scan Actuator (Offs.)	Offset	5.47652057191767E-03
Y Scan Actuator	ScanPlane	Active
Y Scan Actuator (POS)	IsWholeRangeOfSuperZEnabled	0
Y Scan Actuator (Gain)	Gain	5.00000476837613
Y Scan Actuator (Offs.)	Offset	-5.52738889114062E-03

Z Scan Actuator	ScanPlane	Inactive
Z Scan Actuator (POS)	IsWholeRangeOfSuperZEnabled	0
Z Scan Actuator (POS)	Position	0.000
Scan Speed	Speed	100
Phase	Phase	-34.346532387274
Y-Phase	Y-Phase	0
SMD-Phase	SMD-Phase	0
SP Mirror Channel 1 (left)	Wavelength	385.0
SP Mirror Channel 1 (right)	Wavelength	400.6
SP Mirror Channel 2 (left)	Wavelength	425.3
SP Mirror Channel 2 (right)	Wavelength	609.2
SP Mirror Channel 3 (left)	Wavelength	669.0
SP Mirror Channel 3 (right)	Wavelength	721.3
SP Mirror Channel 4 (left)	Wavelength	747.8
SP Mirror Channel 4 (right)	Wavelength	800.0
Magnification-Changer	Magnification	SCANx
Position	Position	1
Objective	Objective	HCX PL APO CS 63.0x1.30 GLYC 21°C UV
Order number (Obj.)	OrderNumber	11506194
Numerical aperture (Obj.)	NumericalAperture	1.30
Refraction index	RefractionIndex	1.45
DM6000 Stage XOrigin	XPosOrigin	0
DM6000 Stage YOrigin	YPosOrigin	0
DM6000 Stage ZOrigin	ZPosOrigin	0
DM6000 Stage Pos x	XPos	0.0087295853742
DM6000 Stage Pos y	YPos	0.01131119538054
Emission bandwidth PMT 2: begin - end	Bandwidth	425nm - 609nm
DM6000 Stage Pos z	ZPos	0

Time Stamps:

Frame (Show All)	**Relative Time (s)**	**Absolute Time (h:m:s.ms)**	**Date**
1	0	10:42:13 AM.172	10/14/2014
55	849.423	10:56:22 AM.595	10/14/2014

Image: **0.53_Z-Series-2**

Size: **17.56 MB**

File Location:
D:\users\Wolfram\Microbeads_14102014.lif

Start Time: **10/14/2014 10:27:11 AM.387**

End Time: **10/14/2014 10:34:23 AM.852**

Total Exposures: **67 (1 channels, 67 frames)**

Dimensions

Dimension	Logical Size	Physical Length	Physical Origin
X	512	49.21 µm	0.00 µm
Y	512	49.21 µm	0.00 µm
Z	67	8.31 µm	-1.85 µm

Scanner Settings

SuperContVisible Shutter	0
UV Shutter	1
Visible Shutter	0
ScanMode	xyz
Pinhole [m]	102.9 µm
Pinhole [airy]	1.00
Size-Width	49.2 µm
Size-Height	49.2 µm
Size-Depth	8.3 µm
StepSize	0.13 µm
Voxel-Width	96.3 nm
Voxel-Height	96.3 nm
Voxel-Depth	125.9 nm
Voxel-Volume	1167557.571 nm³
Zoom	5.0
Scan-Direction	1
SequentialMode	0
Frame-Accumulation	1
Frame-Average	1
Line-Average	5
Resolution	8 bits
Channels	1
Format-Width	512 pixels
Format-Height	512 pixels
Line-Accumulation	1
Sections	67

Scanner Settings Details (Show)

Hardware Settings

WLL AOTF (470)	0.00 %
WLL AOTF (471)	0.00 %
WLL AOTF (472)	0.00 %
WLL AOTF (473)	0.00 %
WLL AOTF (667)	0.00 %
WLL AOTF (668)	0.00 %
WLL AOTF (669)	0.00 %
WLL AOTF (670)	0.00 %
AOTF (405)	25.00 %
AOTF (458)	59.00 %
AOTF (476)	0.00 %
AOTF (488)	0.00 %
AOTF (496)	0.00 %
AOTF (514)	0.00 %
PMT 1	Inactive
PMT 2	Active
PMT 2 (Offs.)	-0.1 %
PMT 2 (HV)	939.4
PMT 2 (HV_Unit)	V
PMT 2 (Preamp)	Direct
PMT 3	Inactive
PMT 4	Inactive
PMT Trans	Inactive
System Number	5100001358
Laser (405 Diode, UV)	On
Laser (Argon, visible)	On
Laser (Argon, visible) (Power)	25 %
Laser (WLL, WLL)	Off
Scan Field Rotation	0 degrees
Z Scan Actuator (POS)	0.000 µm
Scan Speed	400 Hz
Objective	HCX PL APO CS 63.0x1.30 GLYC 21°C UV
Numerical aperture (Obj.)	1.30
Refraction index	1.45
DM6000 Stage Pos x	0.0238330444381
DM6000 Stage Pos y	0.02511813655357
Emission bandwidth PMT 2: begin - end	425nm - 605nm

Hardware Settings Details (Hide)

AOBS (0)	Intensity	0
AOBS (1)	Intensity	100
AOBS (2)	Intensity	0
AOBS (3)	Intensity	0
AOBS (4)	Intensity	0
AOBS (5)	Intensity	0

AOBS (6)	Intensity	0
AOBS (7)	Intensity	0
AOBS (0)	Intensity	0
AOBS (1)	Intensity	0
AOBS (2)	Intensity	0
AOBS (3)	Intensity	0
AOBS (4)	Intensity	0
AOBS (5)	Intensity	0
AOBS (6)	Intensity	0
AOBS (7)	Intensity	0
Constant Power Lambda Begin	ConstantPowerLambdaBegin	0
Constant Power Lambda End	ConstantPowerLambdaEnd	0
Constant Power Mode	ConstantPowerMode	0
AOTF (470)	Intensity	0.00
AOTF (471)	Intensity	0.00
AOTF (472)	Intensity	0.00
AOTF (473)	Intensity	0.00
AOTF (667)	Intensity	0.00
AOTF (668)	Intensity	0.00
AOTF (669)	Intensity	0.00
AOTF (670)	Intensity	0.00
AOTF (470)	CheckState	0.00
AOTF (471)	CheckState	0.00
AOTF (472)	CheckState	0.00
AOTF (473)	CheckState	0.00
AOTF (667)	CheckState	0.00
AOTF (668)	CheckState	0.00
AOTF (669)	CheckState	0.00
AOTF (670)	CheckState	0.00
AOTF (470)	UIVisibleState	1.00
AOTF (471)	UIVisibleState	0.00
AOTF (472)	UIVisibleState	0.00
AOTF (473)	UIVisibleState	0.00
AOTF (667)	UIVisibleState	0.00
AOTF (668)	UIVisibleState	0.00
AOTF (669)	UIVisibleState	0.00
AOTF (670)	UIVisibleState	0.00
AOTF (470)	Intensity	0.00
AOTF (471)	Intensity	0.00
AOTF (472)	Intensity	0.00
AOTF (473)	Intensity	0.00
AOTF (667)	Intensity	0.00
AOTF (668)	Intensity	0.00
AOTF (669)	Intensity	0.00

AOTF (670)	Intensity	0.00
AOTF (405)	Intensity	25.00
AOTF (405)	Intensity	0.00
AOTF (458)	Intensity	59.00
AOTF (476)	Intensity	0.00
AOTF (488)	Intensity	0.00
AOTF (496)	Intensity	0.00
AOTF (514)	Intensity	0.00
AOTF (458)	Intensity	0.00
AOTF (476)	Intensity	0.00
AOTF (488)	Intensity	0.00
AOTF (496)	Intensity	0.00
AOTF (514)	Intensity	0.00
PMT 1	State	Inactive
PMT 2	State	Active
PMT 2 (Offs.)	VideoOffset	-0.1
PMT 2 (HV)	HighVoltage	939.4
PMT 2 (HV_Unit)	HighVoltageUnit	V
PMT 2 (Preamp)	PreampMode	Direct
PMT 3	State	Inactive
PMT 4	State	Inactive
PMT Trans	State	Inactive
Galvo Slider	Filter	Galvo X Normal
Polarization FW	Filter	Empty 1
Reson. Galvo Pan	Filter	Galvo X Pan Center
Target Slider	Filter	Target Park
UV Lens FW	Filter	Lens 63x/1.30 GLYC
Hardware Type No.	Machine_Type	7
System Number	System_Number	5100001358
Laser (405 Diode, UV)	Power State	On
Laser (Argon, visible)	Power State	On
Laser (Argon, visible) (Power)	Output Power	25 %
Laser (WLL, WLL)	Power State	Off
TLD_Settings	TLD_Settings	100
RLD_Settings	RLD_Settings	-1
Scan Field Rotation	Scan Rotation	0
Rotation Direction	Rotation Direction	1
X Scan Actuator	ScanPlane	Active
X Scan Actuator (POS)	IsWholeRangeOfSuperZEnabled	0
X Scan Actuator (Gain)	Gain	5.00000476837613
X Scan Actuator (Offs.)	Offset	-1.84774134482507E-08
Y Scan Actuator	ScanPlane	Active
Y Scan Actuator (POS)	IsWholeRangeOfSuperZEnabled	0
Y Scan Actuator (Gain)	Gain	5.00000476837613
Y Scan Actuator (Offs.)	Offset	8.67361737988404E-19

Z Scan Actuator	ScanPlane	Inactive
Z Scan Actuator (POS)	IsWholeRangeOfSuperZEnabled	0
Z Scan Actuator (POS)	Position	0.000
Scan Speed	Speed	400
Phase	Phase	-34.346532387274
Y-Phase	Y-Phase	0
SMD-Phase	SMD-Phase	0
SP Mirror Channel 1 (left)	Wavelength	385.0
SP Mirror Channel 1 (right)	Wavelength	400.6
SP Mirror Channel 2 (left)	Wavelength	425.3
SP Mirror Channel 2 (right)	Wavelength	604.5
SP Mirror Channel 3 (left)	Wavelength	669.0
SP Mirror Channel 3 (right)	Wavelength	721.3
SP Mirror Channel 4 (left)	Wavelength	747.8
SP Mirror Channel 4 (right)	Wavelength	800.0
Magnification-Changer	Magnification	SCANx
Position	Position	1
Objective	Objective	HCX PL APO CS 63.0x1.30 GLYC 21°C UV
Order number (Obj.)	OrderNumber	11506194
Numerical aperture (Obj.)	NumericalAperture	1.30
Refraction index	RefractionIndex	1.45
DM6000 Stage XOrigin	XPosOrigin	0
DM6000 Stage YOrigin	YPosOrigin	0
DM6000 Stage ZOrigin	ZPosOrigin	0
DM6000 Stage Pos x	XPos	0.0238330444381
DM6000 Stage Pos y	YPos	0.02511813655357
Emission bandwidth PMT 2: begin - end	Bandwidth	425nm - 605nm
DM6000 Stage Pos z	ZPos	0

Time Stamps:

Frame (Show All)	**Relative Time (s)**	**Absolute Time (h:m:s.ms)**	**Date**
1	0	10:27:11 AM.387	10/14/2014
67	432.465	10:34:23 AM.852	10/14/2014

Image: **1.17_Z-Series-1**

Size: **20.97 MB**

File Location:
D:\users\Wolfram\Microbeads_14102014.lif

Start Time: **10/14/2014 10:04:39 AM.677**

End Time: **10/14/2014 10:08:06 AM.855**

Total Exposures: **80 (1 channels, 80 frames)**

Dimensions

Dimension	Logical Size	Physical Length	Physical Origin
X	512	49.21 µm	-28.30 µm
Y	512	49.21 µm	7.84 µm
Z	80	9.94 µm	4.88 µm

Scanner Settings

SuperContVisible Shutter	0
UV Shutter	1
Visible Shutter	0
ScanMode	xyz
Pinhole [m]	102.9 µm
Pinhole [airy]	1.00
Size-Width	49.2 µm
Size-Height	49.2 µm
Size-Depth	9.9 µm
StepSize	0.13 µm
Voxel-Width	96.3 nm
Voxel-Height	96.3 nm
Voxel-Depth	125.9 nm
Voxel-Volume	1167557.571 nm³
Zoom	5.0
Scan-Direction	1
SequentialMode	0
Frame-Accumulation	1
Frame-Average	1
Line-Average	2
Resolution	8 bits
Channels	1
Format-Width	512 pixels
Format-Height	512 pixels
Line-Accumulation	1
Sections	80

Scanner Settings Details (Show)

Hardware Settings

WLL AOTF (470)	0.00 %
WLL AOTF (471)	0.00 %
WLL AOTF (472)	0.00 %
WLL AOTF (473)	0.00 %
WLL AOTF (667)	0.00 %
WLL AOTF (668)	0.00 %
WLL AOTF (669)	0.00 %
WLL AOTF (670)	0.00 %
AOTF (405)	25.00 %
AOTF (458)	0.00 %
AOTF (476)	0.00 %
AOTF (488)	0.00 %
AOTF (496)	0.00 %
AOTF (514)	0.00 %
PMT 1	Inactive
PMT 2	Active
PMT 2 (Offs.)	0.0 %
PMT 2 (HV)	780.6
PMT 2 (HV_Unit)	V
PMT 2 (Preamp)	Direct
PMT 3	Inactive
PMT 4	Inactive
PMT Trans	Inactive
System Number	5100001358
Laser (405 Diode, UV)	On
Laser (Argon, visible)	On
Laser (Argon, visible) (Power)	25 %
Laser (WLL, WLL)	Off
Scan Field Rotation	0 degrees
Z Scan Actuator (POS)	0.000 µm
Scan Speed	400 Hz
Objective	HCX PL APO CS 63.0x1.30 GLYC 21°C UV
Numerical aperture (Obj.)	1.30
Refraction index	1.45
DM6000 Stage Pos x	0.00779222745569
DM6000 Stage Pos y	0.02373198003672
Emission bandwidth PMT 2: begin - end	423nm - 605nm

Hardware Settings Details (Hide)

AOBS (0)	Intensity	0
AOBS (1)	Intensity	0
AOBS (2)	Intensity	0
AOBS (3)	Intensity	0
AOBS (4)	Intensity	0
AOBS (5)	Intensity	0

AOBS (6)	Intensity	0
AOBS (7)	Intensity	0
AOBS (0)	Intensity	0
AOBS (1)	Intensity	0
AOBS (2)	Intensity	0
AOBS (3)	Intensity	0
AOBS (4)	Intensity	0
AOBS (5)	Intensity	0
AOBS (6)	Intensity	0
AOBS (7)	Intensity	0
Constant Power Lambda Begin	ConstantPowerLambdaBegin	0
Constant Power Lambda End	ConstantPowerLambdaEnd	0
Constant Power Mode	ConstantPowerMode	0
AOTF (470)	Intensity	0.00
AOTF (471)	Intensity	0.00
AOTF (472)	Intensity	0.00
AOTF (473)	Intensity	0.00
AOTF (667)	Intensity	0.00
AOTF (668)	Intensity	0.00
AOTF (669)	Intensity	0.00
AOTF (670)	Intensity	0.00
AOTF (470)	CheckState	0.00
AOTF (471)	CheckState	0.00
AOTF (472)	CheckState	0.00
AOTF (473)	CheckState	0.00
AOTF (667)	CheckState	0.00
AOTF (668)	CheckState	0.00
AOTF (669)	CheckState	0.00
AOTF (670)	CheckState	0.00
AOTF (470)	UIVisibleState	1.00
AOTF (471)	UIVisibleState	0.00
AOTF (472)	UIVisibleState	0.00
AOTF (473)	UIVisibleState	0.00
AOTF (667)	UIVisibleState	0.00
AOTF (668)	UIVisibleState	0.00
AOTF (669)	UIVisibleState	0.00
AOTF (670)	UIVisibleState	0.00
AOTF (470)	Intensity	0.00
AOTF (471)	Intensity	0.00
AOTF (472)	Intensity	0.00
AOTF (473)	Intensity	0.00
AOTF (667)	Intensity	0.00
AOTF (668)	Intensity	0.00
AOTF (669)	Intensity	0.00

AOTF (670)	Intensity	0.00
AOTF (405)	Intensity	25.00
AOTF (405)	Intensity	0.00
AOTF (458)	Intensity	0.00
AOTF (476)	Intensity	0.00
AOTF (488)	Intensity	0.00
AOTF (496)	Intensity	0.00
AOTF (514)	Intensity	0.00
AOTF (458)	Intensity	0.00
AOTF (476)	Intensity	0.00
AOTF (488)	Intensity	0.00
AOTF (496)	Intensity	0.00
AOTF (514)	Intensity	0.00
PMT 1	State	Inactive
PMT 2	State	Active
PMT 2 (Offs.)	VideoOffset	0.0
PMT 2 (HV)	HighVoltage	780.6
PMT 2 (HV_Unit)	HighVoltageUnit	V
PMT 2 (Preamp)	PreampMode	Direct
PMT 3	State	Inactive
PMT 4	State	Inactive
PMT Trans	State	Inactive
Galvo Slider	Filter	Galvo X Normal
Polarization FW	Filter	Empty 1
Reson. Galvo Pan	Filter	Galvo X Pan Center
Target Slider	Filter	Target Park
UV Lens FW	Filter	Lens 63x/1.30 GLYC
Hardware Type No.	Machine_Type	7
System Number	System_Number	5100001358
Laser (405 Diode, UV)	Power State	On
Laser (Argon, visible)	Power State	On
Laser (Argon, visible) (Power)	Output Power	25 %
Laser (WLL, WLL)	Power State	Off
TLD_Settings	TLD_Settings	100
RLD_Settings	RLD_Settings	-1
Scan Field Rotation	Scan Rotation	0
Rotation Direction	Rotation Direction	1
X Scan Actuator	ScanPlane	Active
X Scan Actuator (POS)	IsWholeRangeOfSuperZEnabled	0
X Scan Actuator (Gain)	Gain	5.00000476837613
X Scan Actuator (Offs.)	Offset	-1.78262693983039E-03
Y Scan Actuator	ScanPlane	Active
Y Scan Actuator (POS)	IsWholeRangeOfSuperZEnabled	0
Y Scan Actuator (Gain)	Gain	5.00000476837613
Y Scan Actuator (Offs.)	Offset	4.93901261470897E-04

Z Scan Actuator	ScanPlane	Inactive
Z Scan Actuator (POS)	IsWholeRangeOfSuperZEnabled	0
Z Scan Actuator (POS)	Position	0.000
Scan Speed	Speed	400
Phase	Phase	-34.346532387274
Y-Phase	Y-Phase	0
SMD-Phase	SMD-Phase	0
SP Mirror Channel 1 (left)	Wavelength	385.0
SP Mirror Channel 1 (right)	Wavelength	400.6
SP Mirror Channel 2 (left)	Wavelength	423.0
SP Mirror Channel 2 (right)	Wavelength	604.5
SP Mirror Channel 3 (left)	Wavelength	669.0
SP Mirror Channel 3 (right)	Wavelength	721.3
SP Mirror Channel 4 (left)	Wavelength	747.8
SP Mirror Channel 4 (right)	Wavelength	800.0
Magnification-Changer	Magnification	SCANx
Position	Position	1
Objective	Objective	HCX PL APO CS 63.0x1.30 GLYC 21°C UV
Order number (Obj.)	OrderNumber	11506194
Numerical aperture (Obj.)	NumericalAperture	1.30
Refraction index	RefractionIndex	1.45
DM6000 Stage XOrigin	XPosOrigin	0
DM6000 Stage YOrigin	YPosOrigin	0
DM6000 Stage ZOrigin	ZPosOrigin	0
DM6000 Stage Pos x	XPos	0.00779222745569
DM6000 Stage Pos y	YPos	0.02373198003672
Emission bandwidth PMT 2: begin - end	Bandwidth	423nm - 605nm
DM6000 Stage Pos z	ZPos	0

Time Stamps:

Frame (Show All)	**Relative Time (s)**	**Absolute Time (h:m:s.ms)**	**Date**
1	0	10:04:39 AM.677	10/14/2014
80	207.178	10:08:06 AM.855	10/14/2014

B Patent

Patent application

Způsob pořizování mikroskopických snímků a jejich následného zpracování a zařízení k provádění tohoto způsobu

Oblast techniky

Vynález se týká vytváření detailního mikroskopického obrazu pomocí snímků mikroskopovaného vzorku a následného zpracování snímků s vysokou mírou odlišitelnosti objektů při daném zvětšení a zařízení k provádění tohoto způsobu.

Dosavadní stav techniky

V současné mikroskopii se využívá několik principiálně odlišných mikroskopů. Mezi nejznámější typové kategorie patří optické mikroskopy a elektronové mikroskopy.

Elektronové mikroskopy dosahují velmi vysokého zvětšení, neboť používají k promítání obrazu elektrony, jenž vykazují při svém šíření prostorem menší vlnovou délku a proto vyšší rozlišení při zvětšení obrazu, nežli fotony viditelného světla. Nevýhody elektronových mikroskopů spočívají v tom, že jsou konstrukčně velmi složité a jejich výroba a provoz vyžaduje vysoké investice finančních prostředků. Vzorky pro mikroskopování se musejí velice precizně, pracně a zdlouhavě připravovat, přičemž pro některé vědecké metody a typy vzorků je tento přístup nevyhovující, například v biologických aplikacích dojde k nevratné modifikaci vzorku.

Současné optické mikroskopy používají světelné paprsky k zobrazování mikroskopovaného vzorku. Principiální skladba optického mikroskopu zahrnuje optickou část a mechanickou část. V mechanické části je zahrnut ochranný kryt (tubus) pro optické prostředky optické části mikroskopu a polohovatelný stolek pro nesení mikroskopovaného vzorku. V dnešní době dosahuji polohovatelné stolky velmi jemného posunu v řádech desítek nanometrů po směru hlavních os (X, Y, Z) kartézské souřadnicové soustavy.

Optická část mikroskopu zahrnuje alespoň jednu čočku objektivu. Čočka použitá ke zvětšení pozorovaného vzorku se také někdy nazývá přímo objektiv. V optické ose se nachází vzorek umístěný na stolku ozařovaný bílým světlem (bílé světlo je světelný svazek kombinující

světelné paprsky různých vlnových délek), a objektiv. Světlo se šíří přes vzorek k objektivu, který přenáší obraz vzorku, případně dále k okuláru, jenž zprostředkuje zvětšený obraz lidskému oku, či snímači obrazu. V průběhu desetiletí se optické mikroskopy zdokonalovaly tak, aby dosahovaly nejvyššího možného zvětšení při zachování rozlišitelnosti obrazu.

Nevýhody optických mikroskopů spočívají v tom, že ačkoliv bylo vynaloženo úsilí pro získání největšího zvětšení s dostatečným rozlišením v podobě soustav dokonalých optických čoček, v podobě vyladěných světelných zdrojů, v podobě úprav mechanické části optických mikroskopů a dalších technických úprav, je tento způsob vytváření zvětšeného obrazu limitován fyzikálními zákony.

V roce 1873 Ernst Karl Abbé stanovil, že maximální limit dosažitelného rozlišení pomocí optického mikroskopu je určen vztahem $d = \lambda/2n \sin\alpha$, kde λ je vlnová délka použitého světla, n je index lomu čočky a α je polovina vrcholového úhlu kužele paprsků vstupujících do čočky objektivu. Tento vztah vztažen na bílé světlo znamená maximální možné rozlišení d = cca 200 nm.

V nedávné době došlo k prolomení Abbého difrakčního limitu modifikováním postupu optického mikroskopování a úpravou parametrů mikroskopů a mikroskopie. Bylo vyvinuto tzv. fluorescenční mikroskopování vysokého rozlišení. V mnoha případech musí být do vzorku vpraveny fluorescenční látky, které po dopadu světla emitují fotony a které umožňují použití metod překonávajících difrakční limit. Mezi známé způsoby fluorescenčního mikroskopování lze zařadit např. způsob z přihlášky vynálezu JP2014202514 (A).

Nevýhody fluorescenčních mikroskopů tedy spočívají v tom, že vpravení fluorescenčního prostředku do sledovaného vzorku jej vždy modifikuje. Je-li vzorek tvořen např. živou buňkou, má modifikace vliv na fyziologický stav buňky, její přirozené reakce, atp. Jinými slovy, není sledován již původní vzorek, ale vzorek jiný, chemicky nebo molekulárně-biologicky pozměněný, včetně jeho optických vlastností.

Jsou známy i další způsoby mikroskopie pracující na principu úpravy parametrů procházejícího světla optickou soustavou např. fázový posun světelných paprsků, holografie, atp. Nevýhoda těchto mikroskopů spočívá v tom, že provedené úpravy parametrů světla

použitého pro mikroskopování současně způsobují vznik artefaktů v digitálním obraze vzorku, které se musejí pracně odstraňovat pomocí softwarových modulů obsahujících program s náročnými matematickými a analyzačními operacemi. V mnoha případech je informace o vzorku nesená fotony natolik pozměněna, že ji nelze žádným způsobem získat zpět.

Ve vynálezu popisovaná metoda analýzy získaného signálu na digitální kameře se soustředí na maximální vytěžení informace a identifikaci všech topologicky odlišitelných objektů. Tato metoda je principiálně jiná a podobá se více způsobu analýzy objektů prostřednictvím lidského vnímání tak, jak je například vnímána informace při mikroskopii s videozesílením. Mikroskopie s videozesílením též umožňuje odlišit objekty mnohem menší, než předpokládá Abbého difrakční limit, lze i zjednodušeně říci, že jej překonává.

Úkolem vynálezu je vytvoření způsobu pořizování snímků mikroskopovaného vzorku pomocí mikroskopu s jejich následným zpracováním, který by umožňoval využívání známých druhů mikroskopů a který by vedl k vytvoření obrazů a modelů uspořádání objektů uvnitř mikroskopovaného vzorku ve vysokém rozlišení s rozpoznatelností vnitřních struktur objektů, přičemž by nebyl ovlivněn stav sledovaného objektu značícím agentem.

Zařízení využívající způsob podle vynálezu by měla být jednoduše zkompletovatelná a snadno rozšiřitelná do laboratoří a pracovišť široké škály vědních oborů.

Podstata vynálezu

Vytčený úkol je vyřešen vytvořením způsobu pořizování snímků mikroskopem v procházejícím elektromagnetickém vlnění, vybaveného alespoň jednou čočkou a záznamovým zařízením snímků mikroskopovaného vzorku a jejich následného zpracování pro vytvoření trojrozměrného modelu alespoň části mikroskopovaného vzorku tvořeného alespoň jedním objektem zájmu včetně jeho struktury podle tohoto vynálezu.

Při provádění způsobu pořizování snímků z mikroskopu v procházejícím elektromagnetickém vlnění, který je vybaven alespoň jednou čočkou a zařízením pro záznam snímku mikroskopovaného vzorku, a při jejich následném zpracování se nejprve vloží

mikroskopovaný vzorek na polohovatelný stolek mikroskopu. Následně se polohovatelný stolek se vzorkem nastaví do optické osy čoček mikroskopu a poté se vzorek osvítí elektromagnetickým vlněním. Současně se vytvoří digitální záznam alespoň dvou snímků mikroskopovaného vzorku a poté se pořízené snímky mikroskopovaného vzorku datově zpracují.

Podstata vynálezu spočívá v tom, že se v průběhu provádění způsobu provedou následující kroky:

(a) nejprve se nalezne rozsah ohniskových rovin čoček, ve kterém se nachází alespoň jeden objekt zájmu vzorku v rovině ostrosti,

(b) se pořídí alespoň dva odlišné digitální snímky mikroskopovaného vzorku v obrazovém formátu s minimálním zpracováním dat v nejvyšším dostupném digitálním pixelovém rozlišení odpovídajícím rozmístění a počtu aktivních záznamových prvků záznamového zařízení, snímky se systematicky odlišují polohou vzorku od záznamového zařízení, nebo časem pořízení v případě časosběrné mikroskopie,

(c) digitální snímky mikroskopovaného vzorku se podle možnosti technického uspořádání rozdělí na spektrální složky, rozdělené snímky se uspořádají do formy datové 3D matice s respektováním pořadí jejich pořízení a datová 3D matice se analyzuje po jednotlivých pixelech v jednotlivých po sobě jdoucích úrovních datové 3D matice odpovídajících pořadí digitálních snímků zařazených do datové 3D matice,

(d) naleznou se pixely v rámci přesnosti měření neměnné intenzity pro soubor digitálních snímků mikroskopovaného vzorku uspořádaných v datové 3D matici,

(e) vytvoří se referenční histogram intenzit spektrálních složek alespoň části pozadí kolem objektu zájmu,

(f) pozice alespoň jednoho objektu zájmu je nalezena pomocí detekce pixelů neměnné intenzity mezi alespoň dvěma po sobě jdoucími digitálními snímky mikroskopovaného vzorku a porovnají se hodnoty intenzit celého řezu 3D datovou maticí s alespoň jednou hodnotou intenzit histogramu pozadí,

(f) během porovnání je analyzována a klasifikována i vnitřní struktura objektu zájmu, přičemž rozptylující, absorbující a destruktivně interferenční

podobjekty zájmu jsou složeny z pixelů tmavších než referenční hodnota, nebo rozsah hodnot, definující pozadí kolem objektu zájmu a (auto)fluoreskující podobjekty a podobjekty vzniklé pozitivní interferencí elektromagnetického vlnění se skládají z pixelů světlejších než je uvedená referenční hodnota,

(g) na závěr se vytvoří model trojrozměrné struktury objektu zájmu.

Výhodné je, že se vytvoří model struktury objektu zájmu, který obsahuje odlišitelné detaily menší, nežli limit udaný Abbého rovnicí. Objekt zájmu byl nasnímán na základě mikroskopování procházejícím elektromagnetickým vlněním. Způsob využívá dostupná zařízení, která díky zpracování digitálních snímků vedou k detekci a třídění neznačených difraktujících, autofluoreskujících podobjektů velikosti 1 voxelu. Tím je možné postihnout dynamiku uvnitř buňky a rekonstruovat její model. Buňka nemusí být nijak ovlivněna značícími agenty nebo jinými chemikáliemi. Využití barvících technik se ale nevylučuje a způsob analýzy snímků je dokáže odlišit.

Ve výhodném provedení způsobu podle vynálezu je elektromagnetické vlnění tvořeno okem viditelným spektrem, nebo ultrafialovým spektrem, nebo infračerveným spektrem, mikroskop je optický mikroskop, záznamové zařízení je tvořeno digitální kamerou. Vynález ale není omezen pouze na tyto vlnové délky, lze použít elektromagnetické vlnění jiné vlnové délky zvolené pro konkrétní druh mikroskopovaného vzorku a aplikaci. Elektromagnetické vlnění nacházející se v oku viditelném spektru, tzv. bílé světlo, je velice snadno použitelné a bezpečné. Optické mikroskopy na procházející bílé světlo jsou snadno dostupné a rozšířené na pracovištích celého světa. Digitální kamery a jiné digitální detektory zaznamenávající rozložení intenzity elektromagnetického vlnění v rovině a převádějícího jej do digitální formy jsou rovněž dostupné v mnoha typech a provedeních. V jiných aplikacích použití způsobu v průběhu mikroskopování může být výhodné použít ultrafialové, infračervené nebo jiné spektrum.

V dalším výhodném provedení způsobu podle vynálezu je hodnota intenzity procházejícího elektromagnetického vlnění nastavitelná. Díky nastavitelné intenzitě, lze způsob naprosto přesně přizpůsobit typu mikroskopovaného vzorku, čímž je udržena vysoká míra rozlišení výsledků mikroskopování.

V dalším výhodném provedení způsobu podle vynálezu se pro skenování biologických a jiných na elektromagnetické vlnění citlivých vzorků v průběhu polohování stolku se vzorkem a v průběhu mikroskopování elektromagnetické vlnění kontrolovaně rozsvěcuje a zhasíná pro snížení jeho negativního vlivu na vzorek, snímání kamery se synchronizuje s kontrolovaným blikáním elektromagnetického vlnění. Dopadající elektromagnetické vlnění má degradabilní vliv na mikroskopovaný vzorek, zejména u biologických vzorků a dalších vzorků obsahujících organické molekuly. Zároveň je ale odlišitelnost objektů závislá na intenzitě elektromagnetického vlnění a maximální odlišitelnosti je dosaženo při jeho poměrně vysokých intenzitách. Intenzita elektromagnetického vlnění má tedy vliv nejenom na mikroskopovaný vzorek, ale i na datovou informaci obsaženou v digitálních snímcích zpracovávaných způsobem výše uvedeným. Aby byla životnost vzorku prodloužena a zároveň dosaženo maxima odlišitelnosti objektů, je vzorek ozařován pouze v intervalech při prvním polohování stolku, nebo při pořizování snímků.

Součástí vynálezu je rovněž zařízení, které umožňuje provádění způsobu pořizování a zpracování snímku z mikroskopu s procházejícím elektromagnetickým vlněním.

Zařízení pro pořizování snímků mikroskopem v procházejícím elektromagnetickém vlnění a jejich následné zpracování zahrnuje alespoň jeden polohovací stolek polohovatelný ve směru os (X, Y, Z) kartézských souřadnic. Dále alespoň jeden mikroskop sestávající se ze zdroje elektromagnetického vlnění, alespoň z jedné čočky objektivu a alespoň z jedné kamery pro záznam digitálních snímků.

Podstata vynálezu spočívá v tom, že zařízení je opatřeno řídící jednotkou pro nastavení polohy stolku, pro ovládání zdroje elektromagnetické vlnění, pro ovládání funkce kamery a pro ukládání pořízených mikroskopických snímků, která zahrnuje alespoň jedno datové úložiště, ve kterém je uložen alespoň jeden softwarový modul pro řízení funkce zařízení a zpracování pořízených snímků.

Je využito známého mikroskopu, který je ovládán řídící jednotkou pro provádění způsobu podle vynálezu. Řídící jednotka je uzpůsobena k synchronizaci práce jednotlivých součástí zařízení.

Čočka objektivu vykazuje pokud možno co nejmenší zkreslení optické dráhy pro všechny pozorované objekty studovaného vzorku. V případě mikroskopie ve viditelném záření to tedy není nezbytně tzv. plně apochromatický objektiv, s výhodou lze použít například reflektorovou optiku, která minimalizuje barevnou vadu.

V dalším výhodném provedení zařízení podle vynálezu obsahuje softwarový modul pro řízení funkce zařízení a zpracování pořízených snímků alespoň jeden softwarový program pro zpracování pořízených snímků, pro synchronizaci polohování stolku s nastavováním a rozsvěcováním zdroje elektromagnetického vlnění a spouštěním kamery. Softwarový program pro pořizování a zpracování snímků mikroskopovaného vzorku podle tohoto vynálezu zahrnuje algoritmy pro

- nastavování a krokovou změnu polohy polohovatelného stolku,
- nastavování intenzity elektromagnetické vlnění emitovaného zdrojem elektromagnetického vlnění,
- pro řízené rozsvěcování a zhasínání zdroje elektromagnetické vlnění,
- pro synchronizaci polohování stolku, blikání elektromagnetického vlnění, spouštění kamery a pořízení snímku,
- pro zpracování série snímků mikroskopovaného vzorku,
- pro vytvoření 3D obrazu struktury objektu zájmu.

Je výhodné, že zařízení je složeno ze standardního mikroskopu s procházejícím elektromagnetickým vlněním odpovídajícím použité optice. Tyto mikroskopy jsou na pracovištích velmi rozšířené a jsou snadno dostupné.

Pro případ mikroskopie ve viditelné oblasti jsou digitální kamery a polohovatelné stolky rovněž při současném stavu techniky velmi dobře dostupné. Výhoda zařízení spočívá v jeho mimořádné jednoduchosti a dostupnosti, kdy jsou výše uvedené běžně dostupné části řízeny řídící jednotkou tvořenou například počítačem. Počítač, díky svému programu s uloženým způsobem práce, synchronizuje práci jednotlivých součástí zařízení a díky digitálnímu způsobu zpracování snímků je schopen připravit výstup s trojrozměrným modelem objektu zájmu včetně jeho vnitřní struktury s miniaturními podobjekty. Model obsahuje pro optické mikroskopy s procházejícím světlem odlišitelné struktury tak daleko za limitní hranicí Abbého difrakčního limitu, jaký je poměr této teoreticky vypočtené hodnoty k velikosti

objektu projektovaného na jeden bod čipu digitální kamery. Jinými slovy v trojrozměrném obraze je pro topologicky odlišitelné objekty dosaženo stejné odlišitelnosti jako při dvourozměrném pozorování pomocí mikroskopie s videozesílením.

Objasnění výkresů

Uvedený vynález bude blíže objasněn na následujících vyobrazeních, kde:

obr. 1 znázorňuje schéma zařízení a jeho funkce podle vynálezu,
obr. 2 znázorňuje schéma funkce způsobu zpracování snímků mikroskopovaného vzorku,
obr. 3 znázorňuje schéma způsobu segmentace podobjektů.

Příklad uskutečnění vynálezu

Rozumí se, že dále popsané a zobrazené konkrétní případy uskutečnění vynálezu jsou představovány pro ilustraci, nikoliv jako omezení vynálezu na uvedené příklady. Odborníci znalí stavu techniky najdou nebo budou schopni zajistit za použití rutinního experimentování větší či menší počet ekvivalentů ke specifickým uskutečněním vynálezu, která jsou zde popsána. I tyto ekvivalenty budou zahrnuty v rozsahu následujících patentových nároků.

Vlastní matematické zpracování je využitelné prakticky ve všech případech, kdy je mikroskopem pozorován vzorek obsahující obrazové roviny alespoň na dvou krocích posunu stolku v ose shodné s optickou osou mikroskopu. Optická osa se shoduje se svislou osou Z podle kartézského souřadnicového systému (X, Y, Z). Zároveň matematické zpracování snímků mikroskopovaného vzorku není omezeno na mikroskopii v procházejícím bílém světle, lze je použít ve všech případech, kdy je zobrazení dosaženo rozptylem jakýchkoliv vln na prostorovém vzorku, nebo jakýmkoliv jiným postupem, při němž vzniká dvourozměrná mapa signálu, kterou je možno reprodukovatelně systematicky měnit. Matematicky, z hlediska matematické topologie, není omezen ani počet rozměrů signálu. V uvedeném příkladu je prostor detekce fakticky 3 x N rozměrný. To znamená 3(X, Y, Z) x 3(N =počet kanálů – vybrané barvy viditelného spektra světla, pro příklad provedení právě 3 = zelená, červená, modrá).

Na obr. 1 je znázorněno schéma pracovního postupu zařízení **1**, při kterém se provádí záznam sady snímků mikroskopovaného vzorku **2** z optického mikroskopu **3** a jejich zpracování dle způsobu tohoto vynálezu. Z řídící jednotky **4** jsou odesílány pokyny ke zdroji **5** elektromagnetického vlnění, který emituje tzv. bílé světlo = světlo ve viditelném spektru vlnových délek kombinující vlnové délky několika barev. Mezi pokyny je nejenom informace o intenzitě emitovaného světla, ale i pokyn ke svícení, či zhasnutí. Dále je řídící jednotkou **4** polohován polohovatelný stolek **6**, který nese mikroskopovaný vzorek **2**. Řídící jednotka **4** polohuje stolek **6** ve směru os X, Y, Z kartézské souřadnicové soustavy. Nejprve se stolek **6** nastaví tak, aby vzorek **2** ležel v optické ose mikroskopu **3**. V průběhu nastavování pozice stolku **6** je ze světelného zdroje **5** blikáno, aby nebyl vzorek **2** exponován ve světle po dobu větší, než nezbytně nutnou, přičemž každý moment osvícení zaznamená digitální kamera **8** za čočkou **7** objektivu a svá data odešle do řídící jednotky **4**.

Jakmile je vzorek **2** na svém místě v optické ose mikroskopu **3**, najde se rozsah ohniskových rovin čočky **7** objektivu takový, že v něm je alespoň jeden objekt zájmu v rovině ostrosti. V rámci tohoto rozsahu se v tomto konkrétním příkladu provedení vzdálenost mezi polohovatelným stolkem **6** a čočkou **7** ve směru vertikální osy (rovnoběžné s optickou osou mikroskopu) mění o definované malé úseky o velikosti v řádu desítek až 150 nm, přičemž se v každé změněné vzdálenosti pořídí alespoň jeden digitální snímek mikroskopovaného vzorku **2**.

Snímky jsou přeneseny do řídící jednotky **4**, kde jsou uloženy na datovém úložišti **9** a odtud je posléze soubor dat nahrán pro zpracování snímků a v nich se nacházejících dat. Zpracování je provedeno buď v řídící jednotce **4**, nebo v nevyobrazeném externím zařízení s dostatečným výpočetním výkonem.

Mikroskopování je realizováno pomocí zařízení **1**, které zahrnuje optický mikroskop **3** v procházejícím světle. Optický mikroskop **3** má zdroj **5** bílého světla pro ozařování vzorku **2** umístěného na polohovatelném stolku **6**. Dále čočku **7** objektivu a čočku okuláru. V ohnisku okuláru je umístěna digitální kamera **8**. Polohovatelný stolek **6** je ovládán krokovými motory, které jsou řízeny z řídící jednotky **4**. Řídící jednotka **4** je připojena ke všem součástem optického mikroskopu **3**. Na rozdíl od běžného přístupu je kladen důraz na co nejjednodušší

optickou dráhu a co nejmenší zkreslení čočkou. Z dalších optických prvků se použijí pouze případně hranové filtry odstraňující světlo v ultrafialové a infračervené oblasti.

Řídicí jednotka **4** je tvořena počítačem, který má ve svém datovém úložišti **9** softwarový modul obsahující program pro nastavení mikroskopu **3**, zejména nastavení pozice stolku **6** se vzorkem **2** do optické osy a nastavení funkce zdroje **5** světla. Počítač umožňuje zpracování snímků a vytvoření modelu **10** objektu zájmu včetně jeho vnitřní struktury zahrnující podobjekty dle níže uvedeného způsobu.

Na obr. 2 je schematicky vyobrazen způsob zpracování snímků. V rámci způsobu je vykonána řada operací, které vedou k získání trojrozměrného modelu **10** konkrétního objektu zájmu, včetně jeho struktury. Pokud bude zkoumán biologický vzorek **2**, lze si pro lepší představu propojit termín vzorek **2** s termínem tkáň, termín objekt zájmu s termínem buňka, termín podobjekt s termínem organela.

Krok **A1** zahrnuje převzetí snímků v nepozměněné podobě, tak jak byly snímacím čipem zdigitalizovány (v RAW formátu), tedy podle možností současné kamerové technologie v 8, 12 nebo v 16 bitové matici původního digitalizovaného signálu. Důležité je, že žádný ze snímků není nijak komprimován a upravován jinými interpolačními metodami. V případě použití běžné barevné digitální kamery **8**, která je opatřena Bayerovým filtrem, se dopadající elektromagnetické vlnění zaznamenává na mřížku aktivních prvků na čipu (pixelů) citlivých ve třech různých spektrálních rozsazích odpovídajících částečně třem základním barvám vnímaného viditelného elektromagnetického vlnění (zelená, červená a modrá). Pixelů pro záznam zelené barvy je na snímači dvakrát více, nežli pixelů pro každou ze dvou zbývajících barev. V jiném příkladu provedení je možná kombinace šedotónové kamery s použitím barevných filtrů, nebo světelných laserů, při snímání vzorků. Výstupem musí být digitální snímek v nepozměněném formátu digitálního zápisu.

V kroku **A1** je snímek rozdělen na barevné složky. Následně se stejný krok **A1** udělá pro sousedící snímek, který je k předcházejícímu snímku zařazen do datové 3D matice. Snímky se zařadí v matici pod sebe, aby bylo eliminováno nežádoucí posunutí, či chvění, následně se analyzují, pixel po pixelu, přičemž se porovnají a naleznou se pixely s intenzitou, která se v rámci digitálního rozlišení nezmění. Přesnost provedení je dána bitovou hloubkou kamery,

šumem kamery a správným zarovnáním snímků v sérii ve směru optické osy. Tyto zdánlivě neměnné pixely slouží k určení pozice objektu zájmu, přičemž se u něj interakce se světlem a následná zobrazovací funkce nezmění v rámci daného kroku v ose posunu stolku **6** ve vertikální ose. Pixely zobrazující pozadí objektu zájmu se vyloučí a ponechají se pro jinou část analýzy. Toto se provede pro všechny barevné varianty jednoho snímku a dále pak pro celou sérii snímků, které byly zařazeny do datové 3D matice.

Po uskutečnění kroku **A1** je známá pozice objektu zájmu na všech pořízených snímcích v sadě dle pohybu ve směru vertikální osy. Objekty zájmu se promítnou do sebe pro získání konkrétního 2D modelu objektu zájmu. Tento krok je označen na obr. 2 jako krok **B**. V průběhu kroku **B** se vytvoří 2D model objektu zájmu kombinací dat všech známých pozic objektu zájmu získaných výpočtem informace nesené v každém snímku.

Následuje krok **C1**, při kterém se může i dále redukovat rozsah ohniskových rovin využívaných pro konstrukci 2D modelu objektu zájmu.

V kroku **D** se na řezy ohniskovou oblastí aplikuje metoda vyhodnocení rozdílu světelných intenzit v po sobě jdoucích snímcích pro vytvoření vnitřní struktury modelu objektu zájmu. Současně jsou s krokem **D** provedeny kroky **A2**, **C3** a **E3**, při kterých se vytvoří histogramy kolem pozadí ohniskové oblasti objektu zájmu na snímcích. Tyto informace o pozadí objektů zájmu jsou vybrány pro konkrétní ohniskové roviny. Tím dojde k rozdělení zobrazení podobjektů podle intenzit na zobrazení podobjektů difraktujících, podobjektů fluoreskujících (ať již autofluorescence nebo fluorescence vnesená uměle) a zdánlivých podobjektů vzniklých produktivním skládáním světelných vln.

Další na řadu přicházejí kroky **E1** a **E2**, které vedou k vyznačení jednotlivých podobjektů vnitřní struktury objektu zájmu. Podobjekty jsou zkombinovány z informací o pozadí objektu zájmu, z informací rozdílů světelných intenzit mezi pixely sousedících snímků a to z informací pro celou zaostřenou sérii snímků ve směru vertikální osy.

Na obr. 3 je vyobrazeno detailní schéma algoritmu z obr. 2 v krocích **D** a **E3**, včetně třídění podobjektů. V kroku **A1‘** je snímek objektu zájmu rekonstruován do barevné podoby. V kroku **A2‘** jsou klasifikovány podobjekty na základě porovnání histogramu světelné

intensity objektu zájmu s histogramem pozadí snímku na difraktující a autofluoreskující podobjekty. Podobjekty vzniklé konstruktivním skládáním světelných vln není v rámci popisované metody možné odlišit od objektů autofluoreskujících a je nutno použít buď ruční třídění, nebo složitější metody filtrace. Současně je v průběhu kroku **B‘** vytvořena binární maska pomocí překrývajících se pixelů dvou po sobě jdoucích snímků.

V kroku **C‘** se oddělí jednotlivé difraktující podobjekty. Poté je v kroku **D‘** zrekonstruován trojrozměrný model podobjektů rozmístěných v prostoru.

Průmyslová využitelnost

Způsob pořizování snímků mikroskopem v procházejícím elektromagnetickém vlnění a jejich následného zpracování podle vynálezu je vhodný pro univerzální použití prakticky ve všech laboratořích zabývajících se sledováním mikroskopických objektů. Například v laboratořích zabývajících se fyziologickým a morfologickým stavem buněk a vývojem buněk a tkání, rovněž je vhodný pro použití v materiálovém inženýrství, zejména při studiu optických vlastností transparentních materiálů, hodnocení kvality mikro- a nano- granulí apod.

Přehled vztahových značek

1 zařízení pro mikroskopování v procházejícím světle a vyhodnocení snímků
2 mikroskopovaný vzorek
3 mikroskop
4 řídící jednotka
5 zdroj elektromagnetického vlnění
6 polohovatelný stolek
7 čočka objektivu
8 záznamové zařízení/digitální kamera
9 datové úložiště
10 trojrozměrný model objektu zájmu

A1 převzetí snímku v digitální podobě bez jakékoliv úpravy dat formátu uložení snímku, vyloučení pozadí, nalezení pozice objektu zájmu
B kombinace pozic objektu zájmu na snímcích, do konečného modelu
C1 redukce ohniskových rovin pro konstrukci konečného modelu
D použití metody vyhodnocení rozdílů světelných intenzit v po sobě jdoucích snímcích
A2 vytvoření histogramů z pozadí okolo objektu zájmu každého snímku
C3 výběr pro konkrétní ohniskové roviny
E1, E2, E3 vytvoření modelu objektu zájmu s podobjekty ve vnitřní struktuře
A1‘ rekonstrukce objektu zájmu do barevné podoby
A2‘ klasifikace podobjektů
B‘ vytvoření binární masky z překrývajících se pixelů dvou po sobě jdoucích snímků
C odstranění difraktujících podobjektů
D‘ rekonstrukce 3D modelu objektu zájmu s vnitřní strukturou

PATENTOVÉ NÁROKY

1. Způsob pořizování snímků mikroskopem (3) v procházejícím elektromagnetickém vlnění, vybaveným alespoň jednou čočkou (7) a záznamovým zařízením (8) pro záznam snímků mikroskopovaného vzorku (2), a jejich následného zpracování, při kterém se nejprve vloží mikroskopovaný vzorek (2) na polohovatelný stolek (6) mikroskopu (3), polohovatelný stolek (6) se vzorkem (2) se nastaví do osy procházejícího vlnění směřujícího do čočky (7) mikroskopu (3), následně se vzorek (2) ozáří, přičemž se vytvoří digitální záznam alespoň jednoho snímku mikroskopovaného vzorku (2) záznamovým zařízením (8), a poté se pořízený snímek mikroskopovaného vzorku (2) zpracuje, **v y z n a č u j í c í s e t í m**, že

   (a) nejprve se nalezne rozsah ohniskových rovin čočky (7), ve kterém se nachází alespoň jeden objekt zájmu vzorku (2) v rovině ostrosti,

   (b) pořídí se alespoň dva odlišné digitální snímky mikroskopovaného vzorku (2) v obrazovém formátu s minimálním zpracováním dat v nejvyšším dostupném digitálním pixelovém rozlišení odpovídajícím rozmístění a počtu aktivních záznamových prvků záznamového zařízení (8), snímky se systematicky odlišují polohou vzorku (2) od záznamového zařízení (8), nebo časem pořízení v případě časosběrné mikroskopie,

   (c) digitální snímky mikroskopovaného vzorku (2) se rozdělí na spektrální složky, rozdělené snímky se uspořádají do formy datové 3D matice s respektováním pořadí jejich pořízení a datová 3D matice se analyzuje po jednotlivých pixelech v jednotlivých po sobě jdoucích úrovních datové 3D matice odpovídajících pořadí digitálních snímků zařazených do datové 3D matice,

   (d) naleznou se pixely v rámci přesnosti měření neměnné intenzity pro soubor digitálních snímků mikroskopovaného vzorku (2) uspořádaných v datové 3D matici,

   (e) vytvoří se referenční histogram intenzit spektrálních složek alespoň části pozadí kolem objektu zájmu,

   (f) pozice alespoň jednoho objektu zájmu je nalezena pomocí detekce pixelů neměnné intenzity mezi alespoň dvěma po sobě jdoucími digitálními snímky

mikroskopovaného vzorku (2) a porovnají se hodnoty intenzit celého řezu 3D datovou maticí s alespoň jednou hodnotou intenzit histogramu pozadí,

(f) během porovnání je analyzována a klasifikována i vnitřní struktura objektu zájmu, přičemž rozptylující, absorbující a destruktivně interferenční podobjekty zájmu jsou složeny z pixelů tmavších než referenční hodnota, nebo rozsah hodnot, definující pozadí kolem objektu zájmu a (auto)fluoreskující podobjekty a objekty vzniklé pozitivní interferencí elektromagnetického vlnění se skládají z pixelů světlejších než je uvedená referenční hodnota,

(g) na závěr se vytvoří model (10) trojrozměrné struktury objektu zájmu.

2. Způsob podle nároku 1, **v y z n a č u j í c í s e t í m**, že elektromagnetické vlnění je tvořeno okem viditelným spektrem, nebo ultrafialovým spektrem, nebo infračerveným spektrem, nebo elektromagnetickým zářením jiné vlnové délky, mikroskop (3) je optický mikroskop nebo jiný mikroskop vytvářející obraz pomocí elektromagnetického vlnění, záznamové zařízení (8) je tvořeno digitální kamerou nebo jiným zařízením zaznamenávajícím rozložení intenzity elektromagnetického vlnění v rovině a převádějícího jej do digitální formy.

3. Způsob podle nároku 2, **v y z n a č u j í c í s e t í m**, že hodnota intenzity procházejícího elektromagnetického vlnění je nastavitelná.

4. Způsob podle nároku 2 nebo 3, **v y z n a č u j í c í s e t í m**, že pro skenování biologických a jiných na elektromagnetické vlnění citlivých vzorků (2) se v průběhu polohování stolku (6) se vzorkem (2) a v průběhu mikroskopování elektromagnetické vlnění kontrolovaně rozsvěcuje a zhasíná pro snížení jeho negativního vlivu na vzorek (2), snímání záznamového zařízení (8) se synchronizuje s kontrolovaným blikáním elektromagnetického vlnění.

5. Zařízení pro pořizování snímků z mikroskopu v procházejícím elektromagnetickém vlnění a jejich následné zpracování zahrnuje alespoň jeden polohovací stolek (6) polohovatelný ve směru os (X, Y, Z) kartézských souřadnic nebo jiný prostředek umožňující změnu vzájemné polohy vzorku a svazku elektromagnetického vlnění, alespoň jeden optický nebo jiný mikroskop (3) sestávající se ze zdroje (5)

elektromagnetické vlnění, alespoň jedné čočky (7) a alespoň jednoho záznamového zařízení (8) pro záznam digitálních snímků, **v y z n a č u j í c í s e t í m**, že je opatřeno řídící jednotkou (4) pro nastavení polohy stolku (6), pro ovládání zdroje (5) elektromagnetického vlnění, pro ovládání funkce kamery (8) a pro ukládání pořízených mikroskopických snímků, která zahrnuje alespoň jedno datové úložiště (9), ve kterém je uložen alespoň jeden softwarový modul pro řízení funkce zařízení a zpracování pořízených snímků.

6. Zařízení podle nároku 5, **v y z n a č u j í c í s e t í m**, že alespoň jedna objektivová čočka (7) je uspořádána v reflektorovém objektivu, nebo je uspořádána v reflektorové optice.

7. Zařízení podle nároku 6, **v y z n a č u j í c í s e t í m**, že softwarový modul pro řízení funkce zařízení a zpracování pořízených snímků obsahuje alespoň jeden softwarový program pro zpracování pořízených snímků, pro synchronizaci polohování stolku (6) s nastavováním a rozsvěcováním zdroje (5) elektromagnetického vlnění a spouštěním kamery (8).

8. Softwarový program pro pořizování a zpracování snímků mikroskopovaného vzorku (2), **v y z n a č u j í c í s e t í m**, že zahrnuje algoritmy pro
   - nastavování a krokovou změnu polohy polohovatelného stolku (6),
   - nastavování intenzity elektromagnetické vlnění emitovaného zdrojem (5) elektromagnetického vlnění,
   - pro řízené rozsvěcování a zhasínání zdroje (5) elektromagnetické vlnění,
   - pro synchronizaci polohování stolku (6), blikání elektromagnetického vlnění, spouštění kamery (8) a pořízení snímků,
   - pro zpracování série snímků mikroskopovaného vzorku (2),
   - pro vytvoření 3D modelu (10) struktury objektu zájmu.

Anotace

Způsob pořizování mikroskopických snímků a jejich následného zpracování a zařízení k provádění tohoto způsobu

Problém k řešení: V současné době je rozlišení mikroskopování prováděného za pomoci elektromagnetického vlnění bez nebo za použití barvicích agentů omezeno fyzikálními vlastnostmi šíření elektromagnetického vlnění, například Abbého difrakčním limitem.

Řešení: Je vytvořen způsob pořizování a vyhodnocení snímků v průběhu mikroskopování, při kterém se pořídí série odlišných snímků mikroskopovaného vzorku (2). Všechny nebo vybrané snímky se v digitální podobě pod sebe vyrovnají a naskládají do datové 3D matice, která je analyzována pixel po pixelu, úroveň po úrovni. Na základě existence pixelů s neměnnou intenzitou v rámci přesnosti měření a na základě porovnání s intenzitou histogramu pozadí jednotlivých snímků, je nalezen objekt zájmu, určena jeho přesná poloha na snímcích a je vytvořen trojrozměrný model (10) struktury v něm se nacházejících podobjektů.

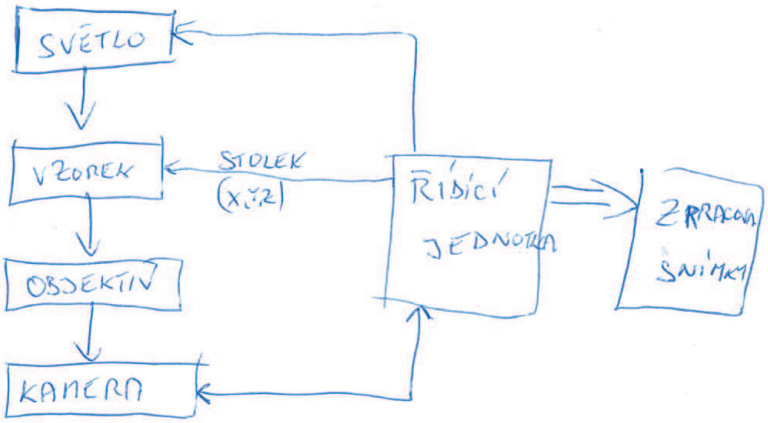

OBR. 1

OBR. 2

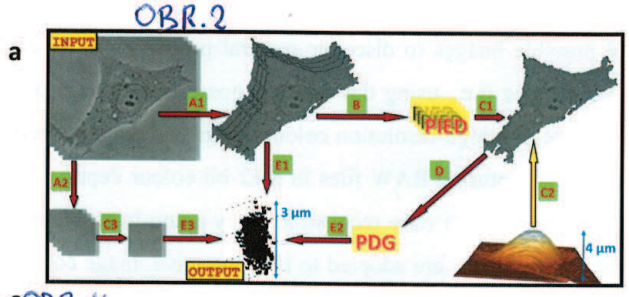

OBR. 3

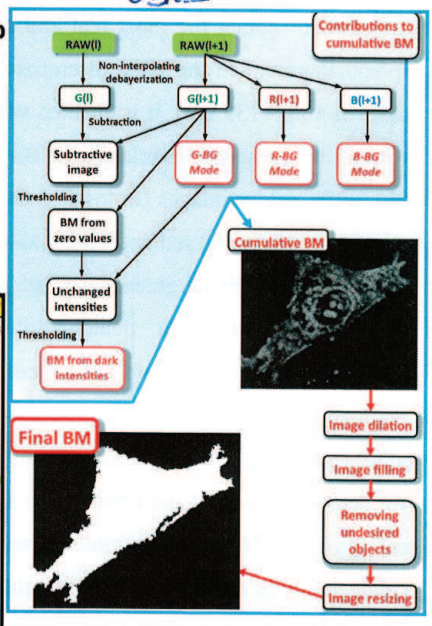

OBR. 4

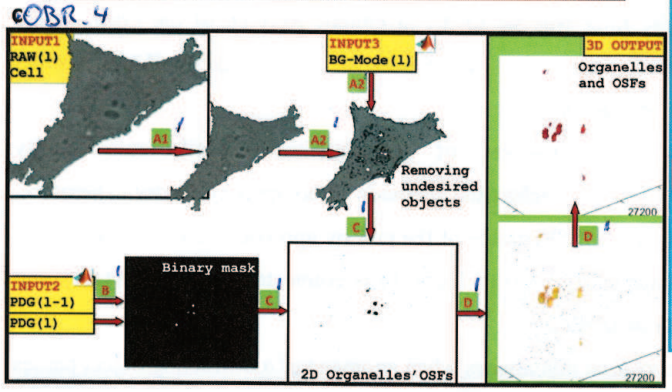

C Matlab Scripts

List of Listings C.1: Airy Disc Simulation

```
% function for Airy Disc simulation in the focus plain
function AiryDiscSim

x=-20:0.1:20;


I0=1;
airyCircle=zeros(401,401);
I=zeros(length(x),1);
c=201;

for i=1:length(x)
    I(i)=I0*(2*besselj(1,x(i))/x(i))^2;
end
% plot Airy Disc - intensity profile
figure;
plot(x,I,'b-');
hold on;
plot(x(1):0.01:x(end),0,'k-');

for r=0:200
   for phi=0:0.0001:2*pi()
       airyCircle(round(c+r*cos(phi)),round(c+r*sin(phi)))=I(r+200);
   end
end
```

```
% plot Airy Disc - top view
figure;
imagesc(airyCircle);
axis equal;
axis tight;

% plot Airy Disc - 3D view
figure;surf(airyCircle)
view(45,45);
axis tight
colormap('jet');
```

List of Listings C.2: ENZ Simulation

```
function ENZ_Dizertace
% Enz Simulation - Thesis

% Settings - Parameters of ENZ Simulation
aberration='No';      % serves only for name
m=0;                  % m, n can be changed for simulation
n=0;                  % of different aberrations
Z=0.3;                % Z - "power" of aberration

r_list=0:0.005:1;
f_list=-3:0.03:3;

na=0.50;          % the numerical aperture
diam=0.2;         % diameter in microns
lambda=0.200;     % wavelength in microns
eps=0.00001;      % a small offset epsilon, to avoid deviding by zero

radius=diam/2;
ap=2*pi*(na/lambda)*radius;
d=1/8*ap^2+1/384*ap^4+1/10240*ap^6; % optimal d.

scale_z=lambda/(2*pi)*1/(1-sqrt(1-na^2)); % scaling factor for defocus


[r,f]=meshgrid((r_list+eps)*2*pi*na/lambda,f_list/scale_z);

% by using a complex defocus parameter, the finite diameter
% is taken into account.
f=f+1i*d;

[x,y]=meshgrid([-r_list(end:-1:2) r_list],[-r_list(end:-1:2) r_list]);
phi=angle(x+1i*y);

u_0=Vnm(r,f,0,0);
```

```
u_aber=Vnm(r,f,n,m);

image3D=zeros([size(phi),length(f_list)]);

% calculations

for foc=1:length(f_list)
    u_0xy=interp1(r_list,u_0(foc,:),sqrt(x(:).^2+y(:).^2));
    u_0xy=reshape(u_0xy,size(x));
    u_aberxy=interp1(r_list,u_aber(foc,:),sqrt(x(:).^2+y(:).^2));
    u_aberxy=1i^(m+1)*2*pi*Z*reshape(u_aberxy,size(x)).*cos(m*phi);
    field=u_0xy+u_aberxy;
    intensity=real(field.*conj(field));
    intensity(isnan(intensity))=0;
    image3D(:,:,foc)=intensity;
end

% Plotting graphs
% 3D image
image3D=image3D/max(max(max(image3D)));
figure('units','normalized','outerposition',[0 0 1 1]);
h = vol3d('cdata',image3D,'texture','2D');
view(3);
vol3d(h);
alphamap('vup');
alphamap(.075 .* alphamap);
grid on;
view(-10,5);
title(['3D model of ',aberration,' aberration'],'FontSize',16, ...
    'FontWeight','bold');
xlabel('X Radius [\mum]','FontSize',14);
ylabel('Y Radius [\mum]','FontSize',14);
zlabel('Focus [\mum]','FontSize',14)

XTicks=get(gca,'XTick');
```

```
YTicks=get(gca,'YTick');
ZTicks=get(gca,'ZTick');

set(gca,'FontSize',12,'FontWeight','bold');
set(gca,'XTickLabel',(XTicks/max(XTicks)*2*max(r_list)-max(r_list)));
set(gca,'YTickLabel',(YTicks/max(YTicks)*2*max(r_list)-max(r_list)));
set(gca,'ZTickLabel',(ZTicks/max(ZTicks)*2*max(f_list)-max(f_list)));

hgexport(gcf, [aberration,'_3D' '.png'], hgexport('factorystyle'), ...
    'Format', 'png');
hgsave(gcf, [aberration,'_3D' '.fig'],'-v7.3');
close(gcf);

% 2D section in focus
figure('units','normalized','outerposition',[0 0 1 1]);
imagesc(image3D(:,:,101));
title('View in Focus','FontSize',16,'FontWeight','bold');
xlabel('X Radius [\mum]','FontSize',14);
ylabel('Y Radius [\mum]','FontSize',14);

axis equal;
axis tight;

XTicks=get(gca,'XTick');
YTicks=get(gca,'YTick');
set(gca,'FontSize',12,'FontWeight','bold','LineWidth',2);
set(gca,'XTickLabel',(XTicks/max(XTicks)*2*max(r_list)-max(r_list)));
set(gca,'YTickLabel',(YTicks/max(YTicks)*2*max(r_list)-max(r_list)));
grid on;

hgexport(gcf, [aberration,'_Focus' '.png'], hgexport('factorystyle'), ...
    'Format', 'png');
hgsave(gcf, [aberration,'_Focus' '.fig'],'-v7.3');
close(gcf);
```

```
% 2D section in through centre of particle YZ plane
figure('units','normalized','outerposition',[0 0 1 1]);
imagesc(squeeze(image3D(201,:,:))');
title('YZ View in centre','FontSize',16,'FontWeight','bold');
xlabel('Y Radius [\mum]','FontSize',14);
ylabel('Focus [\mum]','FontSize',14)

axis equal;
axis tight;

XTicks=get(gca,'XTick');
YTicks=get(gca,'YTick');

set(gca,'FontSize',12,'FontWeight','bold','LineWidth',2);
set(gca,'XTickLabel',(XTicks/max(XTicks)*2*max(r_list)-max(r_list)));
set(gca,'YTickLabel',(YTicks/max(YTicks)*2*max(f_list)-max(f_list)));
grid on;

hgexport(gcf, [aberration,'_YZ' '.png'], hgexport('factorystyle'), ...
    'Format', 'png');
hgsave(gcf, [aberration,'_YZ' '.fig'],'-v7.3');
close(gcf);

% 2D section in through centre of particle XZ plane
figure('units','normalized','outerposition',[0 0 1 1]);
imagesc(squeeze(image3D(:,201,:))');
title('XZ View in centre','FontSize',16,'FontWeight','bold');
xlabel('X Radius [\mum]','FontSize',14);
ylabel('Focus [\mum]','FontSize',14)

axis equal;
axis tight;

XTicks=get(gca,'XTick');
YTicks=get(gca,'YTick');
```

```
set(gca,'FontSize',12,'FontWeight','bold','LineWidth',2);
set(gca,'XTickLabel',(XTicks/max(XTicks)*2*max(r_list)-max(r_list)));
set(gca,'YTickLabel',(YTicks/max(YTicks)*2*max(f_list)-max(f_list)));
grid on;

hgexport(gcf, [aberration,'_XZ' '.png'], hgexport('factorystyle'), ...
    'Format', 'png');
hgsave(gcf, [aberration,'_XZ' '.fig'],'-v7.3');
close(gcf);
```

List of Listings C.3: ENZ Simulation Wavelength Dependency

```
function ENZ_Dizertace_Light_Dep
% Enz Simulation - Thesis
% Light wavelength dependency

% Settings - Parameters of ENZ Simulation
aberration='No';      % serves only for name
m=0;                  % m, n can be changed for simulation
n=0;                  % of different aberrations
Z=0;                  % Z - "power" of aberration

r_list=0:0.005:1;
f_list=-3:0.03:3;

na=0.50;          % the numerical aperture
diam=0.2;         % diameter in microns
lambda=0.800;     % wavelength in microns
eps=0.00001;      % a small offset epsilon, to avoid deviding by zero

radius=diam/2;
ap=2*pi*(na/lambda)*radius;
d=1/8*ap^2+1/384*ap^4+1/10240*ap^6; % optimal d.

scale_z=lambda/(2*pi)*1/(1-sqrt(1-na^2)); % scaling factor for defocus

[r,f]=meshgrid((r_list+eps)*2*pi*na/lambda,f_list/scale_z);

% by using a complex defocus parameter,
% the finite diameter is taken into account.
f=f+1i*d;

[x,y]=meshgrid([-r_list(end:-1:2) r_list],[-r_list(end:-1:2) r_list]);
phi=angle(x+1i*y);

u_0=Vnm(r,f,0,0);
```

```
u_aber=Vnm(r,f,n,m);

image3D=zeros([size(phi),length(f_list)]);

% calculations

for foc=1:length(f_list)
    u_0xy=interp1(r_list,u_0(foc,:),sqrt(x(:).^2+y(:).^2));
    u_0xy=reshape(u_0xy,size(x));
    u_aberxy=interp1(r_list,u_aber(foc,:),sqrt(x(:).^2+y(:).^2));
    u_aberxy=1i^(m+1)*2*pi*Z*reshape(u_aberxy,size(x)).*cos(m*phi);
    field=u_0xy+u_aberxy;
    intensity=real(field.*conj(field));
    intensity(isnan(intensity))=0;
    image3D(:,:,foc)=intensity;
end

% Plotting graphs
% 3D image
image3D=image3D/max(max(max(image3D)));
figure('units','normalized','outerposition',[0 0 1 1]);
h = vol3d('cdata',image3D,'texture','2D');
view(3);
vol3d(h);
alphamap('vup');
alphamap(.075 .* alphamap);
grid on;
view(-10,5);
title(['3D model of ',aberration,' aberration'],'FontSize',16,...
    'FontWeight','bold');
xlabel('X Radius [\mum]','FontSize',14);
ylabel('Y Radius [\mum]','FontSize',14);
zlabel('Focus [\mum]','FontSize',14)

XTicks=get(gca,'XTick');
```

```
YTicks=get(gca,'YTick');
ZTicks=get(gca,'ZTick');

set(gca,'FontSize',12,'FontWeight','bold');
set(gca,'XTickLabel',(XTicks/max(XTicks)*2*max(r_list)-max(r_list)));
set(gca,'YTickLabel',(YTicks/max(YTicks)*2*max(r_list)-max(r_list)));
set(gca,'ZTickLabel',(ZTicks/max(ZTicks)*2*max(f_list)-max(f_list)));

hgexport(gcf, [aberration,'_3D_',num2str(lambda), '.png'],...
    hgexport('factorystyle'), 'Format', 'png');
hgsave(gcf, [aberration,'_3D_',num2str(lambda), '.fig'],'-v7.3');
close(gcf);

% 2D section in focus
figure('units','normalized','outerposition',[0 0 1 1]);
imagesc(image3D(:,:,101));
title('View in Focus','FontSize',16,'FontWeight','bold');
xlabel('X Radius [\mum]','FontSize',14);
ylabel('Y Radius [\mum]','FontSize',14);

axis equal;
axis tight;

XTicks=get(gca,'XTick');
YTicks=get(gca,'YTick');
set(gca,'FontSize',12,'FontWeight','bold','LineWidth',2);
set(gca,'XTickLabel',(XTicks/max(XTicks)*2*max(r_list)-max(r_list)));
set(gca,'YTickLabel',(YTicks/max(YTicks)*2*max(r_list)-max(r_list)));
grid on;

hgexport(gcf, [aberration,'_Focus_',num2str(lambda), '.png'],...
    hgexport('factorystyle'), 'Format', 'png');
hgsave(gcf, [aberration,'_Focus_' ,num2str(lambda),'.fig'],'-v7.3');
close(gcf);
```

```
% 2D section in through centre of particle YZ plane
figure('units','normalized','outerposition',[0 0 1 1]);
imagesc(squeeze(image3D(201,:,:))');
title('YZ View in centre','FontSize',16,'FontWeight','bold');
xlabel('Y Radius [\mum]','FontSize',14);
ylabel('Focus [\mum]','FontSize',14)

axis equal;
axis tight;

XTicks=get(gca,'XTick');
YTicks=get(gca,'YTick');

set(gca,'FontSize',12,'FontWeight','bold','LineWidth',2);
set(gca,'XTickLabel',(XTicks/max(XTicks)*2*max(r_list)-max(r_list)));
set(gca,'YTickLabel',(YTicks/max(YTicks)*2*max(f_list)-max(f_list)));
grid on;

hgexport(gcf, [aberration,'_YZ_',num2str(lambda),'.png'],...
    hgexport('factorystyle'), 'Format', 'png');
hgsave(gcf, [aberration,'_YZ_',num2str(lambda), '.fig'],'-v7.3');
close(gcf);

% 2D section in through centre of particle XZ plane
figure('units','normalized','outerposition',[0 0 1 1]);
imagesc(squeeze(image3D(:,201,:))');
title('XZ View in centre','FontSize',16,'FontWeight','bold');
xlabel('X Radius [\mum]','FontSize',14);
ylabel('Focus [\mum]','FontSize',14)

axis equal;
axis tight;

XTicks=get(gca,'XTick');
YTicks=get(gca,'YTick');
```

```
set(gca,'FontSize',12,'FontWeight','bold','LineWidth',2);
set(gca,'XTickLabel',(XTicks/max(XTicks)*2*max(r_list)-max(r_list)));
set(gca,'YTickLabel',(YTicks/max(YTicks)*2*max(f_list)-max(f_list)));
grid on;

hgexport(gcf, [aberration,'_XZ_',num2str(lambda), '.png'],...
    hgexport('factorystyle'), 'Format', 'png');
hgsave(gcf, [aberration,'_XZ_',num2str(lambda),'.fig'],'-v7.3');
close(gcf);
```

List of Listings C.4: ENZ Simulation Size Dependency

```
function ENZ_Dizertace_Size_Dep
% Enz Simulation - Thesis
% Size Dependency

% Settings - Parameters of ENZ Simulation
aberration='No';      % serves only for name
m=0;                  % m, n can be changed for simulation
n=0;                  % of different aberrations
Z=0;                  % Z - "power" of aberration

r_list=0:0.005:1;
f_list=-3:0.03:3;

na=0.50;          % the numerical aperture
diam=0.1;         % diameter in microns
lambda=0.200;     % wavelength in microns
eps=0.00001;      % a small offset epsilon, to avoid deviding by zero

radius=diam/2;
ap=2*pi*(na/lambda)*radius;
d=1/8*ap^2+1/384*ap^4+1/10240*ap^6; % optimal d.

scale_z=lambda/(2*pi)*1/(1-sqrt(1-na^2)); % scaling factor for defocus

[r,f]=meshgrid((r_list+eps)*2*pi*na/lambda,f_list/scale_z);

% by using a complex defocus parameter,
% the finite diameter is taken into account.
f=f+1i*d;

[x,y]=meshgrid([-r_list(end:-1:2) r_list],[-r_list(end:-1:2) r_list]);
phi=angle(x+1i*y);

u_0=Vnm(r,f,0,0);
```

```
u_aber=Vnm(r,f,n,m);

image3D=zeros([size(phi),length(f_list)]);

% calculations

for foc=1:length(f_list)
    u_0xy=interp1(r_list,u_0(foc,:),sqrt(x(:).^2+y(:).^2));
    u_0xy=reshape(u_0xy,size(x));
    u_aberxy=interp1(r_list,u_aber(foc,:),sqrt(x(:).^2+y(:).^2));
    u_aberxy=1i^(m+1)*2*pi*Z*reshape(u_aberxy,size(x)).*cos(m*phi);
    field=u_0xy+u_aberxy;
    intensity=real(field.*conj(field));
    intensity(isnan(intensity))=0;
    image3D(:,:,foc)=intensity;
end

% Plotting graphs
% 3D image
image3D=image3D/max(max(max(image3D)));
figure('units','normalized','outerposition',[0 0 1 1]);
h = vol3d('cdata',image3D,'texture','2D');
view(3);
vol3d(h);
alphamap('vup');
alphamap(.075 .* alphamap);
grid on;
view(-10,5);
title(['3D model of ',aberration,' aberration'],'FontSize',16,...
    'FontWeight','bold');
xlabel('X Radius [\mum]','FontSize',14);
ylabel('Y Radius [\mum]','FontSize',14);
zlabel('Focus [\mum]','FontSize',14)

XTicks=get(gca,'XTick');
```

```
YTicks=get(gca,'YTick');
ZTicks=get(gca,'ZTick');

set(gca,'FontSize',12,'FontWeight','bold');
set(gca,'XTickLabel',(XTicks/max(XTicks)*2*max(r_list)-max(r_list)));
set(gca,'YTickLabel',(YTicks/max(YTicks)*2*max(r_list)-max(r_list)));
set(gca,'ZTickLabel',(ZTicks/max(ZTicks)*2*max(f_list)-max(f_list)));

hgexport(gcf, [aberration,'_3D_rad_',num2str(diam), '.png'],...
    hgexport('factorystyle'), 'Format', 'png');
hgsave(gcf, [aberration,'_3D_rad_',num2str(diam), '.fig'],'-v7.3');
close(gcf);

% 2D section in focus
figure('units','normalized','outerposition',[0 0 1 1]);
imagesc(image3D(:,:,101));
title('View in Focus','FontSize',16,'FontWeight','bold');
xlabel('X Radius [\mum]','FontSize',14);
ylabel('Y Radius [\mum]','FontSize',14);

axis equal;
axis tight;

XTicks=get(gca,'XTick');
YTicks=get(gca,'YTick');
set(gca,'FontSize',12,'FontWeight','bold','LineWidth',2);
set(gca,'XTickLabel',(XTicks/max(XTicks)*2*max(r_list)-max(r_list)));
set(gca,'YTickLabel',(YTicks/max(YTicks)*2*max(r_list)-max(r_list)));
grid on;

hgexport(gcf, [aberration,'_Focus_rad_',num2str(diam), '.png'],...
    hgexport('factorystyle'), 'Format', 'png');
hgsave(gcf, [aberration,'_Focus_rad_',num2str(diam),'.fig'],'-v7.3');
close(gcf);
```

```
% 2D section in through centre of particle YZ plane
figure('units','normalized','outerposition',[0 0 1 1]);
imagesc(squeeze(image3D(201,:,:))');
title('YZ View in centre','FontSize',16,'FontWeight','bold');
xlabel('Y Radius [\mum]','FontSize',14);
ylabel('Focus [\mum]','FontSize',14)

axis equal;
axis tight;

XTicks=get(gca,'XTick');
YTicks=get(gca,'YTick');

set(gca,'FontSize',12,'FontWeight','bold','LineWidth',2);
set(gca,'XTickLabel',(XTicks/max(XTicks)*2*max(r_list)-max(r_list)));
set(gca,'YTickLabel',(YTicks/max(YTicks)*2*max(f_list)-max(f_list)));
grid on;

hgexport(gcf, [aberration,'_YZ_rad_',num2str(diam),'.png'],...
    hgexport('factorystyle'), 'Format', 'png');
hgsave(gcf, [aberration,'_YZ_rad_',num2str(diam), '.fig'],'-v7.3');
close(gcf);

% 2D section in through centre of particle XZ plane
figure('units','normalized','outerposition',[0 0 1 1]);
imagesc(squeeze(image3D(:,201,:))');
title('XZ View in centre','FontSize',16,'FontWeight','bold');
xlabel('X Radius [\mum]','FontSize',14);
ylabel('Focus [\mum]','FontSize',14)

axis equal;
axis tight;

XTicks=get(gca,'XTick');
YTicks=get(gca,'YTick');
```

```
set(gca,'FontSize',12,'FontWeight','bold','LineWidth',2);
set(gca,'XTickLabel',(XTicks/max(XTicks)*2*max(r_list)-max(r_list)));
set(gca,'YTickLabel',(YTicks/max(YTicks)*2*max(f_list)-max(f_list)));
grid on;

hgexport(gcf, [aberration,'_XZ_rad_',num2str(diam), '.png'],...
    hgexport('factorystyle'), 'Format', 'png');
hgsave(gcf, [aberration,'_XZ_rad_',num2str(diam),'.fig'],'-v7.3');
close(gcf);
```

List of Listings C.5: 3D reconstraction of fluorescent particles

```
function fluorPart

input=['E:\Work\Dizertace\Microbeads_Vienna_14102014\',...
    'Microbeads_14102014\'];
diam=0.22;

files=dir([input,num2str(diam),'*.tif']);

img=(imread([input,files(1).name]));
[x,y]=size(img);
image3D=zeros(x,y,length(files)-1);

for i=1:length(files)-1
    img=(imread([input,files(i).name]));
    image3D(:,:,i)=img;
end

figure('units','normalized','outerposition',[0 0 1 1]);
h = vol3d('cdata',image3D(100:300,100:300,:),'texture','2D');
% h = vol3d('cdata',image3D,'texture','2D');
view(3);
vol3d(h);
alphamap('vup');
alphamap(.075 .* alphamap);
grid on;
view(30,10);
title(['3D image of ',num2str(diam),'\mum latex praticles'],...
    'FontSize',16,'FontWeight','bold');
xlabel('X Position [\mum]','FontSize',14);
ylabel('Y Position [\mum]','FontSize',14);
zlabel('Z Position [\mum]','FontSize',14)

XTicks=get(gca,'XTick');
YTicks=get(gca,'YTick');
```

```
ZTicks=get(gca,'ZTick');

set(gca,'FontSize',12,'FontWeight','bold');
set(gca,'XTickLabel',XTicks*0.0963);
set(gca,'YTickLabel',YTicks*0.0963);
set(gca,'ZTickLabel',ZTicks*0.125);

hgexport(gcf, [aberration,'_3D' '.png'],...
    hgexport('factorystyle'), 'Format', 'png');
hgsave(gcf, [aberration,'_3D' '.fig'],'-v7.3');
close(gcf);
```

List of Listings C.6: 3D reconstruction of real PSF

```
function make3D
% 3D reconstruction of nanopraticles based on
% entropy recalcultaion of BF images
intensity='1000mA';
input=['E:\Data\Nanoparticles - 0-22um\',...
    'PreparedData\1000mA\Cut\2\Entropy RGB-RGB-0,5-Whole image\'];
pxsize=39.54;

channel=2;

limits=[98,317,100,324];
coor=[98,317,100,324,22845,0.4,22886,0.6];

step=100;

files=dir([input,'*.png']);

img3D=zeros(limits(4)-limits(3)+1,limits(2)-limits(1)+1,length(files));

for i=1:length(files)
    img=imread([input,files(i).name]);
    temp=img(coor(3):coor(4),coor(1):coor(2),channel);
    img3D(:,:,i)=temp;
end

figure('units','normalized','outerposition',[0 0 1 1]);
h = vol3d('cdata',img3D,'texture','3D');
view(3);
% Update view since 'texture' = '2D'
vol3d(h);
alphamap('vup');
alphamap(.075 .* alphamap);
axis tight;
daspect([pxsize pxsize step]);
```

```
grid on;
zoom(0.5);
title(['0.22 \mum particle - Intensity ',intensity ,],...
    'FontSize',16,'FontWeight','bold');
xlabel('X position [\mum]','FontSize',14);
ylabel('Y position [\mum]','FontSize',14);
zlabel('Z position [\mum]','FontSize',14)

XTicks=get(gca,'XTick');
YTicks=get(gca,'YTick');
ZTicks=get(gca,'ZTick');

set(gca,'FontSize',12,'FontWeight','bold');
set(gca,'XTickLabel',XTicks*pxsize*0.001);
set(gca,'YTickLabel',YTicks*pxsize*0.001);
set(gca,'ZTickLabel',ZTicks*step*0.001);

hgexport(gcf, [aberration,'_3D' '.png'],...
    hgexport('factorystyle'), 'Format', 'png');
hgsave(gcf, [aberration,'_3D' '.fig'],'-v7.3');
close(gcf);
```

List of Listings C.7: 3D reconstruction of PSF Core

```
% function make3DCore
% 3D reconstruction of PSF Core
intensity='2000mA';
level='Lev_60';

inputCore=['E:\Data\Nanoparticles - 0-22um\PreparedData\',...
    '2000mA\Cut\2\RoiSelection\All_Objects\',...
    'I-1_x_110-301_y_127-302\',level,'\'];

pxsize=39.54;

channel=2;

coor=[110,301,127,302,22845,0.2,22886,-0.02];
limits=coor(1:4);

step=100;

filesCore=dir([inputCore,'*.png']);

core3D=zeros(limits(4)-limits(3)+1,limits(2)-limits(1)+1,...
    length(filesCore));

for i=1:length(filesCore)
    imgCore=imread([inputCore,filesCore(i).name]);
    tempCore=imgCore(:,:,channel);
    core3D(:,:,i)=tempCore;
end

img3D=core3D;

figure('units','normalized','outerposition',[0 0 1 1]);
h = vol3d('cdata',img3D,'texture','3D');
view(3);
```

```
% Update view since 'texture' = '2D'
vol3d(h);
axis tight;
grid on;
zoom(0.5);
title(['0.22 \mum particle - Intensity ',intensity,...
    ' - Channel - ',num2str(channel)],...
    'FontSize',16,'FontWeight','bold');
xlabel('X position [\mum]','FontSize',14);
ylabel('Y position [\mum]','FontSize',14);
zlabel('Z position [\mum]','FontSize',14)

XTicks=get(gca,'XTick');
YTicks=get(gca,'YTick');
ZTicks=get(gca,'ZTick');

colormap(jet)
set(gca,'FontSize',12,'FontWeight','bold');
set(gca,'XTickLabel',XTicks*pxsize*0.001);
set(gca,'YTickLabel',YTicks*pxsize*0.001);
set(gca,'ZTickLabel',ZTicks*step*0.001);


% hgexport(gcf, [intensity,'_3D_Core_Level-',level,'-Channel-',...
%     num2str(channel),'.png'],...
%     hgexport('factorystyle'), 'Format', 'png');
% hgsave(gcf, [intensity,'_3D_Core_Level-',level,'-Channel-',...
%     num2str(channel),'.fig'],'-v7.3');
% close(gcf);
```

List of Listings C.8: 3D reconstruction of PDG Model

```
% function make3DPDGModel
% 3D reconstruction of PDG Model
intensity='1000mA';
input=['E:\Data\Nanoparticles - 0-22um\PreparedData\',...
    intensity,'\Cut\2\RoiSelection\All_Objects\'];
pxsize=39.54;

channel=2;

coor=[111,312,124,283,22845,0.72,22886,0.5];
limits=coor(1:4);

step=100;

files=dir([input,'*.png']);

img3D=zeros(limits(4)-limits(3)+1,limits(2)-limits(1)+1,length(files));

for i=1:length(files)
    img=imread([input,files(i).name]);
    temp=img(coor(3):coor(4),coor(1):coor(2),channel);
    img3D(:,:,i)=temp;
end

figure('units','normalized','outerposition',[0 0 1 1]);
h = vol3d('cdata',img3D(:,:,1:end-7),'texture','3D');
view(3);
% Update view since 'texture' = '2D'
vol3d(h);
axis tight;
daspect([pxsize pxsize step]);
grid on;
zoom(0.5);
title(['0.22 \mum particle - Intensity ',intensity,],...
```

```
    'FontSize',16,'FontWeight','bold');
xlabel('X position [\mum]','FontSize',14);
ylabel('Y position [\mum]','FontSize',14);
zlabel('Z position [\mum]','FontSize',14)

XTicks=get(gca,'XTick');
YTicks=get(gca,'YTick');
ZTicks=get(gca,'ZTick');
set(gca,'FontSize',12,'FontWeight','bold');
set(gca,'XTickLabel',XTicks*pxsize*0.001);
set(gca,'YTickLabel',YTicks*pxsize*0.001);
set(gca,'ZTickLabel',ZTicks*step*0.001*2);

% hgexport(gcf, [intensity,'_3D_PDG' '.png'],...
%     hgexport('factorystyle'), 'Format', 'png');
% hgsave(gcf, [intensity,'_3D_PDG' '.fig'],'-v7.3');
```

List of Listings C.9: 3D reconstruction of PSF Core shells with different intensities

```
function particleShells3D
% 3D reconstruction of PSF Shells of different intensity levels

% coordinates of particle in the image
coor=[111,312,124,283,22845,0.72,22886,0.5];
limits=coor(1:4);

img3D=zeros(limits(4)-limits(3)+1,limits(2)-limits(1)+1,399);
h=waitbar(0,'Levels');

% preprocessing of data
for level=60:20:140
    waitbar(level/140);
    intensity='3500mA';
    input=['E:\Data\Nanoparticles - 0-22um\PreparedData\3500mA\',...
        'Cut\2\RoiSelection\All_Objects\I-1_x_111-312_y_124-283\',...
        'Lev_',num2str(level),'\'];
    pxsize=39.54; % definition of the size of the pixel

    channel=2; % using green channel

    step=100;

    files=dir([input,'*.png']);

    for i=1:length(files)
        img=imread([input,files(i).name]);
        [x,y,~]=size(img);
        img3D(coor(3)-limits(3)+1:coor(3)-limits(3)+x,...
            coor(1)-limits(1)+1:coor(1)-limits(1)+y,i)=...
            double(img3D(coor(3)-limits(3)+1:coor(3)-limits(3)+x,...
            coor(1)-limits(1)+1:coor(1)-limits(1)+y,i))...
            +double(img(:,:,channel)*level/10);
```

```
    end
end
close(h)

% 3D image
figure('units','normalized','outerposition',[0 0 1 1]);
h = vol3d('cdata',img3D(50:end-50,50:end-50,:),'texture','3D');
view(3);
% Update view since 'texture' = '2D'
vol3d(h);
axis tight;
% Changing ration of the axis according to real sizes
daspect([pxsize pxsize step]);
grid on;
zoom(0.5);
title(['0.22 \mum particle - Intensity ',intensity,...
    ' - Shells 60 - 140 '],'FontSize',16,'FontWeight','bold');
xlabel('X position [\mum]','FontSize',14);
ylabel('Y position [\mum]','FontSize',14);
zlabel('Z position [\mum]','FontSize',14)

XTicks=get(gca,'XTick');
YTicks=get(gca,'YTick');
ZTicks=get(gca,'ZTick');

set(gca,'FontSize',12,'FontWeight','bold');
set(gca,'XTickLabel',XTicks*pxsize*0.001);
set(gca,'YTickLabel',YTicks*pxsize*0.001);
set(gca,'ZTickLabel',ZTicks*step*0.001);
alphamap('vup');
alphamap(.075 .* alphamap);
view(50,20)
colormap(hsv);
hgexport(gcf, [intensity,'_shells_60-140' '.png'],...
    hgexport('factorystyle'), 'Format', 'png');
```

```
hgsave(gcf, [intensity,'_shells_60-140' '.fig'],'-v7.3');
```

D Other results

Image D.1 shows results of first preliminary experiments.

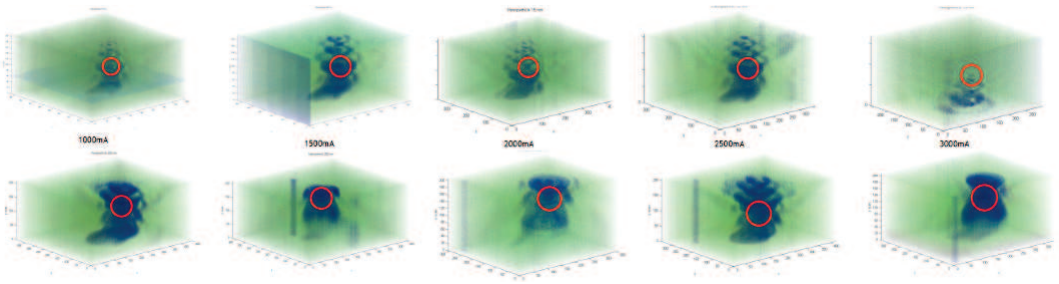

Figure D.1: Real PSF - Different Light Intensities. Upper row - $15nm$ gold particle, bottom row - $200nm$ latex particle. From left to right - $1000mA$, $1500mA$, $2000mA$, $2500mA$, $3000mA$

According to our measured data I tried to simulate the PSF of our microscope however I was not able to gain complete matching of simulation and our experiments. What is shown on Fig. D.2 is comparison of simulated and real PSF. Parameters of the simulated PSF was estimated based on the visual comparison with real PSF.

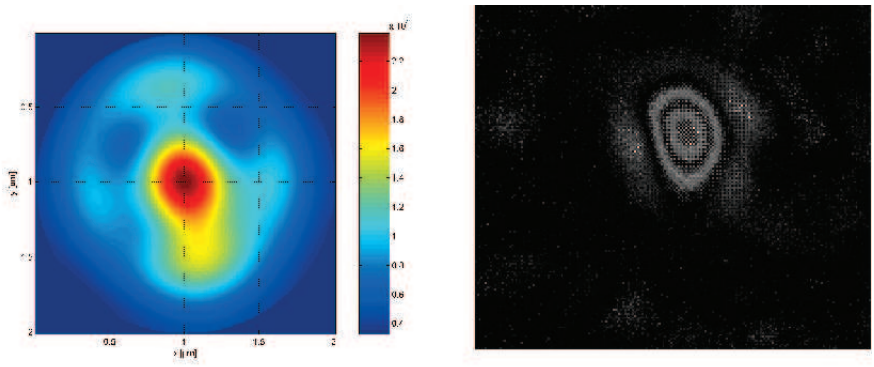

Figure D.2: Comparison of simulated and real PSF - Left part - Simulated PSF, Right part - Real PSF

E Article - The cell monolayer trajectory from the system state point of view

Dalibor Stys, Jan Vanek, Tomas Nahlik, Jan Urban and Petr Cisar
Received 28th February 2011, Accepted 16th July 2011
DOI: 10.1039/c1mb05083d

Abstract:

Time-lapse microscopic movies are being increasingly utilized for understanding the derivation of cell states and predicting cell future. Often, fluorescence and other types of labeling are not available or desirable, and cell state-definitions based on observable structures must be used. We present the methodology for cell behavior recognition and prediction based on the short term cell recurrent behavior analysis. This approach has theoretical justification in non-linear dynamics theory. The methodology is based on the general stochastic systems theory which allows us to define the cell states, trajectory and the system itself. We introduce the usage of a novel image content descriptor based on information contribution (gain) by each image point for the cell state characterization as the first step. The linkage between the method and the general system theory is presented as a general frame for cell behavior interpretation. We also discuss extended cell description, system theory and methodology for future development. This methodology may be used for many practical purposes, ranging from advanced, medically relevant, precise cell culture diagnostics to very utilitarian cell recognition in a noisy or uneven image background. In addition, the results are theoretically

justified.

F Article - The State Trajectory of Cell Using Rényi Entropy Coefficients

Tomas Nahlik, Jan Urban, Dalibor Stys, Petr Cisar, Aliaksandr Pautsina, Jan Vanek

Abstract:

The construction of state trajectory of the cell is not a simple task. It must be decided what are the state variables. Since we work with coloured images, it sounds logical to start with the trajectory in RGB colour space. Each axis is then processed via several Rényi entropies. The value of Rényi coefficient spread or collapsed the trajectory along the axis of the state space. Each combination of Rényi coefficients gives us one subtraction of the whole trajectory. The major issue is how to choose the proper combination. However, all subtractions are correct. The single cell trajectory should be divided into several clusters, once the trajectory is constructed. Each cluster of the trajectory represents an event or subset of the states of the cell. Size and position of clusters depends on the trajectory and on number of clusters. We proposed eight clusters now as a first estimation, satisfied by the results: Clusters are well separated; images in transitions between clusters show some changes. Changes are also observable in images at the borders of the clusters. If we compare content of the clusters in different trajectories some images stay in the same cluster but some images may change the cluster. This is caused by the method of acquisition of the trajectory. The different coefficient in the Rényi equation highlights different part of the image so the

trajectory can be little bit different as well as size, position and content of clusters.

G Article - Entropy based approximation to cell monolayer development

T. Nahlik, J.Urban, P. Cisar, J. Vanek and D. Stys

Abstract:

Our analysis is based on the assumption that the metabolic and signal pathways substantiate non-linear dynamic processes which are responsible for asymptotic stability of biological systems. Observed events, not pathways themselves, are the elementary asymptotically stable objects to be studied. This assumption is theoretically supported by observed structures in a relatively simple pseudo-chemical agent-based model. The state space is given by coefficients of Rényi information entropy. Each combination of Rényi coefficients gives us one subtraction of the whole trajectory. The single cell trajectory should be divided into several clusters, once the trajectory is constructed. Each cluster of the trajectory represents an event or subset of the states of the cell. Size and position of clusters depends on the trajectory and on number of clusters. We propose a recipe, using the rules of the generalized stochastic system theory, how to extract individual trajectories of the multifractal system the biological stochastic attractor. This set of trajectories is then utilized for thermodynamic representation of the biological chaotic attractor. Our analysis is strictly based on experiment with all its practical limits. We present implementation of analysis of development of cell monolayer observed by microphotography.

H Article - Microscope point spread function, focus and calculation of optimal microscope set-up

Tomas Nahlik and Dalibor Stys

Abstract:

If we are observing very small objects in the microscope the information appears somehow distorted. This distortion is called point spread function (PSF) and it can be measured and simulated as we show in this article. Many experiments and simulations were done in the field of confocal or deconvolution microscopy, but we want to present 3D reconstruction and measurement of PSF in the bright field (or phase contrast) microscopy. Our goal is to use this knowledge about PSF to estimate objective focus.We want to use this method for automatic focusing of the microscope.We measured the PSF on our microscope in bright field using a 100x objective. We used 15 nm gold and 200 nm latex particles as point sources. We used two different simulations; first one was Airy disc simulation; the second one was Extended NijboerZernike theory. Both approaches were used for description of PSF and finding the position of the focus.

I Manuscript - Super-resolved 3-D imaging of live cells organelles from bright-field transmission micrographs

Renata Rychtáriková[1], Tomáš Náhlík[1], Kevin Shi[2], Daria Malakhova[1], Petr Macháček[1], Petr Císař[1], Jan Urban[1] & Dalibor Štys[1]

Abstract: Current biological and medical research is aimed at obtaining a detailed spatiotemporal map of a live cell's interior to describe and predict cell's physiological state. This can be fulfilled by our algorithm for a complete 3-D modelling of cellular structures from a z-stack obtained using label-free bright-field light-transmitted microscopy. The computation is based on searching for pixels of unchanged intensities between two consecutive images of object spread function. These pixels represent strongly light-diffracting, light-absorbing or light-emitting objects. To reach that, variables derived from the Rényi entropy was used for the suppression of camera noise. The method visualizes 3-D objects of the volume that is a multiple of a camera pixel size with a z-height.

J Certificate - 3rd IFSM School

18TH INTERNATIONAL MICROSCOPY CONGRESS

Prague, 7 - 12 September 2014

MICROSCOPY FOR GLOBAL CHALLENGES

touching atoms, molecules, nanostructures and cells by multidimensional microscopy

IMC PRAGUE 2014

CERTIFICATE OF ATTENDANCE

3rd IFSM SCHOOL

6 - 7 September 2014

IFSM Young Scientist

Nahlik Thomas

Czech Republic

Prof. C. Barry Carter

IFSM President